2000

The corrosion of commercial weld overlays in low NOx environments

Melissa A. Lim
Lehigh University

Lim, Melissa A.

The Corrosion of Commercial Weld Overlays in Low Nox Environments

June 2000

The Corrosion of Commercial Weld Overlays in Low NOx Environments

by

Melissa A. Lim

A Thesis

Presented to the Graduate and Research Committee

of Lehigh University

in Candidacy for the Degree of

Master of Science

in

Materials Science and Engineering

Lehigh University

May 4, 2000

This thesis is accepted and approved in partial fulfillment of the requirements for the Mater of Science

May 5, 2000

Date

Dr. Arnold R. Marder

Dr. David B. Williams

ACKNOWLEDGEMENTS

First, I would like to thank my advisor, Dr. Arnold Marder, for giving me the opportunity to further my education and expand my horizons. I would also like to acknowledge the sponsors of the Low NOx project – PP&L, Ontario Hydro, Virginia Power, Allegheny Powder, Southern Company, and PSE&G for their financial support. Additional thanks to John DuPont for his support on this project. And to Arlan Benscoter for his never-ending help and for knowing everything there is to know about metallography.

I would like to give special thanks to the people who have helped me immensely in achieving my goals: Kevin Luer, Steve Banovic, Don Susan, Nick Barbosa, Chad Kusko, Jesse Nawrocki, Jon Regina, Mario Epler (catalyst king), and Ryan Deacon (Pax-it man). To the people outside "the group" who have helped make the days more bearable: William VanGeertruyden, Dan Lewis, Laura Roos, Eva Campo, and Jill Aaron

To my parents for all of their love and support. To my sister Valerie for all of your encouragement and advice to get me through each week. To both my brother Derek and my sister Val for all of the fun we've had together.

Finally, to Brian Newbury, who has stood by me these last two years and has given me the strength to be where I am today. I don't know what I would have done without you. I love you dearly.

Table of Contents

List of Tables

List of Figures

Abstract

Weld overlay coatings have been chosen as the method of corrosion protection in many low NOx boilers. Gaseous corrosion studies were performed on several commercial weld overlay coatings in typical low NOx atmospheres.

Four different weld claddings were studied – IN622, IN625, FM72, and 309SS. Wrought T11 and cast Fe-10wt%Al were also investigated. Five different gas compositions were used that ranged from highly oxidizing (high PO_2) to highly sulfidizing (low PO_2). The alloys were exposed to each gas composition for 100 hours at 500°C. Additionally, gas cycle tests were performed where the alloys were exposed to alternating oxidizing and sulfidizing environments at 500°C for 100 hours at 12 hour cycles.

IN622, IN625, and FM72 exhibited parabolic corrosion rates in the sulfidizing atmospheres. The resulting scales consisted of an outer layer of Ni_3S_2 and an inner layer of mixed phases. The alloys performed very well in the oxidizing environments, forming a passive oxide layer on the surface. They also displayed good corrosion resistance in the cyclic atmosphere.

309SS displayed linear corrosion behavior during exposure to the sulfidizing gases. It showed lower weight gains and thinner scale thickness compared to the nickel-base alloys. This alloy also had excellent corrosion resistance in the oxidizing and the cycling atmospheres.

T11 formed non-protective sulfide scales in the sulfidizing gases and exhibited parabolic kinetics. In the oxidizing gas, T11 experienced parabolic kinetics with the

formation of iron oxide on the scale. A mixture of sulfides and oxides were formed in the cyclic atmosphere.

Fe-10wt%Al also formed a non-protective sulfide scale in the sulfidizing gases. Fe-10wt%Al exhibited excellent corrosion resistance in the highly sulfidizing gas in due to the formation of a passive oxide layer. A mixture of iron and aluminum oxides formed in the oxidizing gases. Exposure to the cyclic atmosphere resulted in a mixed oxide/sulfide scale.

A platinum wire catalyst was used in the gases containing both O_2 and SO_2 in order to equilibrate the gases to form SO_3. This reaction enhanced the corrosion of T11 and Fe-10wt%Al and resulted in the formation of thick oxide/sulfide/sulfate scales.

The nickel-base alloys and the stainless steel exhibit good corrosion resistance overall.

1.0 Introduction

The emission of nitrogen oxides (NOx) from the burning of fossil fuels is a major source of environmental hazards such as acid rain and ground-level ozone. In fact, 85% of electric utility nitrogen oxide originates from coal-fired power plants. Therefore, in 1990, the U.S. government passed the Clean Air Act Amendment, which established nitrogen oxide limitations for certain coal-fired utility units. The first stage of the program calls for a reduction in annual NOx emission in the United States by over 1.5 million tons per year beginning in the year 2000 (Phase II)[1].

The formation and emission of nitrogen oxides are inhibited by low operating flame temperatures. Two techniques for combating the NOx emissions in these utilities include the use of low NOx burners and staged combustion. Low NOx burners delay the mixing between the air and fuel to produce a low temperature fuel-rich flame, inhibiting NOx formation. However, delayed mixing results in unburned hydrocarbons and reduced combustion efficiency and can lead to a chemically reducing atmosphere that can corrode the furnace walls. In staged combustion, the air input is substoichiometric in the burner zone. The balance of air is distributed through air ports at a higher elevation to complete the combustion. The process favors the formation of inert N_2 instead of reactive NO.[2,3]

The implementation of low NOx burners in coal-fired boilers has led to a rise in the corrosion rate of the waterwall boiler tubes. Under normal firing conditions, an oxidizing atmosphere, involving such gases as O_2, CO_2, H_2O, SO_2, and SO_3 exists within the boiler, which results in a protective oxide scale on the surface of the tubes, impeding further attack by the gases. However, the use of low NOx technology changes the

combustion environment, resulting in the presence of reducing gases characterized by large amounts of CO and H_2S. In areas of reducing atmospheres, a porous, nonprotective sulfide scale is produced on the waterwalls that have a tendency to flake off and further expose the metal to the gases. This leads to metal loss that can range from 0.5 to 5.0 mm per year (mmpy). In order to understand the mechanisms and kinetics of the gaseous attack, it is necessary to determine the type of environment in which the tubes are exposed.[4]

The gas composition in the boiler is not uniform throughout the furnace and is evident in Figure 1. 1.[5] It can be noted that the gas compositions vary significantly throughout the boiler. The variations in gas compositions play in important role in the corrosion kinetics. For example, the presence of a minute amount of oxygen in a gas containing H_2S may increase the corrosion, because oxygen oxidizes H_2S to elemental sulfur.

Materials solutions to waterwall fireside corrosion problems involve either direct replacement with tubes of a more corrosion-resistant alloy or the application of a corrosion resistant alloy as a coating on the affected tube.[6] Thick protective claddings are much more likely than thin surface coatings to provide long service life and mechanical ruggedness.[7] Therefore, weld overlay claddings have been chosen as the method of corrosion protection in many low NOx boilers.

The purpose of this research is to study the corrosion of weld overlay coatings in Low NOx environments.

2.0 Background

2.1 Oxidation and Sulfidation

The boiler tubes of the furnace are exposed to a highly corrosive environment during operation. The combination of the high temperatures and corrosive gases facilitate the oxidation and sulfidation of the tube metal. The activities of oxygen and sulfur in the atmosphere determine whether oxidation or sulfidation will occur. In order to understand and resolve the problems with the boiler tube failures, the fundamental aspects of gaseous corrosion must be addressed.

2.1.2 Mechanism of Oxidation

Metals are oxidized when heated to elevated temperatures in air or highly oxidizing environments. The reaction between the metal and gas, in this case oxygen, can be written as:

$$aM + (b/2)O_2 \rightarrow M_aO_b$$

This reaction takes place in three stages and is depicted in Figure 2. 1[6]:

1) Adsorption of oxygen gas on the metal surface
2) Formation of individual oxide nuclei which grow laterally to form a continuous oxide film
3) Further growth of the oxide film normal to the surface
4) Formation of microcracks
5) Formation of macrocracks

There are two ways in which molecules can adsorb to the surface: physically and chemically. In physical adsorption, weak van der Waals forces help the gas molecules

bind to the surface. In chemical adsorption, the surface and gas molecules form a chemical bond. Oxygen molecules tend to chemically adsorb on the metal surface by dissociating and adsorbing as atoms[8].

When the metal surface is saturated with adsorbed oxygen atoms and is further exposed to oxygen gas, oxide nuclei form on the surface. In general, oxide atoms tend to nucleate in areas with a high density of atoms and the lowest surface free energy. Such areas include vacancies, kinks, and ledges found on the surface. When the film covers the surface, the reaction proceeds through solid-state diffusion and the oxide grows perpendicular to the surface.

Growth stresses in the scale can cause cavities and microcracks that can eventually grow into larger cracks, exposing the metal to further attack. The continuation of cracking can lead to extremely high corrosion rates, resulting in breakaway corrosion.

As the oxide layer grows, it will either develop as a protective or a non-protective scale. In order for a scale to be protective, it should possess good adherence, good high-temperature plasticity to resist fracture, and low diffusion coefficients for metal and gas ions.[9] A non-protective scale will suffer from pores and cracks that will further expose the base metal to the corrosive atmosphere lead to breakaway corrosion.

2.1.3. Mechanism of Sulfidation

In coal-fired boilers, the sulfidation of the metal occurs in a reducing atmosphere that is characterized by high sulfur/low oxygen potentials. Sulfur in the coal is reduced to H_2S, and the reaction between H_2S and the metal forms a sulfide scale rather than an

oxide. The mechanism of sulfidation is similar to that of oxidation, where the gas metal reaction can be written as

$$aM + (b/2)S_2 \rightarrow M_aS_b$$

However, there are some important differences between oxidation and sulfidation. First, sulfidation is commonly many orders of magnitude faster than oxidation. Also, the morphologies of sulfide scales are often more complex than those characteristic of oxide scales.[10]

2.2 Thermodynamics and Kinetics

2.2.1. Stability Diagrams

Because the combustion of coal results in the formation of both oxidizing and reducing environments, the metal in the boiler tubes is exposed to gases that contain more than one oxidant. A number of different phases may form in the scale depending on both thermodynamic and kinetic considerations.[11] An isothermal stability diagram, Figure 2. 2, is useful for determining the type of oxide or sulfide that forms in the scale. The diagram plots the logarithmic function of the partial pressure of two gases (oxygen and sulfur) on the coordinate axes. The areas within the diagram depict the oxide or sulfide that is thermodynamically stable at those pressures. It should be noted that these diagrams only show the phases that are in equilibrium with the gas pressure, when in actuality, any compound for which the formation pressure is exceeded can be formed. Under equilibrium conditions, the diffusion path for all the phases in the scale can be represented as a line drawn from the point representing the gas atmosphere to the metal phase[12].

However, most alloys used for corrosion protection are composed of multiple alloying elements. For example, at a specific partial pressure of sulfur and oxygen, a metal oxide of alloy A and a metal sulfide of alloy B may both be stable as shown in their respective M-O-S stability diagrams. It is a difficult task to determine whether the oxide or the sulfide phase of alloy AB will be thermodynamically stable at specific sulfur and oxygen pressures due to the lack of experimental data. Therefore, stability diagrams are more useful for showing phase trends as the partial pressures of the gases vary for single metal/gas systems.

2.2.2 Reaction Rates

The kinetics of corrosion can be controlled by several mechanisms:

i) transport and diffusion of the corrosive species to the surface of the metal,

ii) dissociation and adsorption of the gas molecules into the corrosion scale,

iii) growth of the scale by cation and anion diffusion, and

iv) the transfer of metal atoms into the scale[12].

The reaction rate of corrosion can be related mathematically as linear, logarithmic, parabolic, and paralinear (Figure 2. 3[13],[14]). The initial reaction at the gas/metal interface can be described by the linear corrosion rate, which can be equated as:

$$x = k_l t$$

where x represents the weight gain of the metal, k_l is the linear rate constant, and t is time. This relationship describes the corrosion rate as being constant over time and therefore independent of the amount of gas or metal previously consumed in the reaction.

The scale may be porous or cracked, thus allowing the transport of the gas molecules through the scale at faster rates than the chemical reaction. Potassium and Tantalum are examples of metals that oxidize linearly.

It is possible for the reaction between the metal and gas to begin rapidly and then slow down to a negligible rate after a period of time. This relationship can be expressed in terms of the logarithmic rate equation:

$$x = k_{log}\log(Ct + A)$$

where k_{log} is the logarithmic rate constant and C and A are constants. This behavior is characteristic of the oxidation of most metals at ambient or slightly elevated temperatures. In this case, the oxide scale forms as a thin film at a fast rate on the surface of the metal, but once formed, acts as a protective barrier against further corrosion. Aluminum, copper, and iron follow the logarithmic rate law.

At high temperatures the oxidation of many metals follow a parabolic rate, expressed as:

$$x^2 = k_p t + C$$

where k_p is the parabolic rate constant and C is a constant. In this process, the rate-controlling step is the diffusion of ions through the oxide layer. As the oxide becomes thicker, the diffusion distance increases and the oxidation rate decreases. Most metals oxidize according to the parabolic rate law. In later discussion, it is evident that sulfidation also follows this rate.

It is also possible for corrosion to follow a paralinear rate, where the initial corrosion rate appears to be parabolic but then undergoes breakaway corrosion, thus

changing to a linear rate. Metals generally exhibit this behavior at high temperatures due to rapid exothermic reactions on the surface and the loss of a protective coating[14].

The rate at which the scale forms is dependent on numerous factors such as gas pressure, temperature, and elapsed time of reaction. Figure 2. 4[15] shows the effect of temperature and partial pressure of reactive gas on the reaction rate. As the partial pressure of the reactive gas, in this case sulfur, and the temperature increase, the reaction rate of the corrosion increases. The elapsed time of reaction is also a variable in determining reaction rates because short time exposure can give misleading results due to the delayed onset of rapid sulfidation [7].

2.2.3 Diffusion

Diffusion is a key process in the corrosion of metals. It controls the scale formation during the gas-metal reaction. Mass transfer may be the result of the diffusion of metal ions from the metal surface through the oxide to the adsorbed oxygen anions at the oxide/gas interface, or the result of the diffusion of anions inward through the oxide to the metal. The diffusion of atomic oxygen into the metal from the oxide or the gas can also be involved in the process[6].

2.2.3.1 Fick's Laws of Diffusion

Fick's laws of diffusion describe the basics of diffusion. They are based on a two component system at a constant temperature and pressure, with the net movement of the atoms in only one direction. The first law states that the rate of the diffusion of atoms is proportional to the concentration gradient:

$$J = -D(\partial c/\partial x)$$

where J is the flux of atoms diffusing per second through a unit cross section in the concentration gradient ($\partial c/\partial x$), and D is the diffusion coefficient, or diffusivity, in square centimeters per second. D is a function of the diffusing atoms, the structure through which they are diffusing, and the temperature.

The temperature dependence of the diffusivity of a metal can be expressed as:

$$D = D_o \exp(-Q/RT)$$

where D_o is a constant called the frequency factor that is a function of the diffusing species and the diffusion medium, Q is the activation energy for diffusion, R is the gas constant, and T is the absolute temperature. From this equation, it can be noted that diffusion generally increases as temperature increases.

Values for the diffusivities of selected oxides and sulfides are given in Table 2. 1[10]. It is apparent that the diffusivities are several orders of magnitude greater in sulfides than in corresponding oxides. This is reflective in the much higher sulfidation rates that have been observed.

2.3 Corrosion Resistance in Oxidation and Sulfidation

The main concept in establishing corrosion resistant alloys for the use in low NOx boilers is to concentrate on the stabilization of oxide surface scales on the alloy. The renewal of a protective oxide layer by further oxidation of the substrate metal is an essential feature of reactive metal coatings. Effective coatings must therefore have the capability of re-establishing a stable oxide film even in only slightly oxidizing environments[7].

Chromium oxide (Cr_2O_3) is a favored oxide due to its ability to stay intact within a large temperature range (300-1200°C) and its resistance to sulfidation[16]. Because Cr_2O_3 is a highly protective oxide, chromium is a very important alloying element in improving the corrosion resistance of metals. Additions of 9-27% chromium have been observed to improve the oxidation resistance of alloys, and it has been noted that a chromium level between 16-20% is required to develop a continuous Cr_2O_3 scale to protect against further attack. Figure 2. 5[6] illustrates the effect of chromium content in Fe-Cr alloys. The oxidation of chromium generally follows a parabolic rate, and it is apparent that the rate constants of Fe-Cr alloys decrease with increasing chromium content[17].

The rate of sulfidation in Fe-Cr alloys is also dependent on chromium content. Figure 2. 6[18] shows a plot of the parabolic sulfidation rates of Fe-Cr alloys as a function of chromium composition. At low chromium concentrations, (Region I), the scale consisted of FeS. At chromium contents up to 40%, a scale consisting of a mixture of iron and chromium sulfides was formed. It was observed that at chromium concentrations between 4 and 80%, the sulfidation rate of Fe-Cr significantly decreases. A minimum corrosion rate was reported at 70-80% Cr where the scale consisted of a single layer of chromium sulfide with trace amounts of iron.

From the above results, it is possible to develop sulfidation resistant alloys by the inhibition of reactive gases through a sulfide barrier layer formation. In this situation in an alloy of type AB ([B]<[A]) the objective is to choose element B such that it will

undergo selective or partial selective sulfidation and develop as a dominant protective inner barrier layer BS within the duplex (AS + BS) sulfide scale[10].

For example, Mrowec et. al[19] observed the sulfidation behavior of nickel-chromium alloys. From Figure 2. 7[19], it is evident that sulfidation resistance increases with increasing chromiuim content, and those alloys possessing more than 20% chromium experienced relatively low sulfidation rates. Table 2. 2 lists the parabolic rate constants for the sulfidation process. The greatest difference in the sulfidation parabolic rate constants exceeds four orders of magnitude for the alloys containing 0.11 and 62.0% chromium; therefore, the chromium content has an essential influence on the sulfidation rate of nickel. Table 2. 3 gives the composition of the sulfide scales formed on the Ni-Cr alloys. It can be noted that the corrosion resistance of the Ni-Cr alloys is due to the formation of a protective layer of Cr_2S_3. This layer formed on alloys containing more than 40% chromium had better protective properties than on pure chromium, due to the lower defect concentration[19].

A similar effect is seen in Fe-Cr alloys. Figure 2. 6 represents the effect of chromium concentration on the sulfidation rate of Fe-Cr alloys. However, instead of forming a protective Cr_2S_3 layer on the metal surface, the scale consists of a solid solution FeS-Cr_2S_3. Table 2. 4 gives the sulfidation parabolic rate constants of the Fe-Cr alloys. A comparison of this data and that given in Table 2. 2 shows that the rate constants of the Fe-Cr alloys is larger by two orders of magnitude than those for the Ni-Cr alloys. From diffusivity values listed in Table 2. 1, it is apparent that the presence of iron (in the form of iron sulfide) in the Cr_2S_3 scale significantly increases the corrosion

rate of the iron-base alloy. The diffusivity of $Fe_{1-x}S$ is three and a half times larger than the diffusivity of Cr_2S_3. Though the FeS-Cr_2S_3 scale provided some protection against corrosion, Cr_2O_3 is much more effective[18].

Chou and Daniel[2] studied the corrosion resistance of several alloys, both iron and nickel-base, under typical low NOx conditions. The alloys were exposed to complex gas mixtures (H_2S, H_2, O_2, CO, CO_2, H_2O, N_2), which varied from reducing to oxidizing, for 1000-4000 hours at temperatures up to 482°C. In general, the alloys with higher chromium contents had good corrosion resistance in all of the environments. The stainless steels performed better than the carbon steels. The nickel-base alloys, specifically Inconel 671, suffered even less attack than the stainless steels due to its higher chromium content. In the reducing environments, the stainless steels formed an outer layer of iron sulfide and an inner layer containing both FeS and Cr_2O_3. The corrosion layer formed on Inconel 671 was a very thin oxide layer and lacked an outer sulfide layer. The inner oxide layer formed on the high-chromium alloy was enriched with Cr_2O_3 that acted as a barrier against cation diffusion and prevented the formation of an outer sulfide layer.

Corrosion resistance should not be judged on chromium content alone. Hsu et. al.[20] also studied the sulfidation of several iron and nickel-base alloys in a reducing complex gas at 650°C. The compositions of each alloy are listed in Table 2. 5[20]. Even though the nickel-base alloys investigated possessed a high amount of chromium, they suffered very high weight losses (see Table 2. 6[20]). The stainless steels had better corrosion resistance than the Inconel alloys; however, Armco 18SR suffered the least

amount of corrosion overall. The thin, adherent corrosion scale formed on Armco 18SR was mainly chromium sulfide with small amounts of iron and aluminum or their sulfides. The poor resistance of the Inconel alloys might be due to poor adherence of the scale, which further exposes the base metal to the corrosive atmosphere. Additionally, the phases present in the scale (nickel sulfides) have a melting temperature of 685°C, which is very close to the test temperature[20].

2.4 Corrosion in Low NOx environments.

2.4.1. Corrosion in H_2S

Because H_2S plays a dominant role in the waterwall corrosion of low NOx boilers, many studies have been done on the effects of iron-base alloys in H_2-H_2S gas mixtures. Kung and Eckhart[21] studied the performance of various iron-base alloys in H_2S containing gases. Several low carbon, low alloy, and stainless steels were tested in three different complex gases characterized by CO_2, CO, H_2, N_2, H_2S and H_2O. These gases varied in H_2S composition. The samples were exposed to each gas atmosphere for 1000 hours at 500, 700, and 900°C. The low carbon and low alloy steels suffered greater corrosion rates than the stainless steels. It was also observed that the corrosion rates increased with increasing test temperature, resulting in corrosion rates as high as 18 mils per year (mpy) at 900°C. The corrosion scales formed on these alloys consisted mainly of an outer iron sulfide layer and an inner mixed layer of iron oxide and iron sulfide. The stainless steels exhibited corrosion rates of less than 4mpy at all test temperatures. The corrosion product, though thinner than the carbon and low alloy steels, was also comprised of a multi-layered product with iron sulfide as the outer layer and a thin,

continuous layer of chromium oxide underneath. As stated previously, the formation of chromium oxide is very important in the corrosion resistance of alloys. The high chromium content present in the stainless steel accounts for the good corrosion resistance exhibited.

Early studies performed by Haycock[22] helped determine the mechanism of corrosion of iron and low alloy steels in H_2-H_2S environments. The corrosion rates of several low alloy steels were investigated at temperatures between 400 and 550°C. The scales formed on all of the alloys consisted of two layers - an outer porous layer and an inner compact layer. Both layers were mainly iron sulfide. The corrosion kinetics were described as following a parabolic-linear rate law. Haycock states that because the outer scale is porous, the main resistance to corrosion would be found in the inner barrier layer. Since the formation of the inner layer grows by the diffusion of the sulfide ions to the metal surface, this process accounts for the parabolic corrosion kinetics. The linear component of the rate law is associated with the process occurring at the interface between the compact and the porous scale layers. Haycock states that the porous outer scale is formed by the depletion of sulfide ions from the inner layer and accounts for the linear corrosion kinetics.

Schulte et al[23]studied the sulfidation of several steels: unalloyed C-steel (ferritic), 1Cr-0.5Mo steel(ferritic), 12Cr-1Mo-0.25V steel (ferritic) and 18Cr-10Ni-Ti steel (austenitic). The carbon steel and the 1Cr-0.5Mo steel had similar corrosion products form on their surfaces. The outer layer of the scale was a coarse-grain, nonadherent FeS layer. The inner layer was a fine grain, porous FeS layer with traces of Cr and Mo found

in the 1Cr-0.5Mo steel. The 12Cr-1Mo-0.25V steel had a similar two-layer scale with traces of Cr found in the outer FeS layer and an inner layer enriched with 24-27% Cr. Grain boundary attack was observed in all three alloys. The corrosion layer formed on the 12Cr-10Ni-Ti steel had a third layer of $FeCr_2S_4$ in between the outer and inner FeS layers. Additionally, traces of Cr and Ni were detected in the outer FeS layer. Figure 2. 8[23] shows a schematic describing the development of iron sulfide during the corrosion of the ferritic steels in H_2S. The sulfidation of the steel begins with the formation of a pore-free sulfide layer (A). During the growth of the sulfide layer, pores begin to form at the metal/scale interface, specifically at the grain boundaries of the sulfide layer (B). An inner layer of FeS enriched with Cr begins to form (C). The internal stresses in the outer sulfide layer cause its detachment (D). Finally, a new FeS layer forms on top of the porous inner layer (E). The outer sulfide layer grows by the outward diffusion of Fe ions while the inner layer grows by the inward sulfur transport along pores. The overall gas-metal reaction can be represented as

$$Fe + H_2S = H_2 + FeS$$

The kinetics of the corrosion of the ferritic steels follows a linear relationship, meaning that the rate controlling step in the process is the constant delivery rate of H_2S at the inner surface of the detached layer[23].

The kinetics of the corrosion of the austenitic steel followed parabolic kinetics, which indicates that solid-state diffusion is the rate controlling step. The formation of the compact $FeCr_2S_4$ layer is responsible for the decrease in sulfidation rate of the alloy[23]. This further supports the importance of chromium in the corrosion resistance of alloys.

The corrosion of commercial steels in H_2-H_2S and H_2-H_2S-CO_2 gas mixtures was also investigated by Gesmundo et. al[24]. The partial pressure of sulfur for both gas compositions was the same. The corrosion scales that formed in both atmospheres were typical to those described above. No oxide scales were formed in the CO_2 containing gases. The formation of the duplex scales followed irregular kinetics that involved an initial stage of decreasing (parabolic) rate and a second stage of linear behavior. Gesmundo et. al explain that the initial parabolic kinetics observed occur by the growth of the outer scale by the outward diffusion of iron, while the inner layer grows by the inward penetration of sulfur. After some time, the outer layer becomes increasingly non-protective due to the formation of cracks and pores from internal stresses (as seen in Figure 2. 8). The growth mechanism of the scale at this stage becomes complex and involves different simultaneous processes - the outward diffusion of iron through FeS, the inward penetration of H_2S through pores, and the reaction between the H_2S and the metal. The scale growth eventually is controlled by gas transport within the scale. The combination of these processes leads to a generally linear overall reaction rate[24].

2.4.2 Cyclic Oxidation and Sulfidation

The effects of alternating oxidizing and reducing atmospheres have also been an interest in determining the corrosion resistance of alloys. Chou and Daniel[2] have examined the effects of alternating gas conditions at temperatures between 700 and 900°C in various iron-base alloys, including carbon and stainless steels. An increase in the corrosion rate of carbon steel (compared to the constant sulfidation tests) was observed under these conditions. In the reducing conditions, iron sulfide is the stable

phase formed while in the oxidizing gases, Fe_2O_3 and Fe_3O_4 are stable. The alternating gas conditions transform the sulfide into oxide and vice versa, which results in a porous, nonadherent scale. The stainless steels experienced a decrease in corrosion rates compared to their behavior in the reducing atmosphere. This observation can be attributed to the formation of stable chromium oxide during the transient oxidation periods.

Gesmundo et al. studied the corrosion of commercial steels in cycling conditions at both 500 and 600°C[25,26]. In the study at 500°C, C18 (0.012C), T22 (2.22Cr-0.89Mo-0.09C) and T9 (8.84Cr-0.89Mo) steels were exposed to alternating oxidizing (1%O2, 0.%SO2, balance N2) and reducing (H2-1%H2S) environments over a span of four days, with one day per cycle. Higher weight gains were observed during the tests with the initial sulfidizing cycle. The resulting microstructures contained mainly iron-sulfides, though a discontinuous oxide layer was apparent in parts of the scale. During a reducing cycle, the oxide layers formed previously were thermodynamically unstable and transformed into sulfides. However, the sulfide layers were not converted into oxides during an oxidizing cycle. Because the sulfide layers are porous and have low self-diffusivities, the iron ions can rapidly diffuse through the sulfide to react with the oxidizing gas. The overall kinetics are controlled by the nature and thickness of the various layers formed during each cycle[25,26].

2.5 Summary

Waterwall wastage in low NOx boilers is still a major concern for utility companies. Weld overlay coatings have been the chosen technique for combating fireside corrosion of boiler tubes. However, effective corrosion resistant alloys are necessary in order to provide long-term protection. By understanding how variables such as gas composition and temperature effect the mechanism and kinetics of corrosion in reducing atmospheres, more efficient alloys can be identified. Additional research needs to be done in the areas of alternating compositions in order to develop a definite relationship between the corrosion rates and the scale morphologies resulting. From this, it may be possible to determine a better approach to reducing boiler tube wastage.

References

[1] "Nitrogen Oxide Emissions Reduction." Environmental Protection Agency website: http://www.epa.gov.

[2] S.F. Chou and P.L. Daniel. "Hydrogen Sulfide Corrosion in Low-NOx Combustion Systems." High Temperature Corrosion in Energy Systems, Ed. M. Rohman, TMS, 1985, pp. 327-343.

[3] R. Whitaker. "Trade-offs on NOx Control," EPRI Journal, January/February, 1982, pp. 18-25.

[4] P.L. Daniel and L.D. Paul. "Estimating Effects of Chloride on Fireside Corrosion of Furnace Walls on Coal-Fired Boilers," Materials Performance, February, 1989, pp. 41-45 .

[5] F. Clarke and C. Morris. "Combustion Aspects of Furnace Wall Corrosion," in Corrosion Resistant Materials for Coal Conversion Systems, Ed. Meadowcroft and Manning, Applied Science Publishers, 1983, pp. 47-61.

[6] Metals Handbook, Vol. 13, Corrosion. 1987, pp.61-76.

[7] G. Sorrell, M.J. Humphries, E. Bullock, and M. Van de Voorde. "Materials Technology Constraints and Needs in Fossil Fuel Conversion and Upgrading Processes," International Metals Reviews, Vol. 31, No. 5, 1986, pp. 765-779.

[8] P. Kofstad. High Temperature Corrosion. Elsevier Applied Science, 1988.

[9] M. Fontana. Corrosion Engineering. McGraw-Hill, 1986.

[10] K. Strafford and P. Datta. "Design of Sulfidation Resistant Alloys." Materials Science and Technology, Vol. 5, 1989, pp. 765-779.

[11] N. Birks and G. Meier. Introduction to High Temperature Oxidation of Metals. Edward Arnold, 1983.

[12] H.J. Grabke. "Definition and Preparation of Gas Atmosphere" in Guidelines for Methods of Testing and Research in High Temperature Corrosion. Ed. Grabke and Meadowcroft, Institute of Materials, London, 1995, pp. 62-84.

[13] S. Mrowec, T. Werber. Gas Corrosion of Metals. National Bureau of Standards and the National Science Foundation, Washington, D.C. 1978.

[14] W. Smith. Principles of Materials Science and Engineering. McGraw-Hill, 1990.

[15] M. Danielewski, S. Mrowec, A. Stoklosa. "Sulfidation of Iron at High Temperatures and Diffusion Kinetics in Ferrous Sulfide." Oxidation of Metals, Vol. 17, no.1/2, 1982, pp.77-97.

[16] G. Lai. "Meeting the Challenge of Materials Development for Coal Combustion Plants," Materials at High Temperatures, Vol. 11, NO. 1-4, 1993, pp. 143-150.

[17] G. Lai. High-Temperature Corrosion of Engineering Alloys, ASM International, 1990.

[18] S. Mrowec, T. Walec, T. Werber. "High-Temperature Sulfur Corrosion of Iron-Chromium alloys," Oxidation of Metals, Vol. 1, no.1, 1969, pp. 93-119.

[19] S. Mrowec, T. Werber, and M. Zastawnik. "The Mechanism of High Temperature Sulfur Corrosion of Nickel-Chromium Alloys," Corrosion Science, Vol. 6, 1996, pp. 47-68.

[20] C.H. Hsu, P. Gillis and R. DeAngelis. "High Temperature Sulfidation of Six Alloys." Journal of Materials for Energy Systems, Vol. 1, 1979, pp. 15-24.

[21] S. Kung and C. Eckhart. "Corrosion of Iron-Base Alloys in Reducing Combustion Gases." NACE Corrosion '93, Paper #242, 1993.

[22] E. W. Haycock. " High-temperature Sulfiding of Iron Alloys in Hydrogen Sulfide-Hydrogen Mixtures." Journal of the Electrochemical Society, Vol. 106, no. 9, 1959, pp. 764-771.

[23] M. Schulte, A. Rahmel, M. Schutze. "The Sulfidation Behavior of Several Commercial Ferritic and Austenitic Steels." Oxidation of Metals, Vol. 49, no. 1/2, 1998, pp. 33-70.

[24] F. Gesmundo, F. Viani, W. Znamirowski, K. Godlewski, F. Bregani. "The Corrosion of Iron and of Three Commercial Steels in H_2-H_2S and in H_2-H_2S-CO_2 gas mixtures at 400-700°C." Werkstoffe und Korrosion, Vol. 43, 1992, pp. 83-95.

[25] F. Gesmundo, F. Viani, and G.P. Toledo. "The Corrosion of Three Commerical Steels in Chemically Cycling Conditions at 500°C." The Institute of Materials (UK), 1993, pp.825-832.

[26] F. Gesmundo, C. Roos, D. Oquab, and F. Viani. "The Corrosion at 600°C of Four 8-12% Cr Ferritic Steels in Chemically Cycling Oxidizing-Sulfidizing Gases Started with Sulfidation." High Temperature Materials and Processes, Vol. 17, no. 3, 1998, pp.145-153.

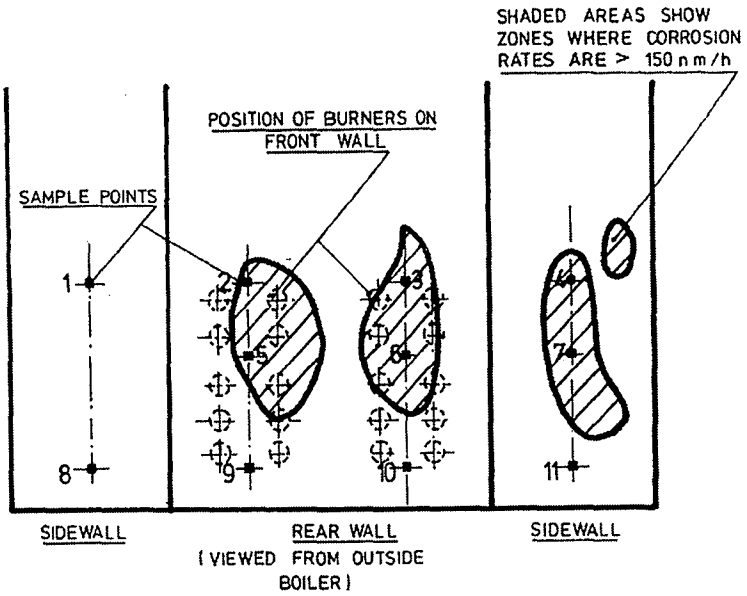

		SAMPLE POINT NUMBER :										
	GAS	1	2	3	4	5	6	7	8	9	10	11
	O_2 %	10·8	4·1	NIL	1·2	NIL	NIL	1·1	8 9	8·6	6·2	6·1
	CO %	0·02	0·02	4·2	0·8	2·7	4·3	0·61	0·03	0·06	0·005	0·03
	SO_2 VPM	490	800	900	1200	800	1000	1600	600	400	700	1000
	H_2 %	NIL	NIL	1·08	0·20	0·70	1·23	0·12	NIL	NIL	NIL	NIL
	H_2S PPM	NIL	NIL	>300	TRACE	TRACE	>300	NIL	NIL	NIL	NIL	NIL
(1)	HC VPM	NIL	NIL	6	6	2	3	NIL	NIL	NIL	NIL	NIL
	HCl PPM	150	265	377	303	385	470	410	287	230	239	225
(2)	HCl_C PPM	159	246	425	316	407	425	404	266	267	320	286
	SOLID											
	Combustibles %	2·9	8·2	14·6	50·8	24·5	42·3	12·4	2·5	2·4	5·7	7·8
	Cl %	0·11	0·03	0·13	0·15	0·21	0·13	0·15	0·03	0·07	0·08	0·10
	S %	0·59	0·49	0·50	0·48	0·77	0·60	0·46	0·28	0·27	0·42	0·33

(1) HC is total hydrocarbon gases concentration.

(2) HCl_C is calculated HCl concentration from coal composition.

Figure 1. 1: The composition of gases and solids reaching the furnace walls of a 120 MW boiler.

Table 2. 1: Self-diffusion coefficients of cations D_{Me} in some metal oxides and sulfides

Table 4 Selfdiffusion coefficients of cations D_{Me} in some metal oxides and sulphides[27]

Sulphide	Temperature, °C	D_{Me}, $cm^2 s^{-1}$	Oxide	Temperature, °C	D_{Me}, $cm^2 s^{-1}$
$Cu_{2-x}S$	650	$5{\cdot}15\times10^{-5}$	$Cu_{2-x}O$	1000	$1{\cdot}7\times10^{-8}$
$Co_{1-x}S$	720	$7{\cdot}0\times10^{-7}$	$Co_{1-x}O$	1000	$1{\cdot}9\times10^{-9}$
$Ni_{1-x}S$	800	$1{\cdot}4\times10^{-8}$	$Ni_{1-x}O$	1000	$1{\cdot}0\times10^{-11}$
Cr_2S_3	1000	$1{\cdot}0\times10^{-7}$	Cr_2O_3	1000	$1{\cdot}0\times10^{-12}$
$Fe_{1-x}S$	800	$3{\cdot}5\times10^{-7}$	$Fe_{1-x}O$	800	$1{\cdot}3\times10^{-8}$
Al_2S_3	600	$1{\cdot}0\times10^{-13}$	Al_2O_3	1000	$1{\cdot}0\times10^{-15}$
NbS_2	800	$1{\cdot}6\times10^{-12}$	...	...	...

Table 2. 2: Parabolic rate constants for the sulfidation process of nickel-chromium alloys ($g^2cm^{-4}min^{-1}$).

TABLE 3. PARABOLIC RATE CONSTANTS FOR THE SULPHIDATION PROCESS OF NICKEL–CHROMIUM ALLOYS ($g^2cm^{-4}min^{-1}$)

Chromium, Wt. %	Temperature								
	520°C	560°C	600°C	650°C	700°C	750°C	800°C	850°C	900°C
0·11	$6{\cdot}0.10^{-8}$	$1{\cdot}2.10^{-6}$	$2{\cdot}2.10^{-4}$	—	—	—	—	—	—
1·1	$2{\cdot}5.10^{-8}$	$4{\cdot}7.10^{-7}$	$7{\cdot}6.10^{-6}$	—	—	—	—	—	—
4·5	$1{\cdot}6.10^{-8}$	$5{\cdot}4.10^{-8}$	$1{\cdot}6.10^{-6}$	$6{\cdot}1.10^{-5}$	$2{\cdot}2.10^{-4}$	—	—	—	—
13·3	—	—	$4{\cdot}0.10^{-7}$	$1{\cdot}4.10^{-6}$	$5{\cdot}0.10^{-6}$	$1{\cdot}3.10^{-5}$	$5{\cdot}0.10^{-6}$	—	—
21·8	—	—	$3{\cdot}1.10^{-7}$	$5{\cdot}4.10^{-7}$	$9{\cdot}0.10^{-7}$	$1{\cdot}3.10^{-6}$	$5{\cdot}5.10^{-6}$	$2{\cdot}0.10^{-5}$	—
32·6	—	—	$2{\cdot}0.10^{-7}$	$3{\cdot}4.10^{-7}$	$5{\cdot}6.10^{-7}$	$7{\cdot}0.10^{-7}$	$2{\cdot}4.10^{-6}$	$1{\cdot}3.10^{-5}$	$4{\cdot}5.10^{-5}$
42·8	—	—	$1{\cdot}4.10^{-7}$	$2{\cdot}2.10^{-7}$	$3{\cdot}7.10^{-7}$	$5{\cdot}0.10^{-7}$	$1{\cdot}6.10^{-6}$	$7{\cdot}2.10^{-6}$	$2{\cdot}4.10^{-5}$
53·0	—	—	$7{\cdot}6.10^{-8}$	$1{\cdot}2.10^{-7}$	$1{\cdot}7.10^{-7}$	$2{\cdot}8.10^{-7}$	$9{\cdot}5.10^{-7}$	$1{\cdot}7.10^{-6}$	$5{\cdot}2.10^{-6}$
82·0	—	—	$5{\cdot}2.10^{-8}$	$1{\cdot}0.10^{-7}$	$2{\cdot}1.10^{-7}$	$3{\cdot}8.10^{-7}$	$1{\cdot}3.10^{-6}$	$2{\cdot}8.10^{-6}$	$3{\cdot}2.10^{-5}$
Cr	-	—	—	—	$2{\cdot}4.10^{-8}$	$3{\cdot}6.10^{-8}$	$6{\cdot}3.10^{-8}$	$8{\cdot}3.10^{-8}$	$1{\cdot}6.10^{-6}$

Table 2. 3: Phase composition of sulfide scales formed on nickel-chromium alloys.

TABLE 5. PHASE COMPOSITION OF SULPHIDE SCALES FORMED ON NICKEL–CHROMIUM ALLOYS

Chromium Wt. %	Sulphidation temperature °C	Outer layer	Inner layer
0·0	600	α-NiS $Ni_{3+x}S_2$*	α-NiS $Ni_{3+x}S_2$*
0·11	600	α-NiS $Ni_{3+x}S_2$*	α-NiS $Ni_{3+x}S_2$*
4·5	700	α-NiS	α-NiS Cr_2S_3
13·8	800	α-NiS	α-NiS Cr_2S_3
32·8	750	α-NiS NiS_2*	Cr_2S_3 α-NiS*
32·8	850	α-NiS	Cr_2S_3 α-NiS*
63·0	850	Cr_2S_3	Cr_2S_3
63·0	750	Cr_2S_3	Cr_2S_3
82·0	900	Cr_2S_3	Cr_2S_3
82·0	750	Cr_2S_3	Cr_2S_3
100	900	Cr_2S_3	Cr_2S_3

*Low concentration of marked phase.

Table 2. 4: Parabolic rate constants for the sulfidation process of Fe-Cr alloys.

Cr, at.%	Temperature, °C						
	700	750	800	850	900	950	1000
0.35	2.6×10^{-4}	4.3×10^{-4}	6.8×10^{-4}	1.0×10^{-3}	1.4×10^{-3}	—	—
1.1	2.4×10^{-4}	3.9×10^{-4}	6.5×10^{-4}	1.4×10^{-3}	1.0×10^{-3}	—	—
2.2	2.1×10^{-4}	3.5×10^{-4}	6.0×10^{-4}	9.6×10^{-4}	1.4×10^{-3}	—	—
4.0	1.5×10^{-4}	2.7×10^{-4}	2.7×10^{-4}	2.3×10^{-4}	1.2×10^{-3}	1.8×10^{-3}	—
5.1	2.0×10^{-5}	3.0×10^{-5}	3.7×10^{-5}	5.3×10^{-5}	4.0×10^{-4}	1.6×10^{-3}	—
13.0	3.3×10^{-6}	4.1×10^{-6}	6.3×10^{-6}	3.9×10^{-5}	1.8×10^{-4}	6.0×10^{-4}	—
19.4	—	1.4×10^{-6}	4.5×10^{-6}	2.3×10^{-5}	1.1×10^{-4}	2.4×10^{-4}	6.2×10^{-4}
37.3	—	—	3.6×10^{-6}	8.0×10^{-6}	3.3×10^{-5}	9.2×10^{-5}	2.2×10^{-4}
57	—	—	1.4×10^{-6}	6.4×10^{-6}	2.1×10^{-5}	5.5×10^{-5}	1.4×10^{-4}
74	—	—	1.9×10^{-6}	3.5×10^{-6}	8.2×10^{-6}	3.0×10^{-5}	7.3×10^{-5}

[a] Values of k_p'' are given in g^2/cm^4-min.

Table 2. 5: Nominal Compositions of the Test Samples.

Table II. Nominal Compositions of the Test Samples

Alloy	Composition (Wt Pct)											
	C	Mn	Si	Fe	Ni	Cr	Co	Al	Ti	P	S	Mo
Inconel 600	0.05	0.15	0.20	7.0	76.5	15.8	0.08	—	—	—	—	—
Incoloy 800	0.03	0.80	0.33	47.1	30.8	20.6	0.10	0.32	0.42	—	—	—
316 S.S.	0.06	1.65	0.43	65.3	13.9	17.1	—	—	—	—	—	2.5
304 S.S.	0.05	1.45	0.54	70.0	9.1	18.8	—	—	—	—	—	0.34
Armco 18SR	0.05	0.50	1.00	77.52	0.5	18.0	—	2.0	0.4	0.02	0.01	—
1020 C.S.	0.22	0.62	0.20	98.96	—	—	—	—	—	—	—	—

Table 2. 6: Estimated Corrosion Rates.

Table III. Estimated Corrosion Rates

Alloy	Original Thickness		Measured Thickness		Corrosion Rate	
	mm	in.	mm	in.	mm/year	in./year
Inconel 600	3.38	0.133	2.06	0.081	57.5	2.262
Incoloy 800	3.30	0.130	3.10	0.122	8.89	0.350
316 S.S.	1.14	0.045	1.02	0.040	5.56	0.219
304 S.S.	1.42	0.056	1.42	0.052	4.44	0.175
Armco 18SR	0.86	0.034	0.86	0.034	Nil	Nil
1020 C.S.	1.09	0.043	*	*	*	*

*Estimate unavailable.

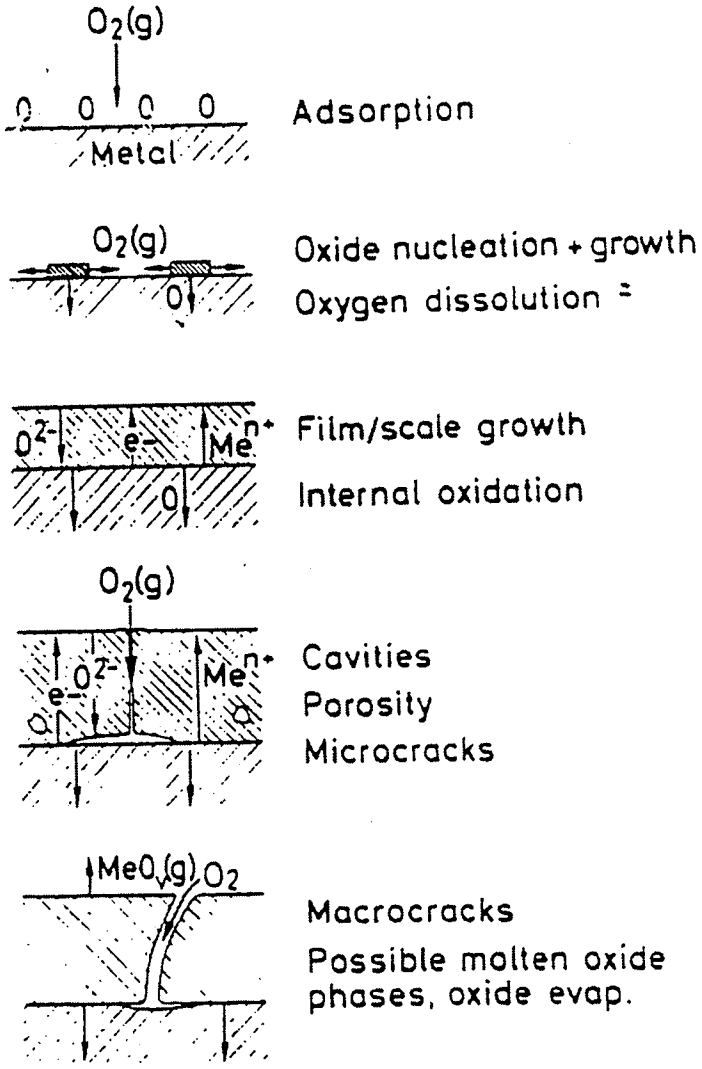

Figure 2. 1: Schematic Illustration of some of the main aspects of metal-oxygen reactions.

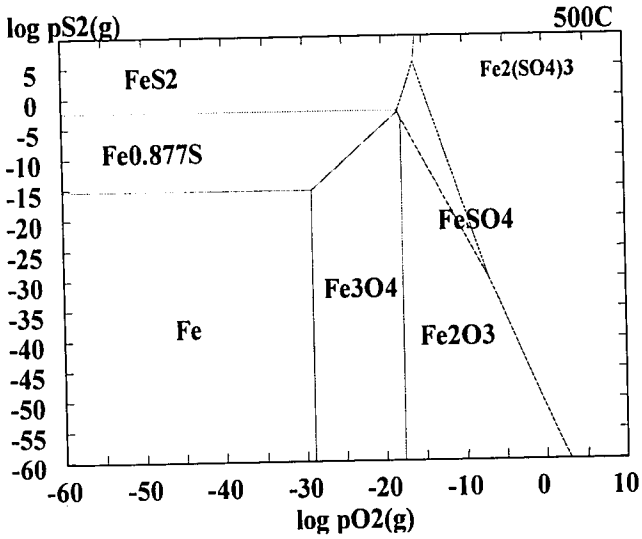

Figure 2. 2: Phase Stability Diagram of Fe-S-O system at 500°C.

a)

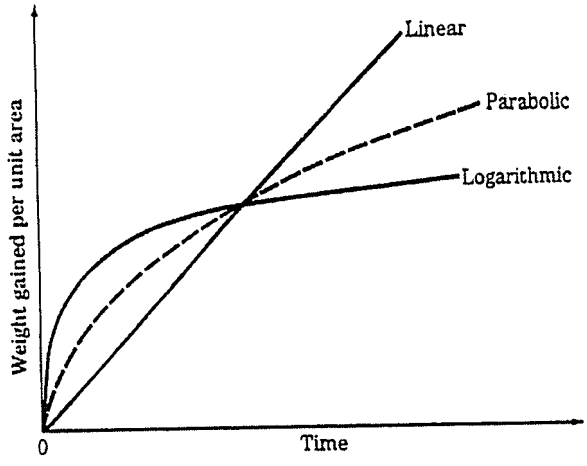

b)

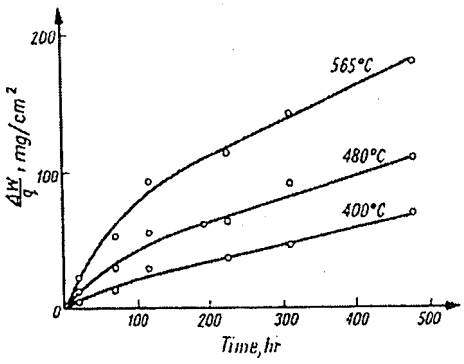

Figure 2. 3: Mathematical Illustration of corrosion rate laws, a) linear, parabolic, and logarithmic, b) paralinear.

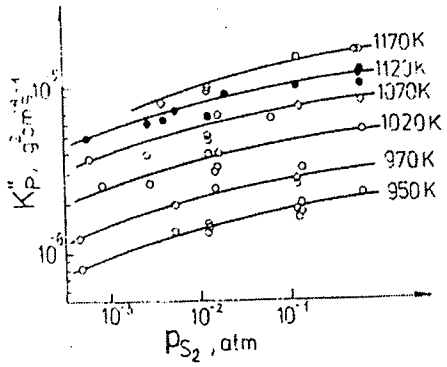

Figure 2. 4: Dependence of the parabolic rate constants of iron sulfidation on sulfur pressure for several temperatures.

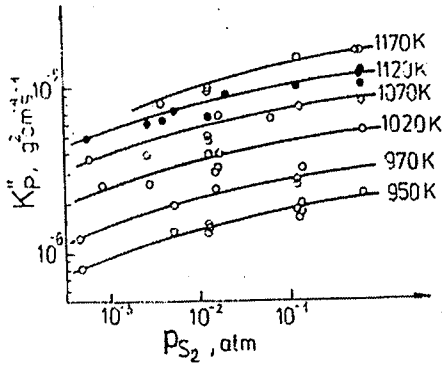

Figure 2. 4: Dependence of the parabolic rate constants of iron sulfidation on sulfur pressure for several temperatures.

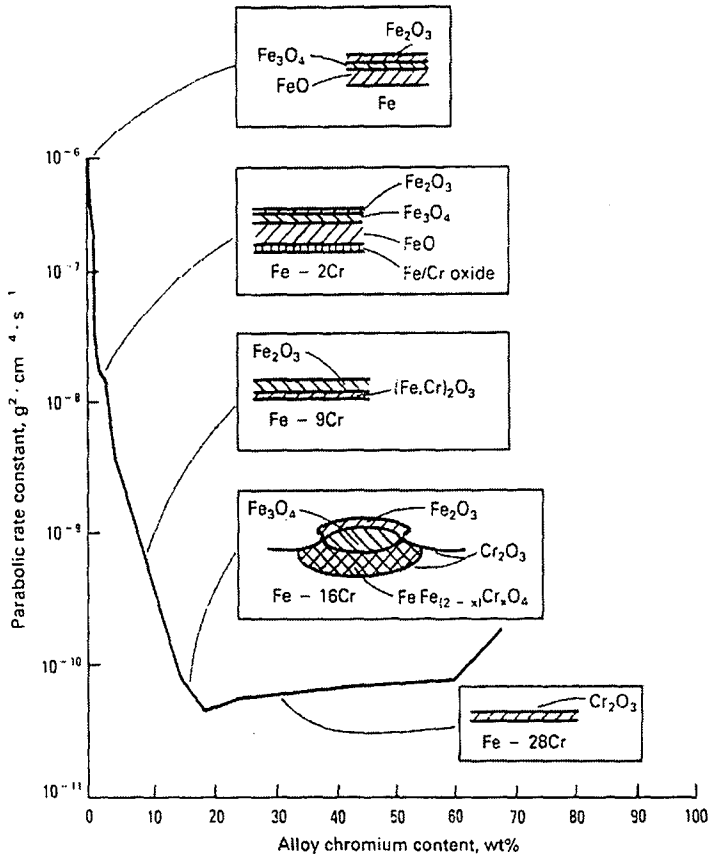

Figure 2. 5: Schematic showing the effect of chromium in Fe-Cr alloys on oxidation rate and oxide scale structure based on isothermal oxidation studies at 1000°C in 0.13 atm O_2.

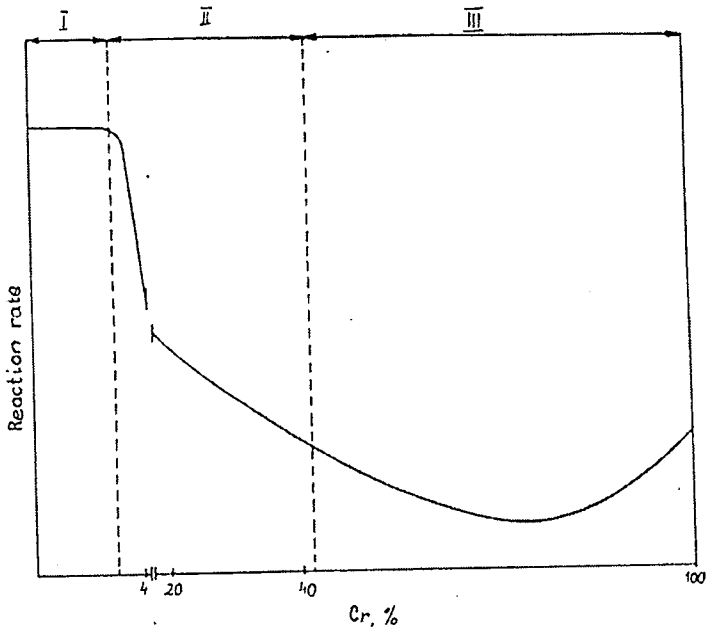

Figure 2. 6: Schematic plot of the sulfurization of rate of Fe-Cr alloys as a function of chromium concentration.

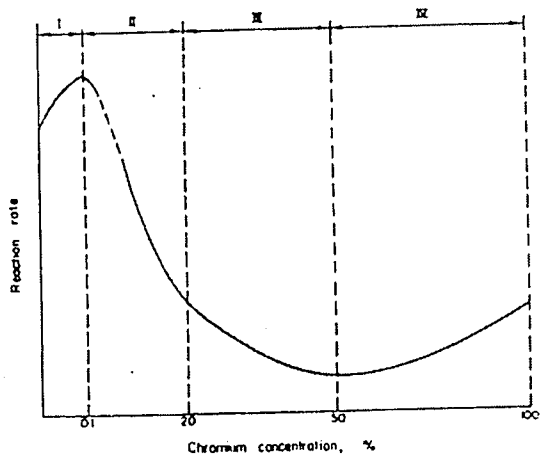

Figure 2. 7: Schematic diagram of the sulfidation rate of Fe-Ni alloys as a function of chromium concentration in the alloy.

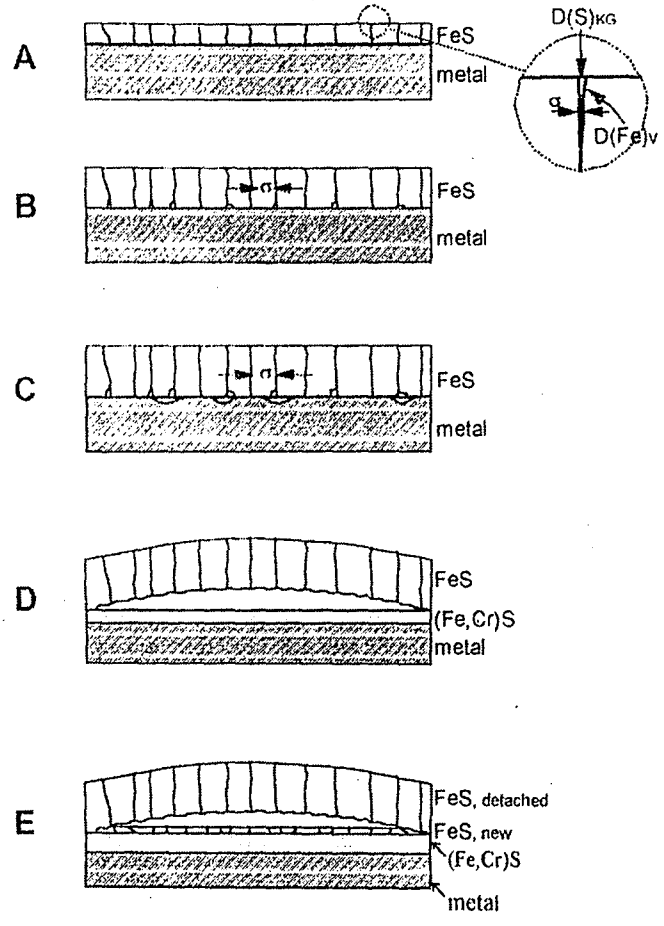

Figure 2. 8: Development of sulfide scales on ferritic steels.

3.0 EXPERIMENTAL PROCEDURES

3.1. Sample Preparation

The materials used in this study are wrought Fe-1.25Cr-0.5Mo steel, cast Fe-10wt%Al, IN622 weld overlay, IN625 weld overlay, FM72 weld overaly, and 309 stainless steel weld overlay. The compositions of the alloys are listed in **Table 3. 1**. The metal was cut into 15mm by 15mm by 5mm specimens using a Struers Accutom 50 high speed cutting wheel. A 2mm hole was drilled through the top-center of each sample in order to place it in the thermogravimetric balance. The surfaces and corners of the samples were ground using 600 grit silicon carbide paper and cleaned in alcohol. They were then measured to the nearest hundredth of a mm using a hand micrometer and weighed to the nearest tenth of a mg with a digital balance.

3.2. Corrosion Testing

A Netzsch STA 409 thermogravimetric balance was used to measure the weight gain of the sample over time. A schematic of the Netzsch is shown in Figure 3.1. A kd Scientific syringe pump was used to inject water into the chamber of the furnace, as seen in Figures 3.2 and 3.3. The point at which the water enters the furnace is at a temperature that is high enough to evaporate the water so it enters the chamber as water vapor. The sample is supsended from the crucible in order to fully expose it to the gases. After the sample is placed in the chamber, the balance is zeroed to the nearest hundredth of a mg. Any traces of oxygen in the furnace chamber can affect the PO_2 of the corrosive gas, specifically in the reducing atmospheres. Therefore, a vacuum is pulled on the furnace, which is subsequently back-filled with ultra high purity argon. This process is

repeated five times in order to get rid of residual air that remains inside the furnace. Afterwards, ultra high purity argon is allowed to flow to the balance at a flow rate of 50mL/min while the corrosive gases flow to the chamber at the same rate. These gases flow through the Netzsch for two hours prior to testing.

The gas compositions used in this study were complex mixtures of H_2, H_2S, CO, CO_2, O_2, SO_2, N_2, and water vapor, H_2O. The mixtures ranged from highly reducing to highly oxidizing. The presence of water vapor is inherent in coal-fired boilers; therefore, it was included in this study. However, it is difficult to include water vapor in a cylinder of mixed gases. Therefore, the gas compositions listed in Table 3. 2 are for dry gases. The flow rates listed in Table 3. 3 were calculated to constantly inject a specific volume of water into the furnace via the kd Scientific syringe pump.. Table 3. 4 shows the final composition of the gases including the moisture content.

Gas 5 consists of various oxidizing species, including O_2 and SO_2. Under equilibrium conditions, the reaction

$$2SO_2(g) + O_2(g) = 2SO_3(g)$$

would occur. In order to obtain the right thermodynamic conditions, a platinum wire catalyst that was placed inside the furnace tube was used to equilibrate the gas mixture (Grabke). Proof of the above reaction presented itself as condensed SO_3 in the reaction chamber.

Each sample was exposed to each gas composition at 500°C for 100 hours. A sample isothermal program is shown in Table 3. 5. Additionally, gas cycle experiments were also performed on the samples. The specimens were exposed to alternating

oxidizing and sulfidizing gases, beginning with the oxidizing gas, at twelve-hour intervals for 96 hours. Compositions 5 and 3 were used in these experiments. A sample program is seen in Table 3. 6. After the furnace cooled to room temperature, the samples were removed and weighed to the nearest tenth of a mg.

3.3. Characterization

Macroscopic digital color photographs of the specimens were taken using an Olympus SZH10 Stereoscope. The corrosion scales were then characterized using the Rigaku Rotaflex x-ray unit. The x-ray spectra produced were compared to those obtained from the Powder Diffraction File (PCPDF-WIN) in order to identify the phases of the scales. The samples were then mounted in cold setting epoxy. Once set, the samples were ground to a 600 grit finish using silicon carbide paper and then polished to a 0.1 μm finish using colloidal silica.

Photomicrographs of the cross sections of the samples were taken using the Reichert-Jung MeF3 metallograph. The thickness of the scales was measured using a Nikon Microphot light optical microscope and the LECO imaging program. 50 measurements were taken of each layer on each sample. Further characterization of the scales was performed using the energy dispersive spectroscopy system on the JEOL 6300F scanning electron microscope at 25eV.

Table 3. 1: Compositions of alloys studied, wt%

Overlay Sample	Fe	Ni	Cr	Others
Fe-1.0Cr-0.5Mo	Balance		1.25	0.5Mo
Fe-10Al	Balance			10Al
309SS	Balance	11	21	2.0Mn-0.83Si-0.03C
IN625	8.2	Balance	20	8.4Mo-3.4Nb
IN622	7	Balance	20	14.0Mo-3.0W
FM72	6	Balance	39	---

Table 3. 2: Gas compositions in volume percent as received from Scott Specialty Gases

Gas Component	Gas 1	Gas 2	Gas 3	Gas 4-a	Gas4-b	Gas 5
O_2	---	---	---	1.042	1.042	2.1
CO	15	13.1	10.2	2.08	2.08	
CO_2		2	5.1	13.54	13.54	16
H_2	3	2.5	---	---	---	---
H_2S	0.12	0.12	0.12	0.125	---	---
SO_2	---	---	---	---	0.125	0.13
N_2	Balance	Balance	Balance	Balance	Balance	Balance

Table 3. 3: Flow rates of Syringe Pump into furnace

Final % H_2O in gas	Flow Rate (μL/hr)
0.50%	12
2.0%	48
4.0%	96
6.0%	145

Table 3. 4: Gas Compositions in volume percent with variable moisture

Gas Component	Gas 1	Gas 2	Gas 3	Gas 4	Gas5
O_2	---	---	---	1	2
CO	15	13	10	2	---
CO_2		2	5	13	15
H_2	3	2.5	---	---	6
H_2O	---	0.5	2	4	---
H_2S	0.12	0.12	0.12	0.06	---
SO_2	---	---	---	0.06	0.12
N_2	81.88	81.68	82.88	79.88	76.88
log PO_2	-27.9	-23.2	-19.2	-16.9	-1.7
log PS_2	-6.3	-3.3	-8.6	-13.2	-45.6

Table 3. 5: Temperature program for 100hr isothermal hold at 500°C

Temperature Segment	Rate (K/min)	Temperature (°C)	Time
Initial		20	
Dynamic (heating)	50	500	10 min
Isothermal		500	100 hrs
Dynamic (cooling)	20	20	20 min
Emergency Shut Off Temperature		550	

Table 3. 6: Temperature program for 12 hour gas cycle experiments

Temperature Segment	Rate (K/min)	Temperature (°C)	Time	Gas
Initial		20		5
Dynamic (heating)	50	500	10 min	5
Isothermal		500	12hrs	5
Isothermal		500	12hrs	3
Isothermal		500	12hrs	5
Isothermal		500	12hrs	3
Isothermal		500	12hrs	5
Isothermal		500	12hrs	3
Isothermal		500	12hrs	5
Isothermal		500	12hrs	3
Dynamic (cooling)	20	20	20 min	3
Emergency Shut Off Temperature		550		

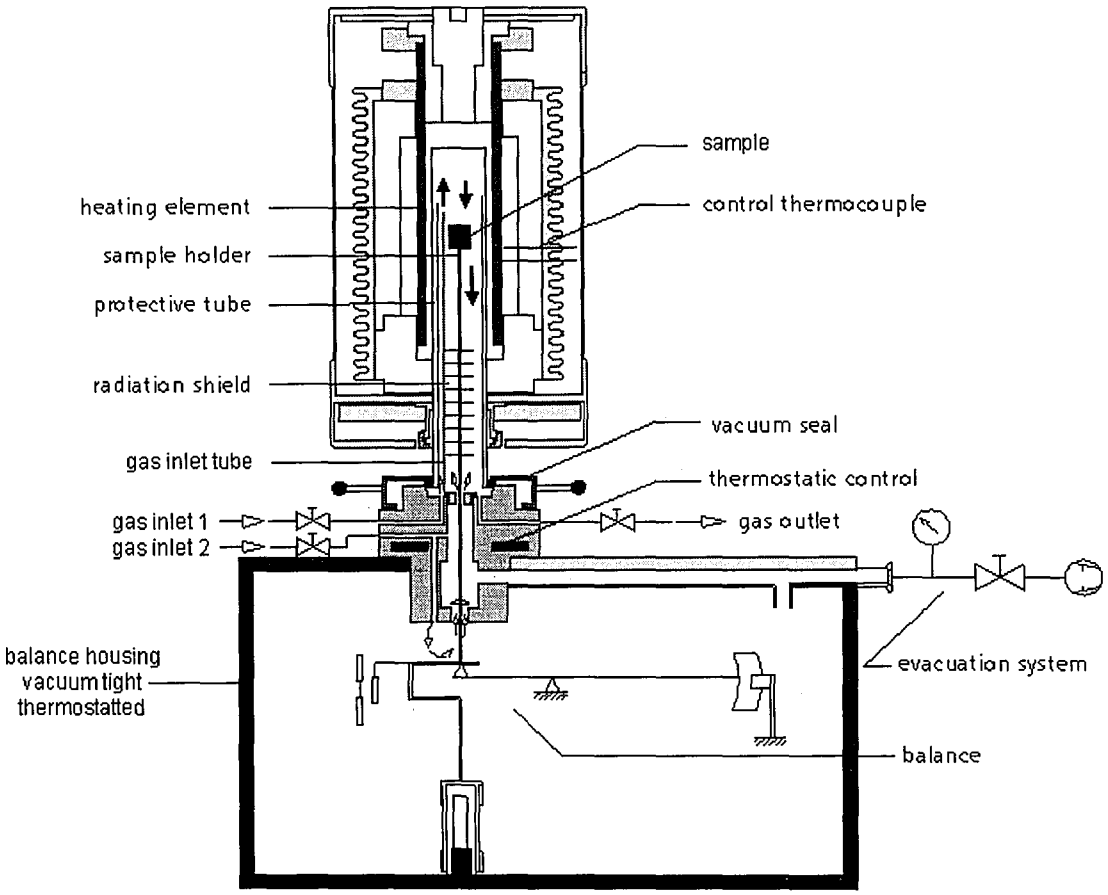

Figure 3.1. Schematic of Netzsch STA 409 thermogravimetric balance

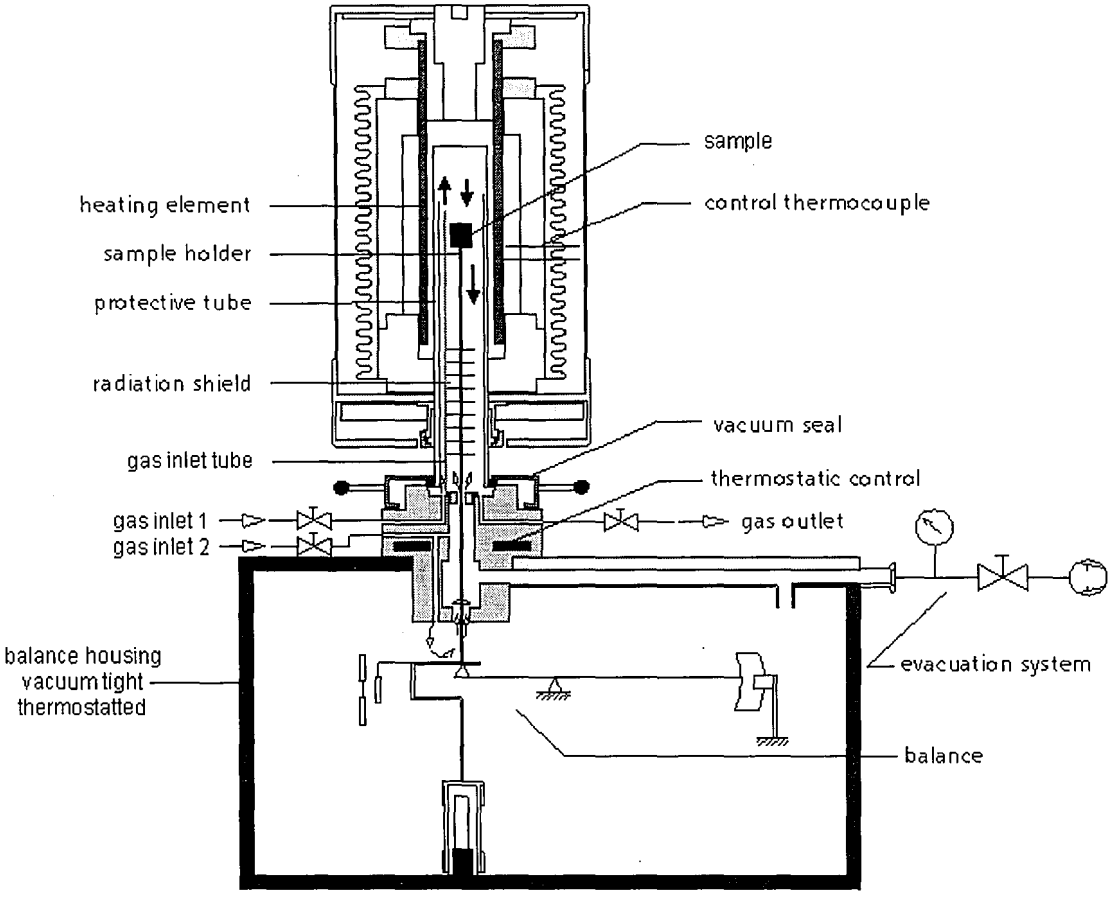

Figure 3.1. Schematic of Netzsch STA 409 thermogravimetric balance

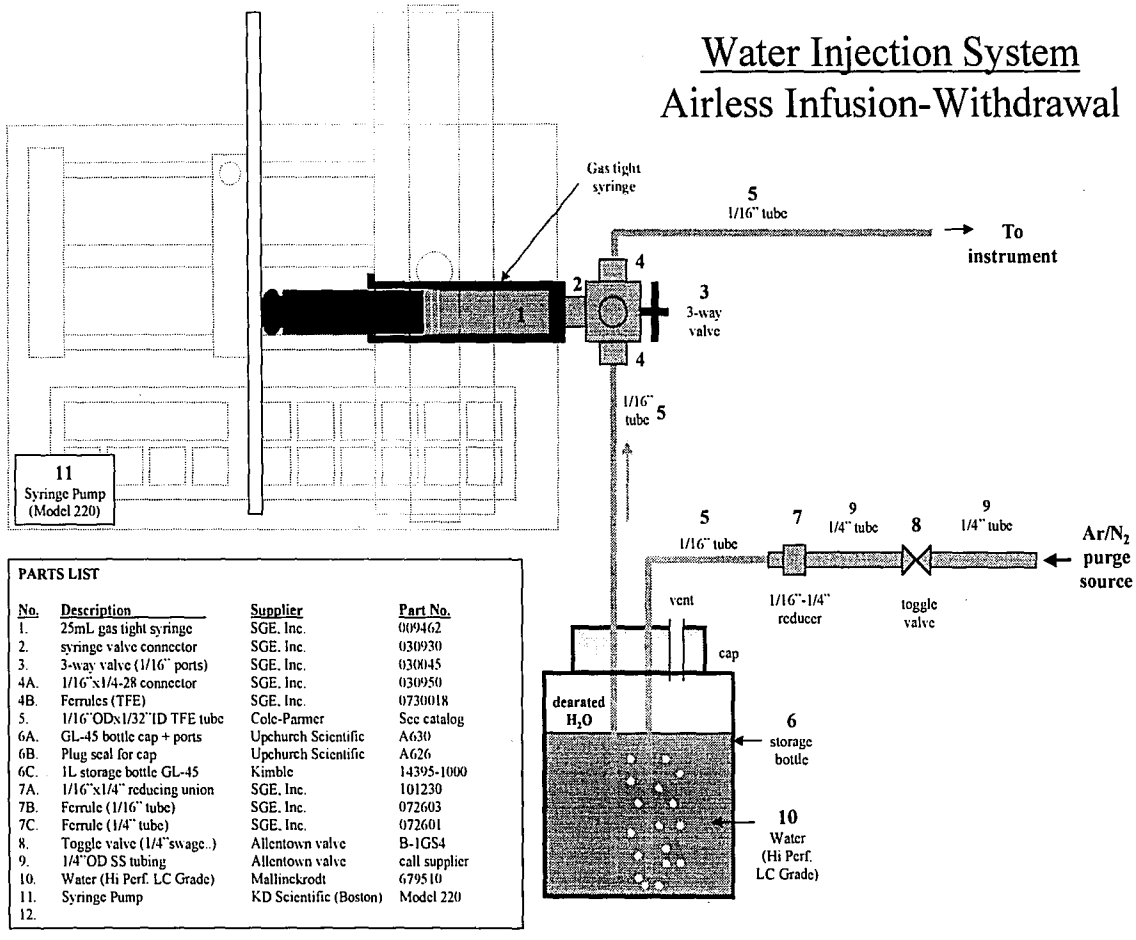

PARTS LIST

No.	Description	Supplier	Part No.
1.	25mL gas tight syringe	SGE, Inc.	009462
2.	syringe valve connector	SGE, Inc.	030930
3.	3-way valve (1/16" ports)	SGE, Inc.	030045
4A.	1/16"x1/4-28 connector	SGE, Inc.	030950
4B.	Ferrules (TFE)	SGE, Inc.	0730018
5.	1/16"ODx1/32"ID TFE tube	Cole-Parmer	See catalog
6A.	GL-45 bottle cap + ports	Upchurch Scientific	A630
6B.	Plug seal for cap	Upchurch Scientific	A626
6C.	1L storage bottle GL-45	Kimble	14395-1000
7A.	1/16"x1/4" reducing union	SGE, Inc.	101230
7B.	Ferrule (1/16" tube)	SGE, Inc.	072603
7C.	Ferrule (1/4" tube)	SGE, Inc.	072601
8.	Toggle valve (1/4"swage..)	Allentown valve	B-1GS4
9.	1/4"OD SS tubing	Allentown valve	call supplier
10.	Water (Hi Perf. LC Grade)	Mallinckrodt	679510
11.	Syringe Pump	KD Scientific (Boston)	Model 220
12.			

Figure 3.2 Schematic of syringe pump.

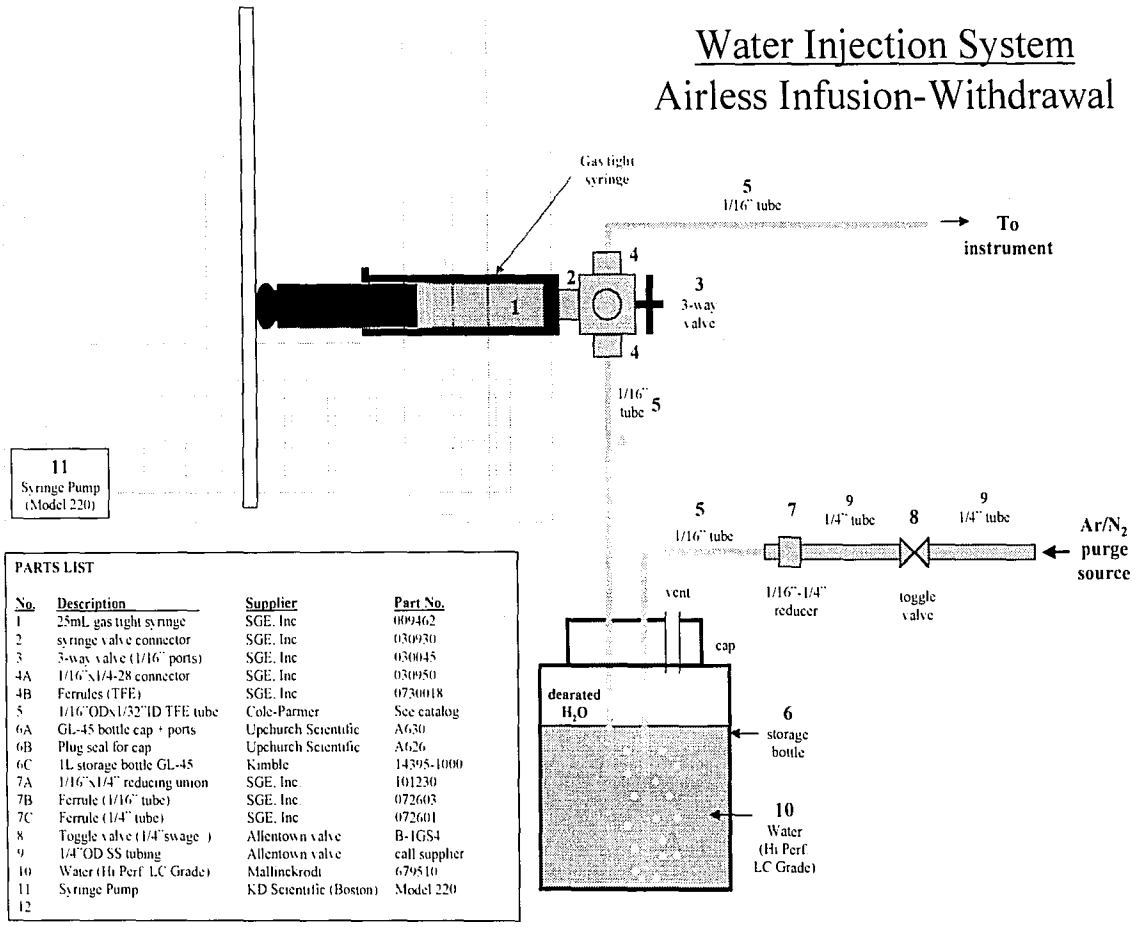

PARTS LIST

No.	Description	Supplier	Part No.
1	25mL gas tight syringe	SGE. Inc	009462
2	syringe valve connector	SGE. Inc	030930
3	3-way valve (1/16" ports)	SGE. Inc	030045
4A	1/16"x1/4-28 connector	SGE. Inc	030950
4B	Ferrules (TFE)	SGE. Inc	0730018
5	1/16"ODx1/32"ID TFE tube	Cole-Parmer	See catalog
6A	GL-45 bottle cap + ports	Upchurch Scientific	A630
6B	Plug seal for cap	Upchurch Scientific	A626
6C	1L storage bottle GL-45	Kimble	14395-1000
7A	1/16"x1/4" reducing union	SGE. Inc	101230
7B	Ferrule (1/16" tube)	SGE. Inc	072603
7C	Ferrule (1/4" tube)	SGE. Inc	072601
8	Toggle valve (1/4"swage)	Allentown valve	B-1GS4
9	1/4"OD SS tubing	Allentown valve	call suppher
10	Water (Hi Perf LC Grade)	Mallinckrodt	679510
11	Syringe Pump	KD Scientific (Boston)	Model 220
12			

Figure 3.2 Schematic of syringe pump.

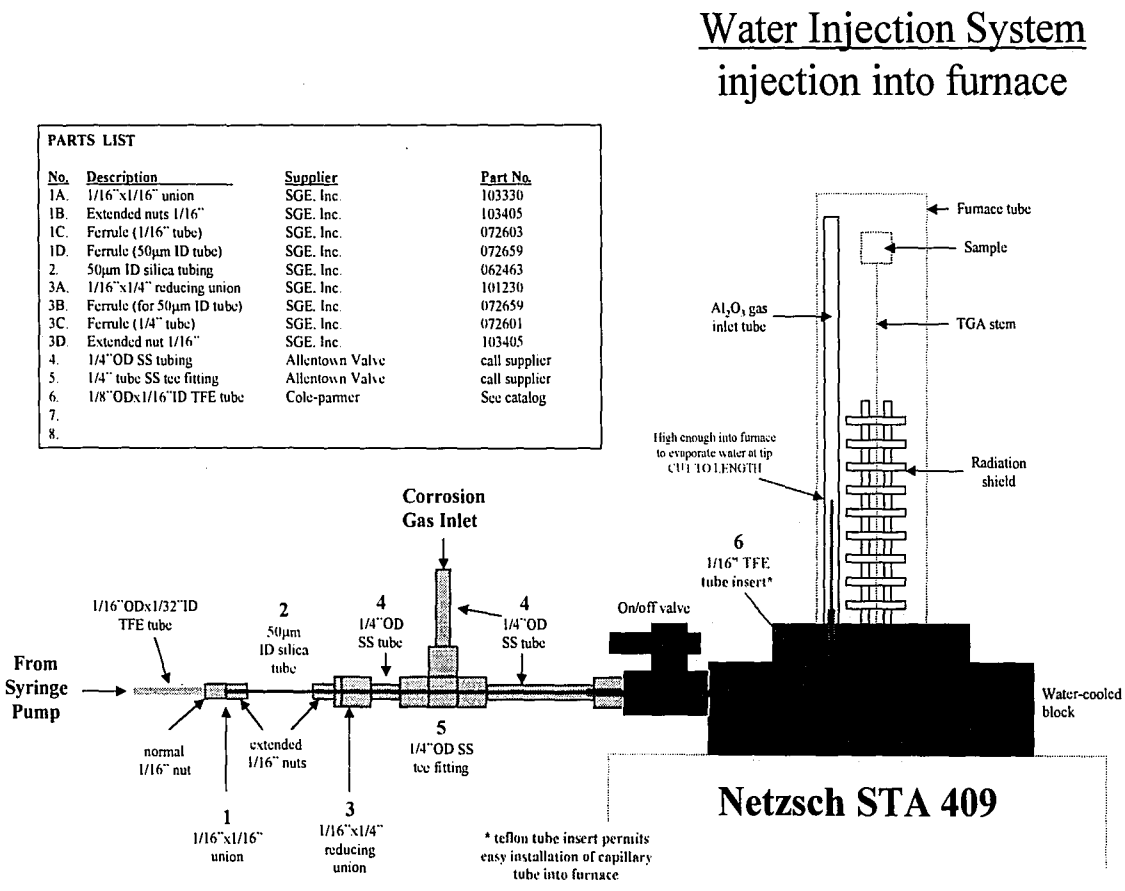

Figure 3.3: Schematic of the addition of moisture into the furnace.

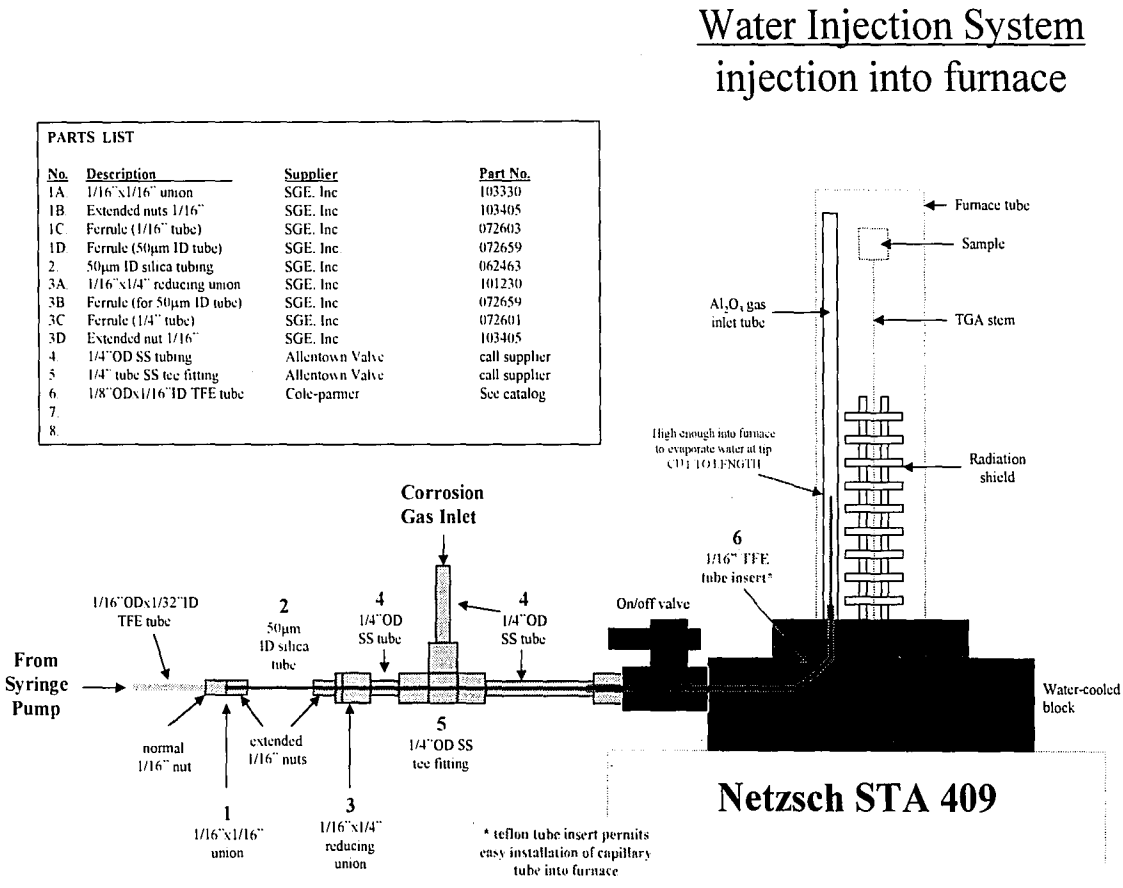

Figure 3.3: Schematic of the addition of moisture into the furnace.

4.0 Results and Discussion

Figures 4.1-4.4 show the M-S-O phase stability diagrams for iron, nickel, aluminum, and chromium. The phase stability diagrams for the Fe-S-O and the Ni-S-O systems predict that at 500°C gas compositions 1 and 2 will be sulfidizing gases, due to the low PO_2. Gas composition 3 lies in a sulfide phase field in the Ni-S-O system, but in an oxidizing area in the Fe-S-O system. The Cr-S-O and Al-S-O phase stability diagrams predict the formation of oxides in Gases 1, 2, and 3 in the systems. These stability diagrams represent the phases formed in a pure element. The addition of alloying elements may shift the phase field boundaries. In all of the M-S-O systems depicted, oxides are predicted to form in Gas 4 and sulfates are anticipated to form in Gas 5. In this discussion, Gases 1,2, and 3 will be referred to as sulfidizing gases, and 4 and 5 will be oxidizing gases.

4.1 Sulfidizing Gases (1,2,3)

Light optical macrographs of the samples after 100 hours exposure to the sulfidizing gases are shown in Figure 4.5 and 4.6. The scales formed on the nickel-base alloys (IN622, IN625, FM72) generally consist of a non-uniform outer dark, powder layer and an inner, more adherent yellow crystalline layer. However, IN625 and FM72 exposed to Gas 1 lack the dark powder on their surfaces. FM72 appears to have the least amount of powder formed on its surfaces. The Fe-Cr alloy (309SS) possessed a dark, adherent corrosion product from exposure to Gases 1 and 2. In Gas 3, the scale formed on the specimen was thin and flaky. The iron base (T11) alloy formed a flaky, yellow

corrosion scale in all three gas compositions. The iron aluminide also formed a similar corrosion product in Gases 2 and 3. However, a very thin, dark surface formed on the alloy in Gas 1.

4.1.1 Microstructures and Kinetics

4.1.1.1 Nickel-base alloys

Light optical micrographs of the nickel-base alloys exposed to the sulfidizing gases are seen in Figures 4.7, 4.8, and 4.9. The microstructures of each alloy are very similar, with an outer yellow layer and an inner, porous gray layer. Some dendrite attack is apparent in IN622 and IN625 for all of the sulfidizing gases, but not in FM72. The scales formed on IN622 and IN625 are thicker than those formed on FM72. The scale thickness ranged from 35-60μm for IN622 and IN625. FM72 had scales that ranged from 21-40μm thick. X-ray diffraction (Figure 4.10) shows the presence of Ni_3S_2 in the scale of IN625 exposed to Gas 2. Because all of these alloys are similar in composition, Ni_3S_2 most likely makes up the outer, yellow layer of the corrosion product for all of the alloys. X-ray diffraction performed on FM72 exposed to Gas 3 showed the appearance of more peaks than seen in IN625 in Gas 2 (Figure 4.11). Table 4.2 lists all of the possible phases that match each peak in Figure 4.11. Because of the amount of alloying elements present in the nickel-base alloys, it is possible to form several different phases within the corrosion scale. Additionally, the IN625 possesses a thicker scale than FM72; therefore, x-ray diffraction was only able to detect the Ni_3S_2 phase on surface of the IN625 sample.

The corrosion kinetics of the sulfidation of the nickel-base alloys are plotted as weight gain vs. time, as seen in Figures 4.12 – 4.14. The Inconel alloys exhibited

parabolic behavior, with n-values ranging from 0.49 to 0.6. However, they also experienced relatively higher weight gains compared to FM72. The sulfidation of FM72 also reflected corrosion kinetics that are close to parabolic. The n-values attained for Gases 1, 2, and 3 were 0.58, 0.38, and 0.7 respectively.

4.1.1.2 Fe-Cr alloy

Light Optical micrographs of the cross section of 309SS after exposure to Gases 1 and 3 are seen in Figure 4.15. Corrosion in Gas 2 was very similar to Gas 1. The corrosion scale formed in Gas 1 is more adherent than that formed in Gas 3. The outer layer formed in Gas 3 was thin and flaky, which caused its separation from the corrosion product. The thickness of the scales formed ranged from 27 – 29 μm. A very small amount of attack of the substrate is apparent in the alloy exposed to Gas 1. X-ray diffraction (Figure 4.16) indicates that exposure to all sulfidizing gases resulted in the formation of an outer layer of $Fe_{1-x}S$ and an inner layer of $FeCr_2S_4$. The outer iron sulfide layer forms by the outward diffusion of Fe ions an its reaction with the sulfur in the gas. The inner, spinel layer forms by the inward diffusion of S ions and its reaction with the iron and chromium found in the alloy.

A plot of weight gain vs. time for 309 SS exposed to the sulfidizing gases at 500°C is shown in Figure 4.17. The determined n-values that reflect the reaction kinetics are in between linear and parabolic. The n-values range from 0.7 to0.83 in the sulfidizing atmospheres. The final weight gained after 100 hours was generally lower than T11 and the Inconel alloys. The close-to-parabolic kinetics and lower weight gains observed can be contributed to the formation of the compact $FeCr_2S_4$ layer than forms between the base

metal and the $Fe_{1-x}S$ layer. This spinel layer may act as a passive layer and accounts for the diffusion-controlled kinetics.

4.1.1.3. Fe-base alloy

Cross sections of T11 exposed to Gases 1 and 3 are shown in Figures 4.18 and 4.19. Corrosion of T11 in Gas 2 is very similar to that in Gas 3. Both microstructures exhibit a non-adherent, coarse grained outer scale and a fine-grained, more adherent inner scale. The scale thickness of the alloy exposed to Gas 1 was 70μm, while in Gases 2 and 3, the thickness of the scales were measured to be 37 and 35μm respectively. The x-ray spectrum shown in Figure 4.20 indicates that the outer layer of the scale consists of $Fe_{1-x}S$. Work done by Schulte et al. identified an enrichment of Cr and Mo of $Fe_{1-x}S$ at the metal-scale interface of sulfidized low alloy steels. This area was darker in color than the pure $Fe_{1-x}S$ and penetrated the grain boundaries. Based on this information, the interface between the scale and the base metal shown in Figures 4.18 and 4.19 may be enriched with Cr and Mo. The outer $Fe_{1-x}S$ layer formed by the outward diffusion of iron ions and the reaction between iron and sulfur at the interface. The inner, fine-grained scale was formed by the inward diffusion of sulfur ions and the reaction between the base metal and sulfur. Penetration of the grain boundaries of the alloy is apparent in Figure 4.19.

A plot of weight gain vs. time for T11 exposed to the sulfidizing gases is seen in Figure 4.21. Exposure to Gas 1 resulted in the highest weight gain after 100 hours. The corrosion kinetics followed behavior in between parabolic and linear, with $n = 0.79$. From Figure 19, it appears that the kinetics initially follow a parabolic rate until 50 hours,

where the weight gain vs. time remains constant. This reflects a parabolic to linear transition. Exposure to Gases 2 and 3 seem to follow a similar trend in kinetics, with n=0.6 and 0.66 respectively. These kinetics imply that initially, the rate controlling step is the diffusion of the ions through the corrosion scale. However, with time, the iron sulfide scale cracks and allows easy transport of the ions, thereby changing the rate-controlling step to the adsorption of the gas in the metal.

4.1.1.3 Fe-10wt%Al

Light optical micrographs of the cross section of Fe-10Al exposed to Gas 1 is shown in Figure 4.22. From the photomicrograph, the formation of a protective layer, which is around 2μm thick, is apparent. The scale formed was too thin to examine using x-ray diffraction. From the phase stability diagrams, FeS and/or Al_2O_3 would be expected to form in this gas composition. Banovic et. al.[1] reported that Fe-10wt%Al exposed to a simple reducing gas ($PO_2 = 10^{-25}$, $PS_2 = 10^{-4}$ atm) at 500°C for 100 hours formed a thin, protective Al_2O_3 layer. Even though Gas 1 is a highly sulfidizing gas, the PO_2 and PS_2 are comparable to that used by Banovic et. al.; therefore, the scale seen in Figure 4.22 is most likely Al_2O_3.

A cross section of the specimen exposed to Gas 3 is seen in Figure 4.23. Corrosion in Gas 2 was very similar. The scale thickness was measured to be 30μm. Two layers are apparent in the corrosion scale. X-ray diffraction performed on the outer, non-adherent layer indicates the presence of $Fe_{1-x}S$. The inner, more adherent layer could not be examined using XRD. However, studies by Banovic et. al.[1] suggest the formation of an $FeAl_2S_4$ spinel layer below the iron sulfide. Therefore, the mechanism of scale

formation is similar to the sulfidation of 309SS, with the outward diffusion of iron ions and the inward diffusion of sulfur.

The corrosion kinetics of the sulfidation of Fe-10w%Al are plotted in Figure 4.24. The sample exposed to Gas 1 gained very little weight while exposure to Gas 2 and 3 resulted in linear kinetics, with n=0.9. In Gas 1, the specimen formed a protective oxide layer that inhibited further attack. However, in Gases 2 and 3, the formation of a non-protective iron sulfide layer resulted higher weight gains.

4.2 Oxidizing Gases (4,5)

Light optical macrographs of the specimens after 100 hours exposure to Gases 4 and 5 (Pt catalyzed) are shown in Figures 4.25 and 4.26. From these macrographs, it appears that any scale that formed on the nickel-base (IN622, IN625, and FM72) and the Fe-Cr (309SS) alloys is only visible in the form of discoloration. In Gas 4, IN622, IN625, and FM72 appear to have areas of yellow and brown on their surfaces. In Gas 5 (Pt Catalyzed), IN625 and FM72 appear darker in color than IN622. The 309SS samples exposed to both Gas 4 and 5 appear to have an orange tint to them. The surface marks from the 600 grit SiC paper are still apparent on the all of these specimens, indicating very little corrosion.

In Gas 4, a red, adherent scale appears on the both the T11 and the Fe-10wt%Al samples. This is indicative of the formation of an iron oxide layer in the corrosion scale. In Gas 5 (Pt catalyzed), both alloys formed a thick, brittle corrosion scale on their surfaces that are white in color.

4.2.1. Microstructures and Kinetics

4.2.1.1. Nickel-base alloys

A cross section of FM72 exposed to Gas 5 (Pt catalyzed) for 100 hours at 500°C is seen in Figure 4.27. This microstructure is typical of all of the nickel-base alloys exposed to Gases 4 and 5. In the oxidizing environments, all three nickel-base alloys experienced very little weight gain and possessed very thin scales. This is indicative of the formation of a protective oxide on the surface of the samples. Because of the high alloy content of these alloys, the layer formed is most likely a protective oxide.

Figure 4.28 shows a plot of the weight gain vs. time for FM72 exposed to Gases 4 and 5. This plot is also representative for IN622 and IN625 in these gases. The weight gain of each sample was very small and ranged from 0.05 to 0.2 mg/cm^2. The formation of a protective oxide layer supports these very low weight gains.

4.2.1.2. Fe-Cr alloy

309SS also experienced similar corrosion resistance in Gases 4 and 5 (Pt catalyzed). Figure 4.29 shows the cross section of 309SS exposed to Gas 4. Again, a very thin oxide layer formed on the surface, and because of the high chromium content in the alloy, it is most likely a protective Cr_2O_3 layer.

A plot of the weight gain vs. time is shown in Figure 4.30. The weight gain of the sample in the oxidizing gases ranged from 0.1 to 0.17 mg/cm^2. Therefore, the formation of a protective oxide prevented further weight gain.

4.2.1.3. Fe-base alloy

A photomicrograph of the cross section of T11 after 100 hours exposure to Gas 4 is seen in Figure 4.31. A similar scale microstructure is formed in Gas 5 (non-catalyzed). The scale thickness was measured at 26μm. Four main oxide layers are apparent in the scale, an outer red layer, a thin intermediate light colored layer, an compact gray layer, and a cracking, less adhesive inner layer. Some slight grain boundary attack is apparent. X-ray diffraction (Figure 4.32) shows the presence of Fe_2O_3 on the surface of the sample. Under equilibrium conditions, the diffusion path for all of the phases in the scale can be represented in the phase stability diagram as a line drawn from the point representing the gas atmosphere to the metal.[2] Therefore, from Figure 4.31, the phase that is thermodynamically stable at 500°C is Fe_2O_3 (outer red layer). Looking at the phase stability diagram in Figure 4.1, the diffusion path from Fe_2O_3 to Fe would include the formation of Fe_3O_4, which makes up the intermediate gray layers.

The microstructure of the cross section of the sample exposed to Gas 5 (Pt catalyzed) is shown in Figure 4.33. The scale thickness is 31μm. Three main layers are apparent in the corrosion scale – a brittle, red outer layer, a thin, lighter colored layer, and an inner, cracked gray layer. X-ray diffraction was performed on the sample to determine the phases present. The spectrum obtained is shown in Figure 4.34, and Table 4.6 lists the possible phases that match up with the x-ray peaks. From this data, it appears that both sulfides and oxides have formed the corrosion scale of the specimen, even though the PS_2 for Gas 5 is very low. However, the phase stability diagram shown in Figure 4.1

indicates that Gas 5 is a sulfating gas, which explains the presence of sulfur in the corrosion scale.

The plot of weight gain vs. time for T11 exposed to Gases 4 and 5 (catalyzed and non-catalyzed) are shown in Figure 4.31. In Gas 4 and 5 (non-catalyzed), the corrosion kinetics are close to following parabolic behavior, with n=0.41. This corrosion pattern can be observed in the plot where the weight gain gradually decreases with time. This type of behavior is representative of the formation of a passive oxide layer, where the kinetics are controlled by diffusion of the oxidizing species through the oxide. This is supported by the microstructure seen in Figure 4.33. The corrosion kinetics of the sample exposed to Gas 5 are near parabolic behavior, with n = 0.6. This is again supported by the formation of a passive oxide layer, seen in the microstructure. The effect of the catalysis of Gas 5 on the corrosion reaction will be discussed later.

4.2.1.4. Fe-10wt%Al

A photomicrograph of the cross section of Fe-10wt%Al exposed to Gas 4 and Gas 5 (non-catalyzed) is shown in Figure 4.36. The microstructures look very similar. However, the scale formed in Gas 5 (non-catalyzed) is not continuous and is much thinner than that formed in Gas 4. Several corrosion layers are apparent, but not all of them are continuous throughout the specimen. The thickness of the scale is relatively thin at 14 μm. EDS was performed on the sample to determine the elements present in each layer of the scale. An SEM image of the sample area where energy dispersive spectroscopy (EDS) was performed is shown in Figure 4.37. The spectra obtained for points A and B are seen in Figures 4.38 and 4.39. Figure 4.38 shows the presence of iron

and oxygen in the outer layer of the scale. EDS of the inner layer shows a mixture of iron and aluminum oxides present.

The microstructure of the corrosion scale of the sample exposed to Gas 5 (Pt catalyzed) is seen in Figure 4.40. Four main layers are apparent within the scale – an outer, chunky layer, a thin, light colored layer, an intermediate gray layer, and an inner, multiphase layer that somewhat attacks the substrate. The scale thickness was measured to be 17μm. Figure 4.41 and Table 4.7 show the possible phases formed in the scale. Additional analysis using (EDS) indicates the presence of iron, aluminum, oxygen, and sulfur within the scale (Figures 4.42-4.45). Therefore, the scale may consist of a mixture of oxides, sulfides, or sulfates. In both the Fe-S-O and the Al-S-O phase stability diagrams, Gas 5 lies the sulfating region. Therefore, sulfur attack is possible even with the very low PS_2 of the gas.

The weight gain vs. time for Fe-10wt%Al exposed to Gases 4 and 5 (catalyzed and non-catalyzed) are plotted in Figure 4.46. The alloy experienced relatively low weight gains in Gases 4. The kinetics follow a linear rate law in Gas 4, with n = 1.0. From the microstructure, it is apparent that the oxide layers formed in this environment are not protective, and the rate-controlling step is the adsorption of the oxidizing species and their reaction with the substrate. The corrosion rate in Gas 5 (non-catalyzed) is parabolic, with n=0.55. This is reflective of the formation of a passive layer. The kinetics of the corrosion in Gas 5 (catalyzed) are in between linear and parabolic behavior, with n = 0.8. The weight gained in Gas 5 (catalyzed) after 100 hours was as high as that gained in the sulfidizing gases. However, the scale thickness of the scale

formed in Gas 5 is less than the scale thickness of the sulfides. This implies that the phases formed from exposure to Gas 5 have a higher density than iron sulfide.

The platinum wire catalyst used to force the reaction of O_2 and SO_2 to form SO_3 has a large effect on the corrosion of Fe-10wt%Al. In Gas 5 without the catalyst, the microstructure of the scale formed on the alloy is very similar to that formed in Gas 4. This would imply that in the Fe-S-O phase stability diagram (Figure 4.1), Gas 5 without the catalyst would lie in the same phase field as Gas 4. In these gases, iron oxides form on the scale. However, SO_3 gas reacts readily with iron oxide to form iron sulfate. Therefore, the higher weight gain observed for Fe-10wt%Al in Gas 5 (catalyzed) would be attributed to the formation of a sulfate in the scale.[3]

4.3 Summary

A comparison of the scale thicknesses of each alloy in each gas composition is seen Figure 4.47. T11 seems to form relatively thick scales in all of the gases tested, although the scales formed in the oxidizing gases were thinner than those formed in the sulfidizing gases. The nickel-base alloys exhibit thick scale formation in the sulfidizing gases, but very thin, almost non-existent scales in the oxidizing environments. 309SS follows a similar trend in the oxidizing environments. Both FM72 and 309SS have thinner scales than the Inconel alloys in the sulfidizing gases. The iron aluminide performs very well in the highly sulfidizing gas, forming a very thin scale in Gas 1; however, it forms a relatively thick scale in the higher oxidizing environment of Gases 4 and 5 (catalyzed). In Gas 5 (non-catalyzed), the scale formed after 100 hours was thin

and non-continuous. The parabolic kinetics indicate the formation of a passive layer in this environment.

Figure 4.48 compares the n-values obtained for each alloy in each gas composition. Even though the Inconel alloys possessed very thick scales in the sulfidizing atmospheres, they all followed parabolic kinetics. However, 309 stainless steel exhibits kinetics which are close to linear in the sulfidizing gases. T11 experiences almost linear kinetics in Gas 1, but more parabolic kinetics in Gases 2-5. The iron aluminide displays linear behavior in all of the gas compositions except Gas 1 and Gas 5 (non-catalyzed). It is important to note that the n-values of the corrosion rates do not directly relate to the thickness of the scales formed after 100 hours. The n-values give an average for all of the layers formed and are not indicative of the scale thickness or weight gain.

A plot of the weight gain vs. the scale thickness for all of the alloys in all of the gas compositions is shown in Figure 4.49. A general relationship between the scale thickness and the weight gain can be made mathematically. This is seen in Figure 4.48. A best fit line of $y = 0.0602x^{1.1982}$ describes an almost linear relationship. However, it must be noted that the different phases formed possess different densities. For example, in Figure 32, IN622 in Gas 3 exhibits a higher weight gain than T11 in Gas 1, however, T11 possesses a scale 10 μm thicker than the Inconel alloy. The reason for this discrepancy is due to the fact that nickel is heavier element than iron; therefore, the nickel-bearing phases formed in the corrosion scale would have a higher mass than the

iron sulfides formed on T11. Table 4.7 summarizes corrosion kinetics and scale thickness of each alloy exposed to each gas composition.

A schematic of each of the microstructures is shown in Figures 4.50. The sulfidation of the nickel base alloys involves the formation of an outer Ni3S2 layer and an inner mixture of various sulfides. The corrosion scale formed on 309SS during sulfidation consists of an outer $Fe_{1-x}S$ layer and an inner, more compact $FeCr_2S_4$ layer. $Fe_{1-x}S$ is the main constituent formed during the sulfidation of T11. Fe-10wt%Al also forms an outer $Fe_{1-x}S$ layer under sulfidizing conditions. The inner layer consists of $FeAl_2S_4$. However, under extremely sulfidizing conditions, a protective oxide layer forms on Fe-10wt%Al

Under oxidizing conditions, both the nickel-base alloys and the stainless steel form a protective oxide layer on the surface (Figure 4.53). In Gas 4, iron oxide layers form on T11. A mixture of iron and aluminum oxides form on Fe-10wt%Al under oxidizing conditions.

4.4 Cyclic Gas Experiments

Light Optical photomacrographs of the alloys after 96 hours exposure of 12 hour cycles between Gases 5 (catalyzed) and 3 at 500°C are shown in Figure 4.51. Because the start-up gas atmosphere in a boiler is oxidizing, the alloys were exposed to a Gas 5 (catalyzed) cycle first. The scales formed on the surface of IN622 and IN625 were very thin and yellow in color. In contrast, FM72 possessed a thin, dark colored scale. Differences in alloying compositions may explain the differences in surface scales

formed between FM72 and the Inconel alloys. A thin, gray colored scale formed on 309SS. Both T11 and Fe-10wt%Al formed thicker scales than the other alloys.

4.4.1. Microstructures and Kinetics

4.4.1.1. Nickel-base alloys

Cross sections of the scale microstructures of the nickel-base alloys are shown in Figures 52-53. The scales formed on IN622 and IN625 appear to have two thin layers - an outer, sulfide layer and an inner layer that attacks the metal at the dendrites. The scale thicknesses of IN622 and IN625 are 3.85μm and 2.13μm respectively. The scale formed on FM72 is thicker than the Inconel alloys. The scale-metal interface is scalloped in shape, which indicates some attack of the substrate. The average thickness is 17.5μm. Several layers appear to have formed in the FM72 scale, Figure 53. XRD detected the presence of Ni_3S_2 in the scale (Figure 4.54). An extraneous peak pointed to the possibility of Cr_2O_3 in the scale, shown in Table 4.9. Therefore, it is possible that the layers are alternating oxides and sulfide because of the alternating gas compositions.

Plots comparing the weight gain vs. time in Gas 3, Gas 5 (catalyzed), and the cyclic atmosphere for IN622, IN625, and FM72 are shown in Figures 4.55-4.57. All of the alloys experienced much lower corrosion rates in the cyclic atmosphere compared to exposure to Gas 3. However, corrosion in the cyclic atmosphere was slightly higher than in Gas 5 (catalyzed). However, it appears that exposure to Gas 5 (catalyzed) during the gas cycles attributes to the lower corrosion rates observed.

4.4.1.2. Fe-Cr alloy

A cross section of the corrosion scale formed on 309SS is seen in Figure 4.58. A layered structure similar to that seen on FM72 is apparent. The scale thickness is 6.1μm, which is thicker than the Inconel alloys, but thinner than FM72. X-ray diffraction detected Fe1-xS and $FeCr_2S_3$ in the corrosion scale (Figure 4.59). However, a peak at 2θ = 50.7 implies the existence of Cr_2O_3 in the scale, as seen in Table 4.10. Therefore, it appears that the specimen underwent both oxidation and sulfidation under these conditions.

Figure 4.60 compares the weight gain vs. time for 309SS exposed to Gas 3, Gas 5 (catalyzed) and cyclic atmosphere. Much lower weight gains are observed in the cyclic atmosphere compared to Gas 3. The weight gain from exposure to the cyclic atmosphere is slightly larger than that seen in Gas 5 (catalyzed). Therefore, exposure to an oxidizing atmosphere may be the source of the low weight gain observed.

4.4.1.3. Fe-base alloy

A layered structure also appears in the corrosion scale formed on T11, as seen in Figure 4.61. X-ray diffraction (Figure 4.62) indicates the formation of $Fe_{1-x}S$ in the scale. The extraneous peaks indicate the additional existence of iron oxide or iron sulfate (Table 4.11). EDS (Figures 4.63 and 4.64) performed on the scale showed the presence of iron, chromium, sulfur, and oxygen in the scale adjacent to the base metal. Iron, sulfur, and oxygen were the only elements that were detected in areas near the scale/gas interface. Therefore, the scale most likely formed by the outward diffusion of iron ions and their reaction with the oxidizing and sulfidizing gases.

Figure 4.65 compares the weight gain vs. time for the corrosion of T11 in Gas 3, Gas 5 (catalyzed), and cyclic atmosphere. Higher weight gains are observed for exposure to the cyclic atmosphere compared to Gas 3. However, exposure to Gas 5 (catalyzed) resulted in a higher weight gain than exposure to the cyclic atmosphere. The thickness of the scale formed in the cyclic atmosphere measured 27μm, which is thinner than the scales formed in Gas 3 and Gas 5.

4.4.1.4. Fe-10wt%Al

A cross section of the scale microstructure of Fe-10wt%Al exposed to the cyclic oxidizing and sulfidizing atmospheres is shown in Figure 4.66. The scale thickness is much larger than the scales formed in Gases 3 and 5 (catalyzed). Three main corrosion layers are apparent in the scale – an outer, porous layer, an intermediate gray layer, and an inner two-phase layer. X-ray diffraction (Figure 4.67) detected the presence of both oxides and sulfides in the scale. Table 4.12 lists the possible phases that match with the XRD spectrum.

Figure 4.68 compares the weight gain vs. time for Fe-10wt%Al exposed to Gas 3, Gas 5 (catalyzed) and the cyclic atmosphere. A larger weight gain over time is apparent for the alloy exposed to the cyclic atmosphere. This high weight gain is reflective of the formation of non-protective scales in both Gas 3 and 5 (catalyzed)

Because the platinum wire catalyst in Gas 5 causes a significant change in the corrosion of T11 and Fe-10wt%Al, it should be noted that the corrosion in cycling atmospheres may change without the use of the catalyst. The kinetics and microstructure of Fe-10wt%Al exposed to Gas 5 lacking the catalyst indicated the formation of a

passive layer. This type of corrosion scale formed may increase the corrosion resistance under cyclic atmospheres.

4.5 Summary

Figure 4.69 compares the thickness of the corrosion scales for the alloys exposed to Gas 3, Gas 5 (catalyzed), and Gas 5 (catalyzed) - 3 cycle. The formation of very thin corrosion scales in the nickel-base alloys indicates an increase in corrosion resistance in the gas cycling environment. Because the thickness of the scales is much smaller than in the pure sulfidizing atmosphere, it can be determined that the lower weight gain/thinner corrosion scale can be attributed to alloys' exposure to the oxidizing gas. 309SS also follows a similar behavior. Exposure of T11 in the cyclic atmosphere resulted in a lower scale thickness compared to constant exposures of Gases 3 and 5 (catalyzed). Therefore, T11 exhibits slightly better corrosion resistance in the cycling environment. Fe-10wt%Al suffered an increase in corrosion when exposed to the cycling environment because of the platinum catalysis of Gas 5. It is possible that because the alloy formed a passive layer in Gas 5 without the platinum catalyst, it may possess better corrosion resistance in cyclic atmospheres without a catalyzed gas.

5.0 Conclusions

1. The nickel-base alloys displayed parabolic corrosion kinetics in the sulfidizing atmospheres, which indicates diffusion-controlled corrosion. They also exhibited very good corrosion resistance the in the oxidizing atmospheres due to the formation of a protective oxide layer.

2. The stainless steel possessed lower weight gains and scale thickness in the sulfidizing atmospheres compared to the nickel-base alloys. The formation of the compact spinel phase ($FeCr_2S_4$) is attributed to the lower weight gains. It also displayed very good corrosion resistance in the oxidizing environments because of the formation of a protective Cr_2O_3 layer.

3. Fe-10wt%Al exhibited excellent corrosion resistance in the most sulfidizing atmosphere due to the formation of a protective oxide layer. The use of a platinum wire catalyst increases the corrosion of the alloy due to the reaction between iron oxide and SO_3 to form a sulfate. Fe-10wt%Al experienced very low weight gains in the non-catalyzed gas, which reflects relatively good corrosion resistance in oxidizing environments.

4. The nickel-base alloys and the stainless steel exhibited very good corrosion resistance in the cycling environment. This is attributed to the cyclic exposure to Gas 5.

References

[1] Banovic, S.W., DuPont, J.N., and Marder, A.R., Mat. High Temp., Vol. 16, no. 4, 1999, pp. 195-200.

[2] Grabke, H.J. "Definition and Preparation of Gas Atmosphere" in Guidelines for Methods of Testing and Research in High Temperature Corrosion. Ed. Grabke and Meadowcroft, Institute of Materials, London, 1995, pp. 62-84.

[3] Epler, M. Unpublished Research, Lehigh University, 2000.

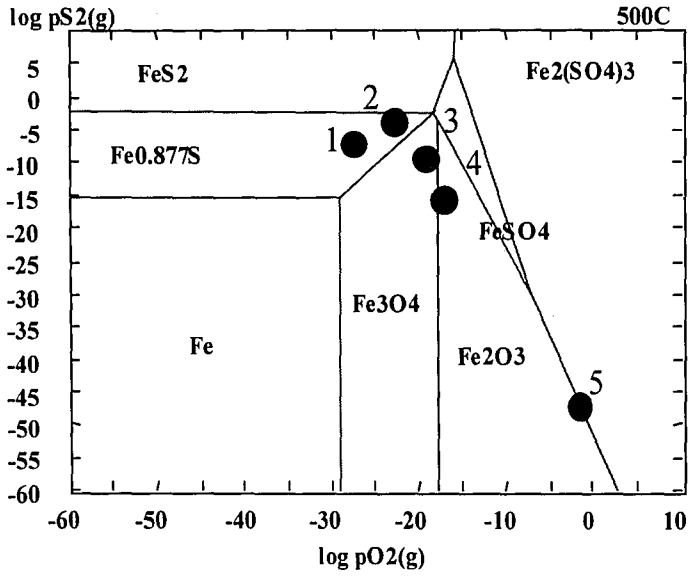

Figure 4. 1: Equilibrium phase stability diagram for Fe-S-O system.

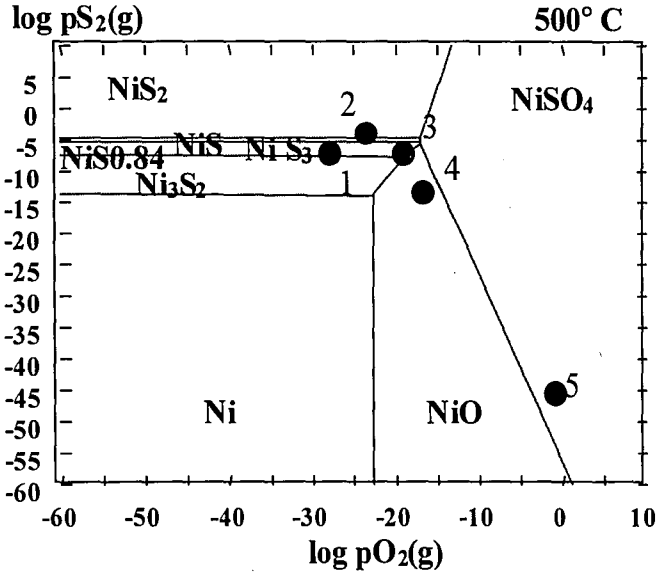

Figure 4. 2: Equilibrium phase stability diagram for Ni-S-O system.

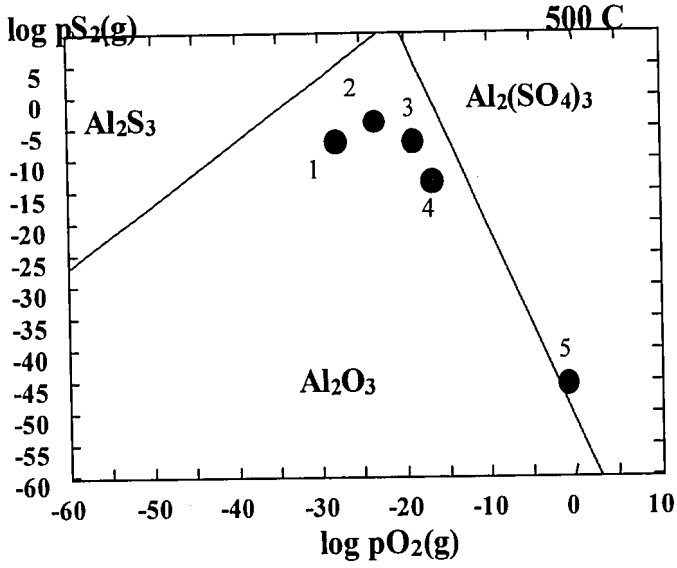

Figure 4. 3: Equilibrium phase stability diagram for Cr-S-O system.

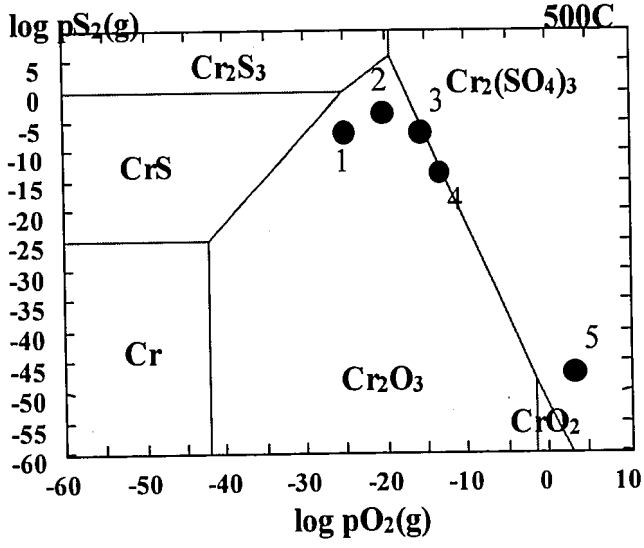

Figure 4. 4: Equilibrium phase stability diagram for Al-S-O system.

a) IN625 in Gases 1,2 and 3

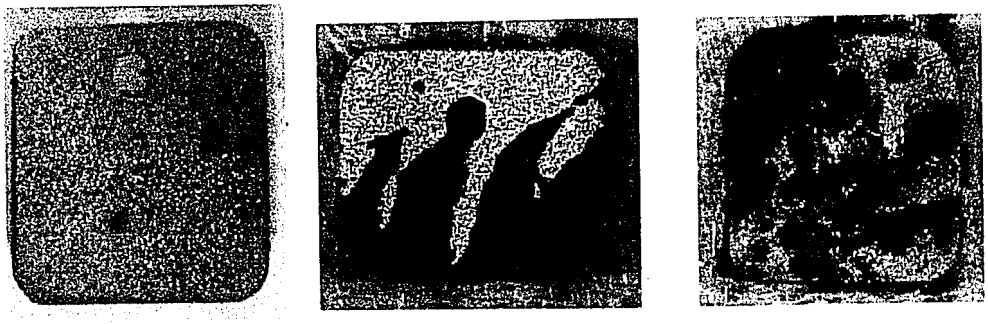

b) IN622 in Gases 1,2 and 3

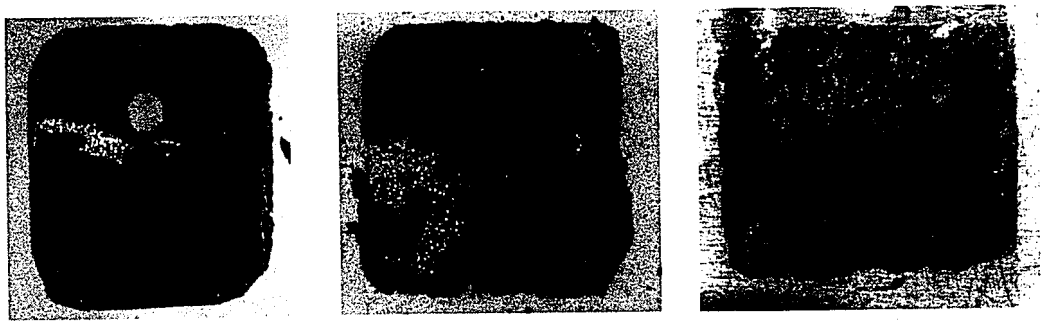

c) FM72 in Gases 1,2 and 3.

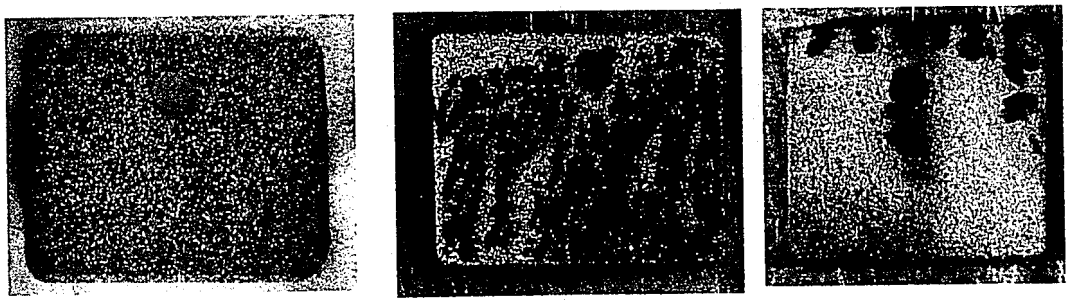

Figure 4. 5: Light optical photmacrographs of a) IN622, b)IN625 and c) FM72 after 100 hours exposure to Gases 1, 2 and 3 at 500°C.

a) IN625 in Gases 1,2 and 3

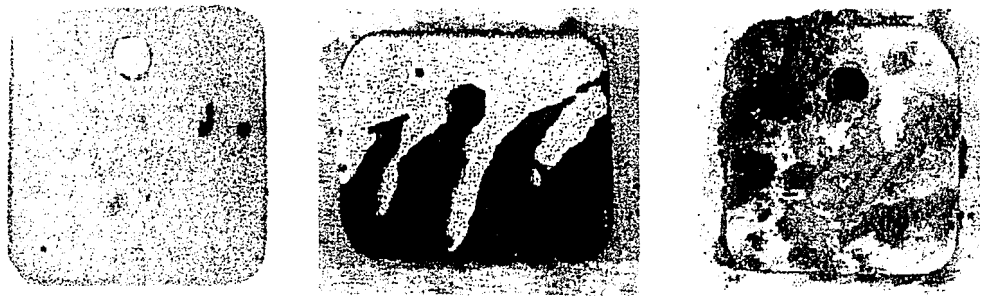

b) IN622 in Gases 1,2 and 3

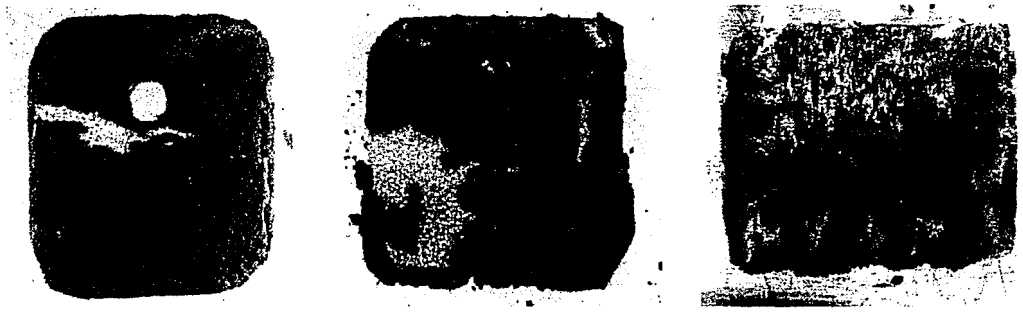

c) FM72 in Gases 1,2 and 3.

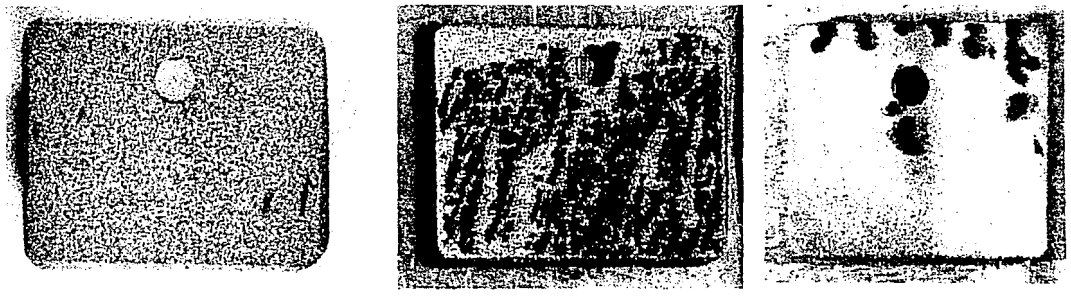

Figure 4. 5: Light optical photmacrographs of a) IN622, b)IN625 and c) FM72 after 100 hours exposure to Gases 1, 2 and 3 at 500°C.

a) T11 steel in Gases 1, 2, and 3

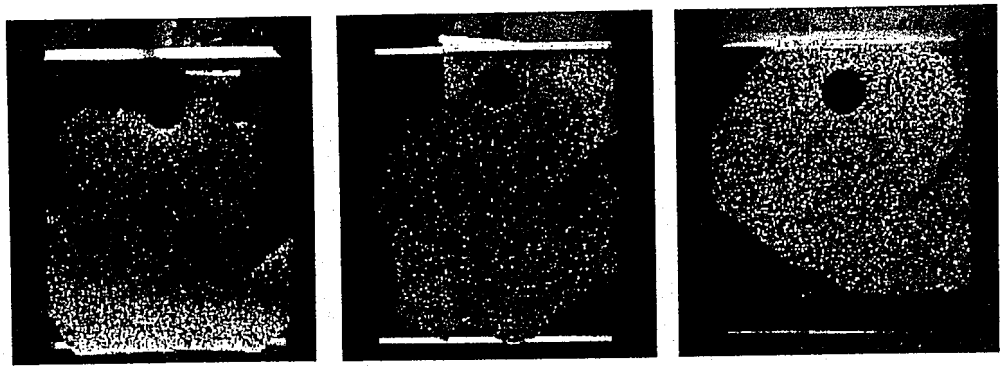

b) 309SS in Gases 1,2 and 3

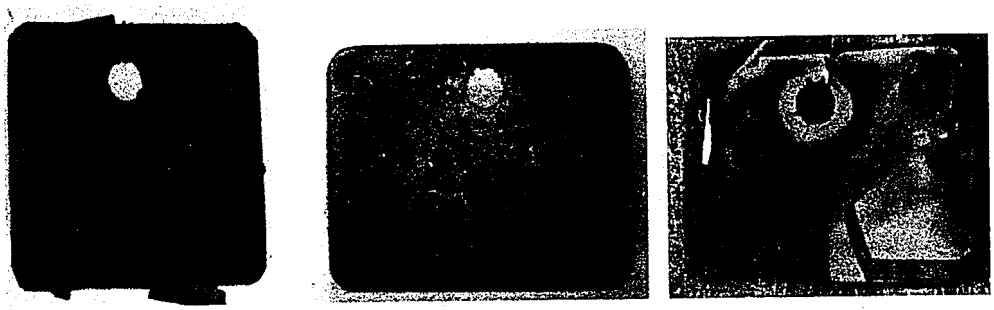

c) Fe-10w%Al in Gases 1, 2 , and 3

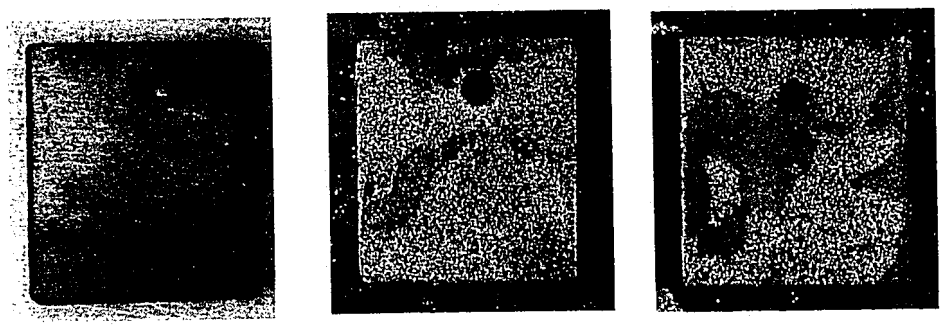

Figure 4. 6: Light optical macrographs of a) T11 steel, b) 309SS and c) Fe-10wt%Al after 100 hours exposure in Gases 1, 2 and 3 at 500°C.

a) T11 steel in Gases 1, 2, and 3

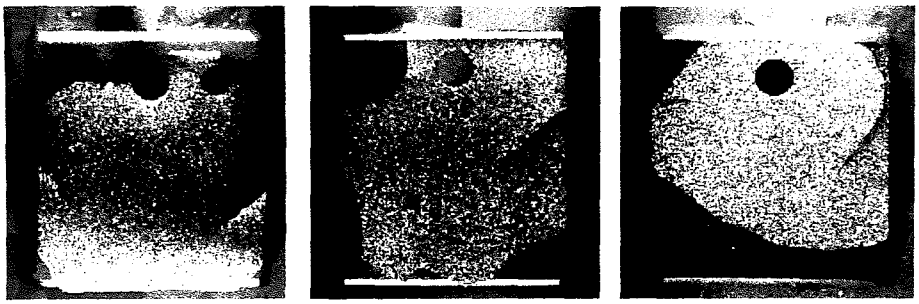

b) 309SS in Gases 1,2 and 3

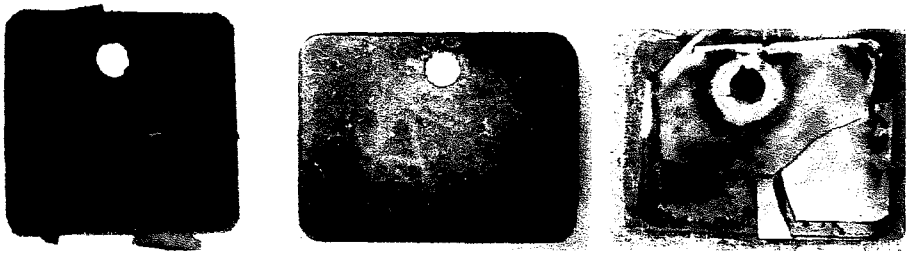

c) Fe-10w%Al in Gases 1, 2 , and 3

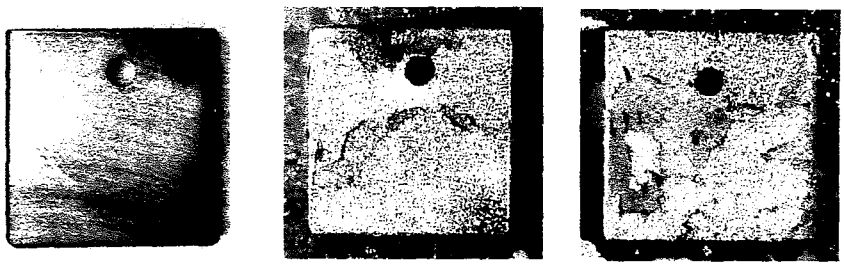

Figure 4. 6: Light optical macrographs of a) T11 steel, b) 309SS and c) Fe-10wt%Al after 100 hours exposure in Gases 1, 2 and 3 at 500°C.

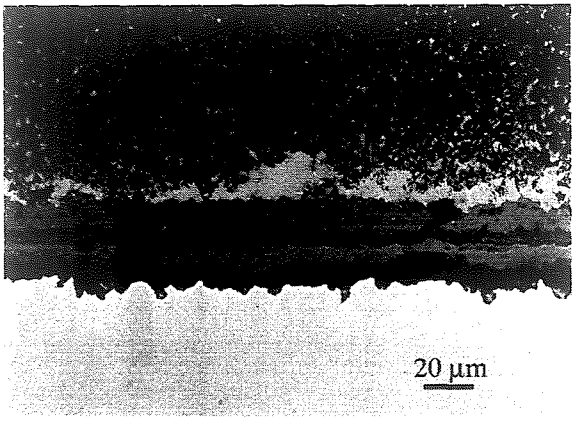

Figure 4. 7: Photomicrograph of the cross section of IN622 exposed to Gas 1 at 500°C for 100 hours.

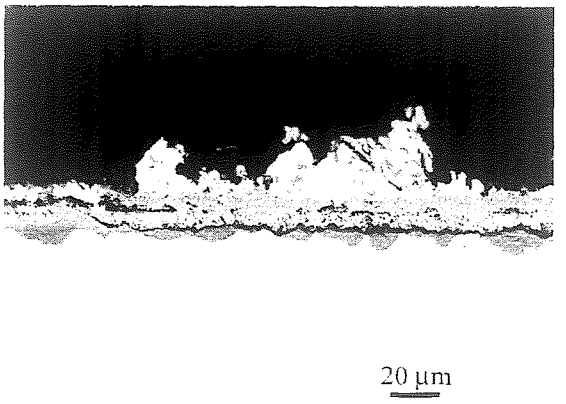

Figure 4. 8: Photomicrograph of the cross section of IN625 exposed to Gas 3 at 500°C for 100 hours.

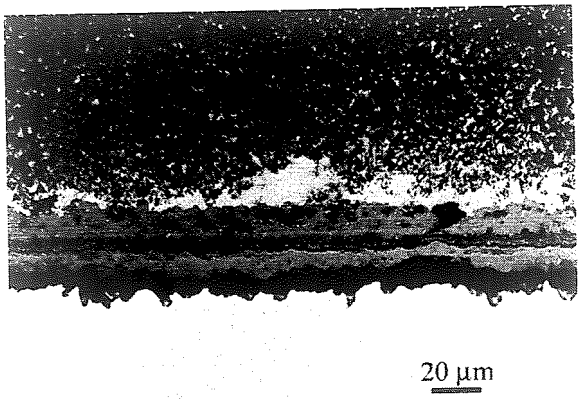

Figure 4. 7: Photomicrograph of the cross section of IN622 exposed to Gas 1 at 500°C for 100 hours.

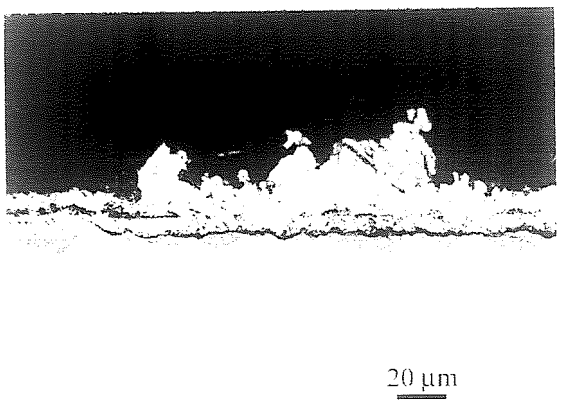

Figure 4. 8: Photomicrograph of the cross section of IN625 exposed to Gas 3 at 500°C for 100 hours.

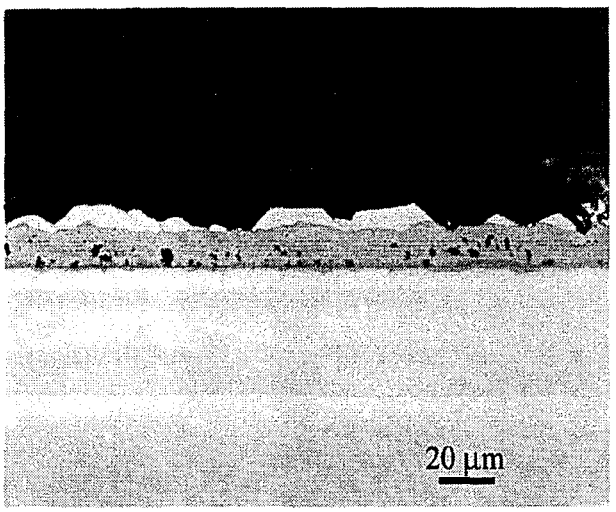

Figure 4. 9: Photomicrograph of the cross section of FM72 exposed to Gas 2 at 500°C for 100 hours.

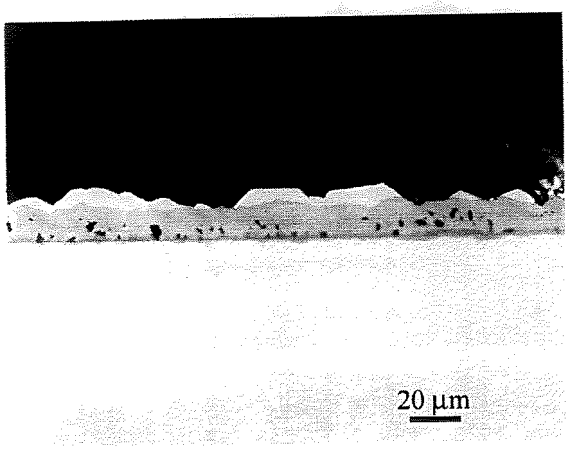

Figure 4. 9: Photomicrograph of the cross section of FM72 exposed to Gas 2 at 500°C for 100 hours.

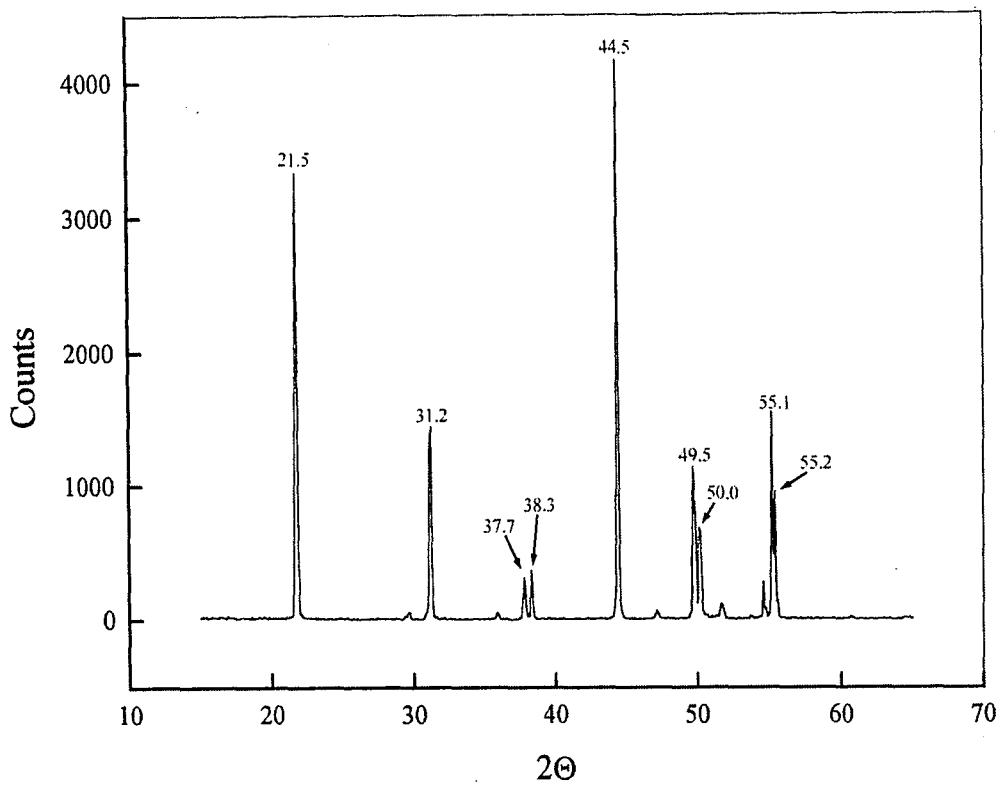

Figure 4. 10: X-ray diffraction spectrum obtained for IN625 exposed to Gas 2 performed with Cu Kα radiation. Peaks indicate presence of Ni_3S_2 in corrosion scale.

Table 4. 1: Powder diffraction table for Ni3S2 from JCPDS – International Centre for Diffraction Data

2 θ	Relative Intensity
21.75	67
31.10	100
37.78	33
38.27	11
44.33	31
49.73	43
50.12	39
54.62	13
55.16	45
55.30	38

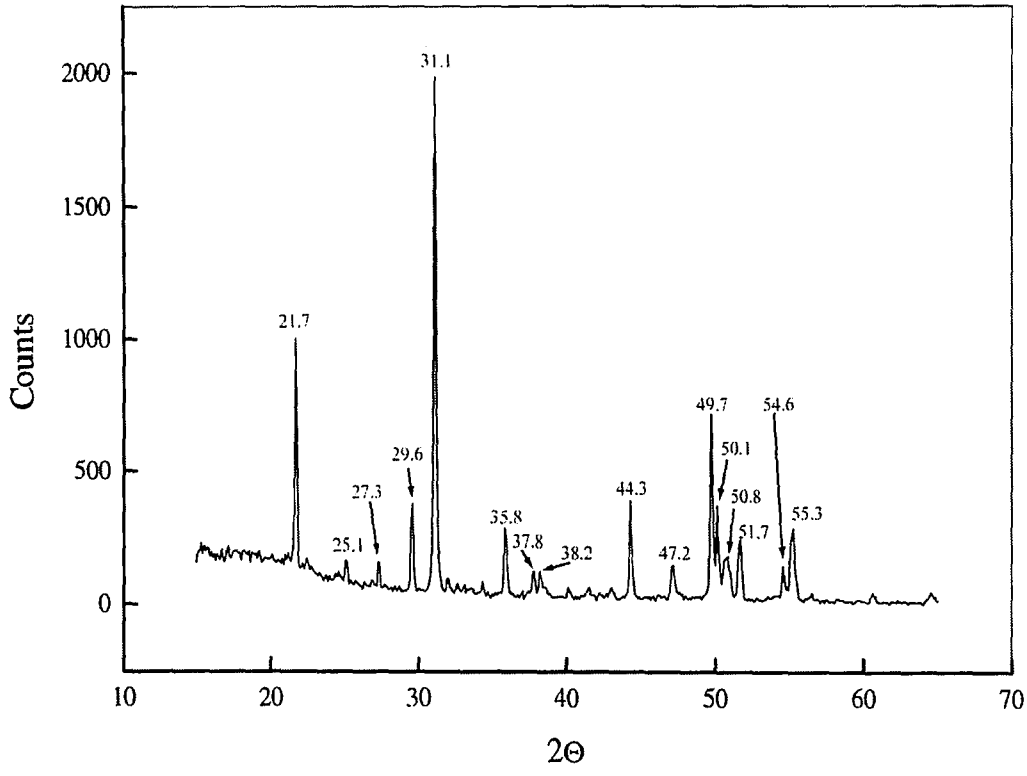

Figure 4. 11: X-ray spectrum for FM72 exposed to Gas 3 for 100 hours at 500°C performed with Cu Kα radiation.

Table 4. 2: List of possible phases that formed on FM72 exposed to Gas 3. Data obtained from JCPDS – International Centre for Diffraction Data.

FM72 Gas3	FeS	FeS2	NiS	Ni3S2	NiS2	NiO	Cr2O3	CrS	Cr2S3	Possible Compounds
21.7				21.755						Ni3S2
25.1										?
27.3					27.272				27.5	NiS2, Cr2S3
29.6	29.943							29.563		FeS, CrS
31.1				31.105	31.615					Ni3S2, NiS2
35.8	35.553		35.73		35.336					FeS, NiS, NiS2
37.8		37.07	37.38	37.78		37.25		37.733		FeS2, NiS, Ni3S2, NiO, CrS
38.2				38.272	38.815					Ni3S2, NiS2
44.3				44.331			44.194		44.594	Ni3S2, Cr2O3, Cr2S3
47.2	47.162	47.42								FeS, FeS2
49.7				49.734						Ni3S2
50.1			50.19	50.123			50.22			NiS, Ni3S2, Cr2O3
50.8										?
51.7										?
54.6				54.621			54.852			Ni3S2, Cr2O3
55.3				55.162						Ni3S2

a)

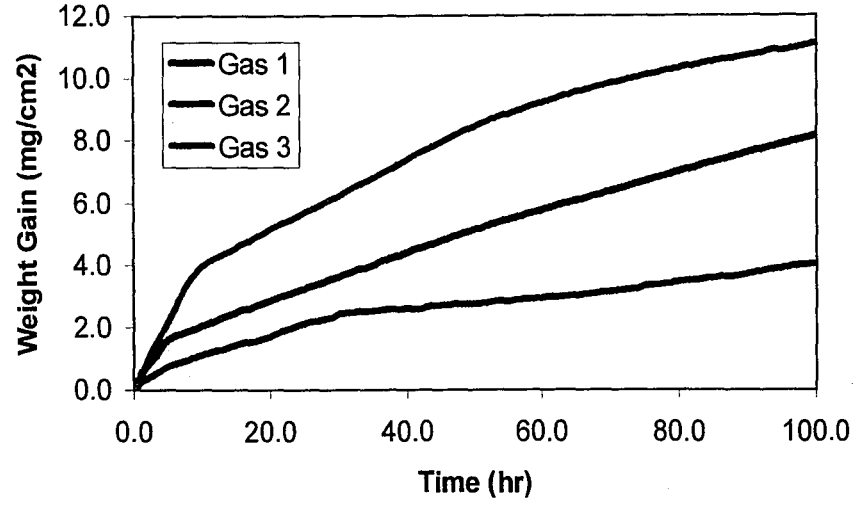

b)

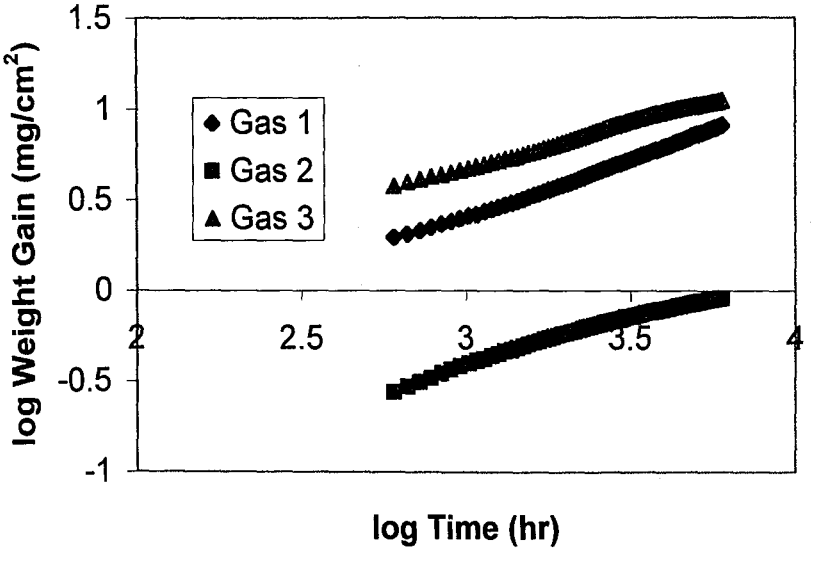

Figure 4. 12: Plot of weight gain vs. time for IN622: a) linear and b) logarithmic for exposure to Gases 1, 2, and 3 for 100 hours at 500°C.

a)

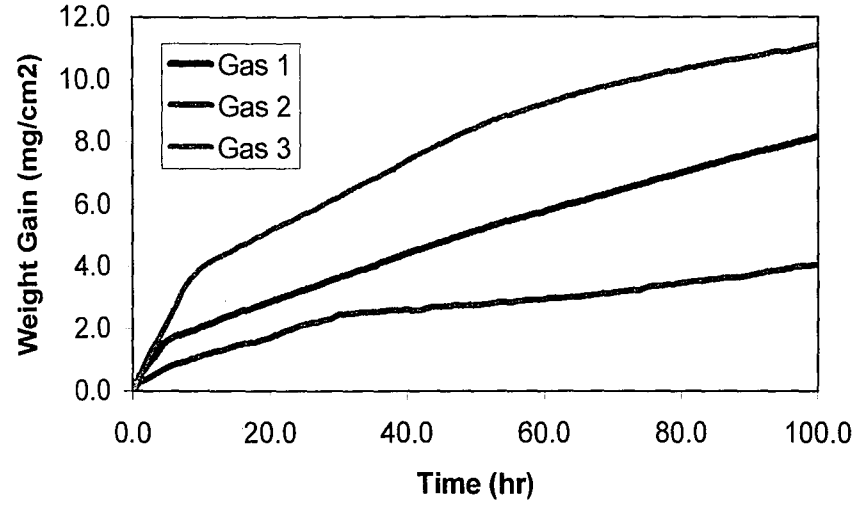

b)

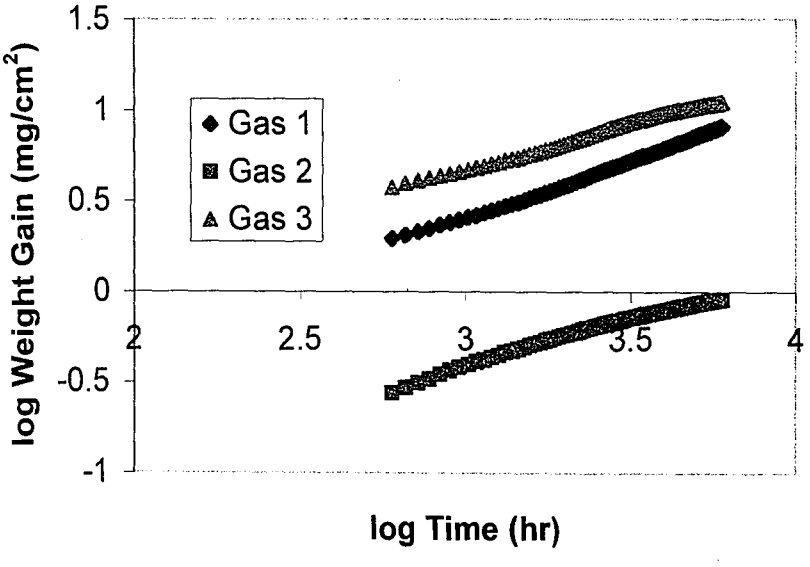

Figure 4. 12: Plot of weight gain vs. time for IN622: a) linear and b) logarithmic for exposure to Gases 1, 2, and 3 for 100 hours at 500°C.

a)

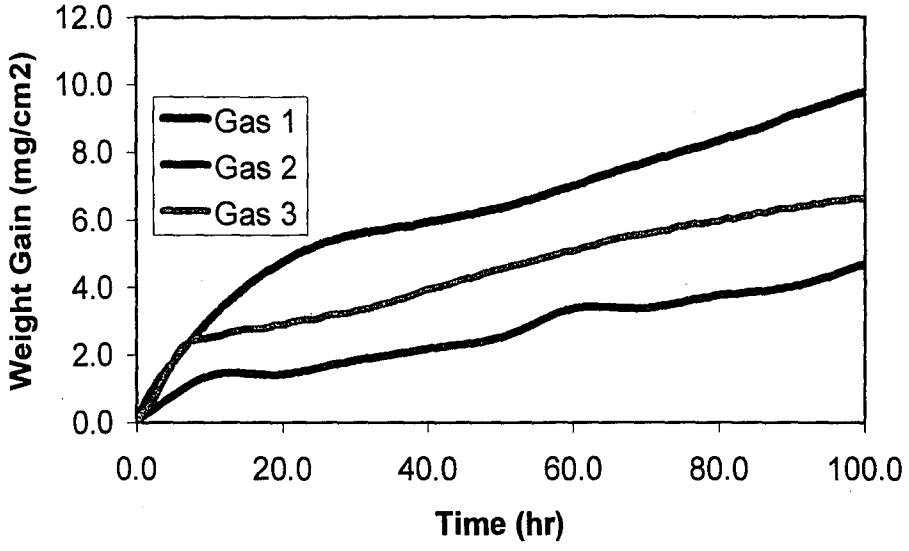

b)

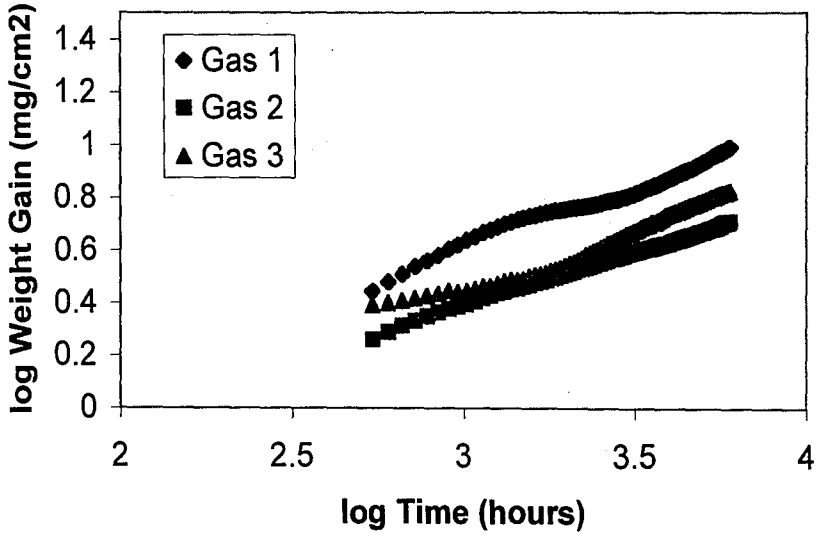

Figure 4. 13: Plot of weight gain vs. time for IN625: a) linear and b) logarithmic for exposure to Gases 1, 2, and 3 for 100 hours at 500°C.

a)

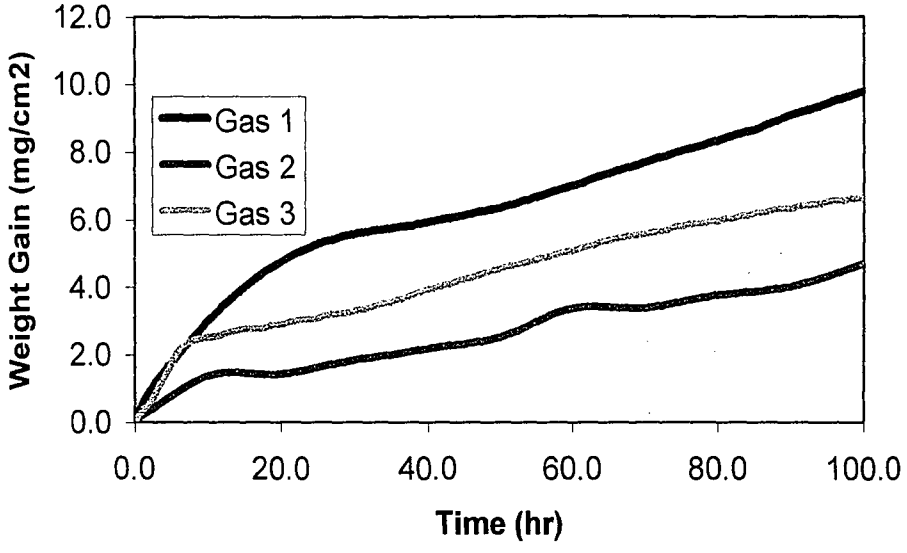

b)

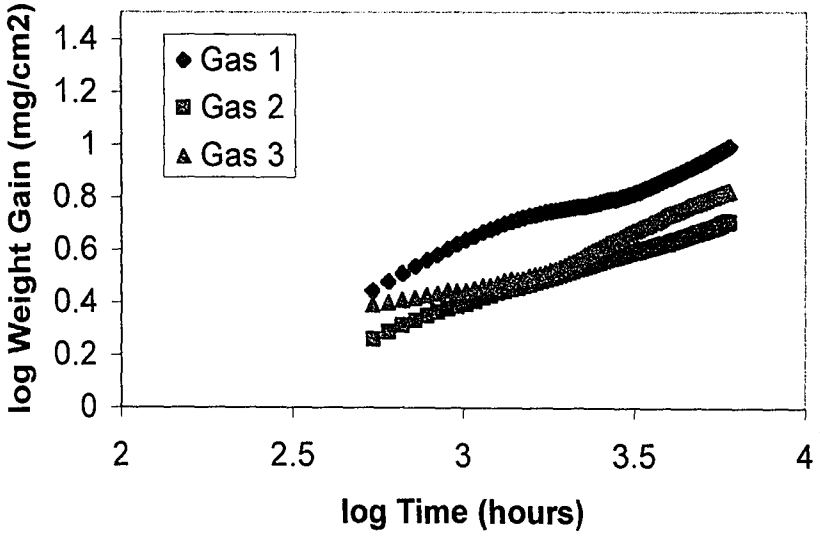

Figure 4. 13: Plot of weight gain vs. time for IN625: a) linear and b) logarithmic for exposure to Gases 1, 2, and 3 for 100 hours at 500°C.

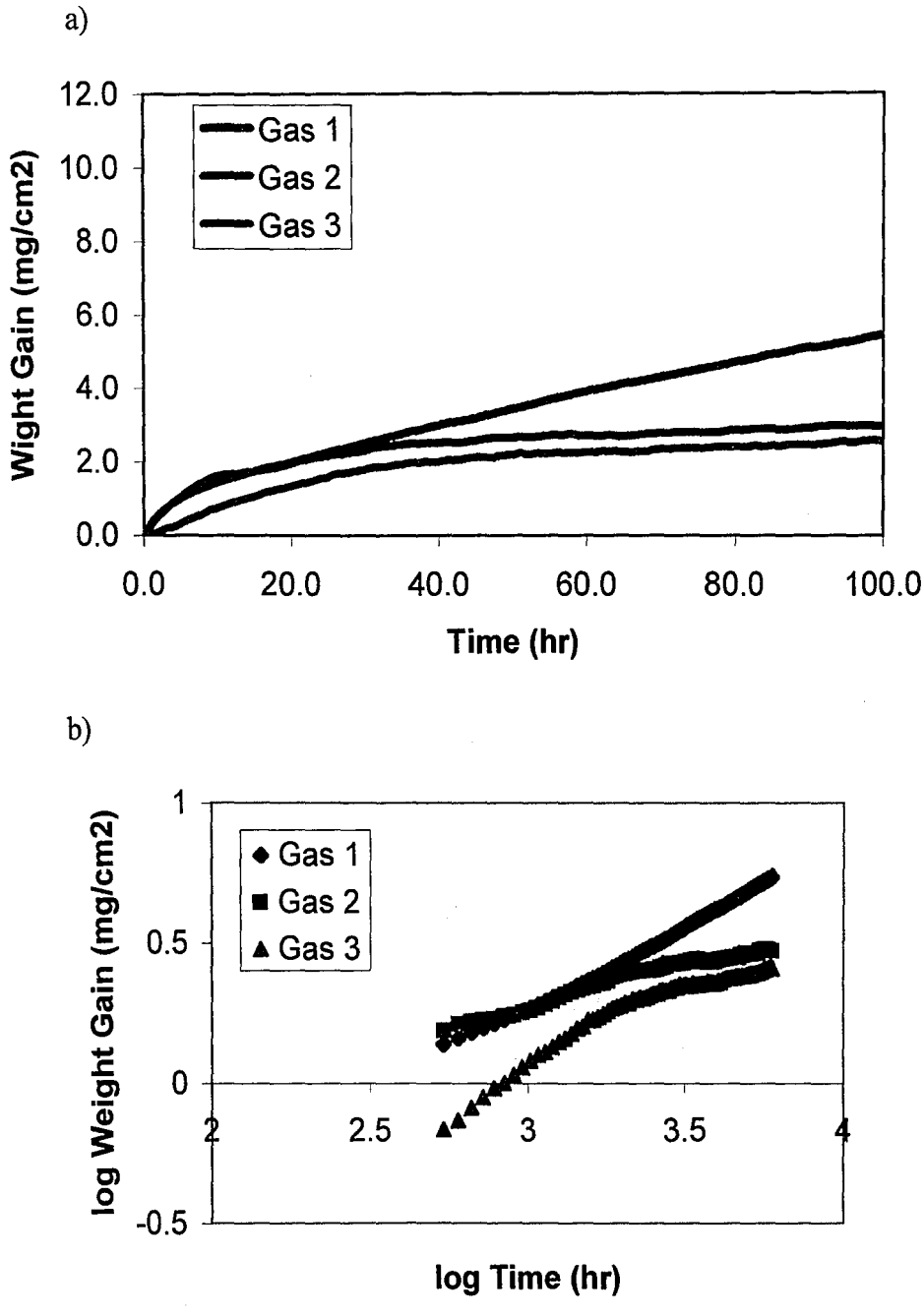

Figure 4. 14: Plot of weight gain vs. time for FM72: a) linear and b) logarithmic for exposure to Gases 1, 2, and 3 for 100 hours at 500°C.

a)

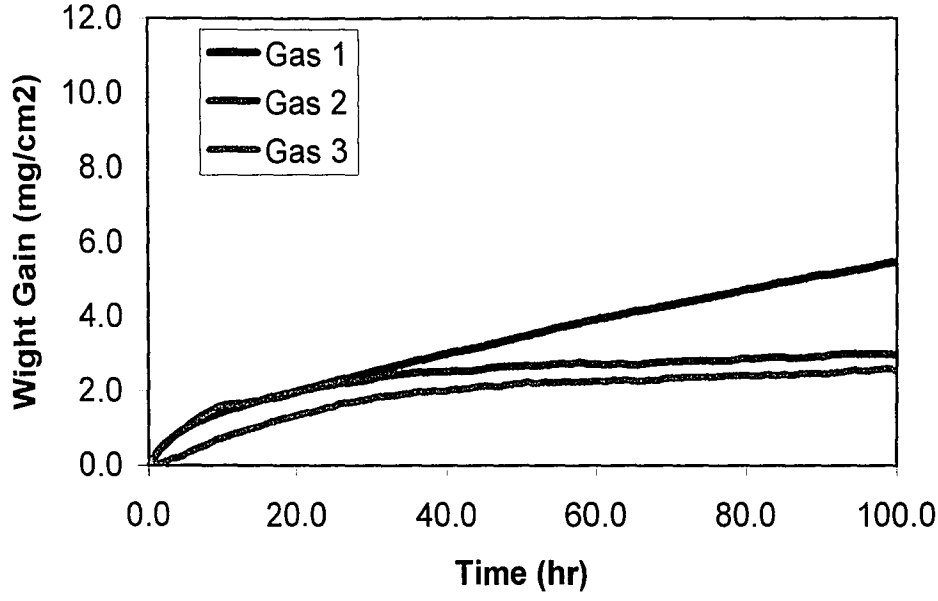

b)

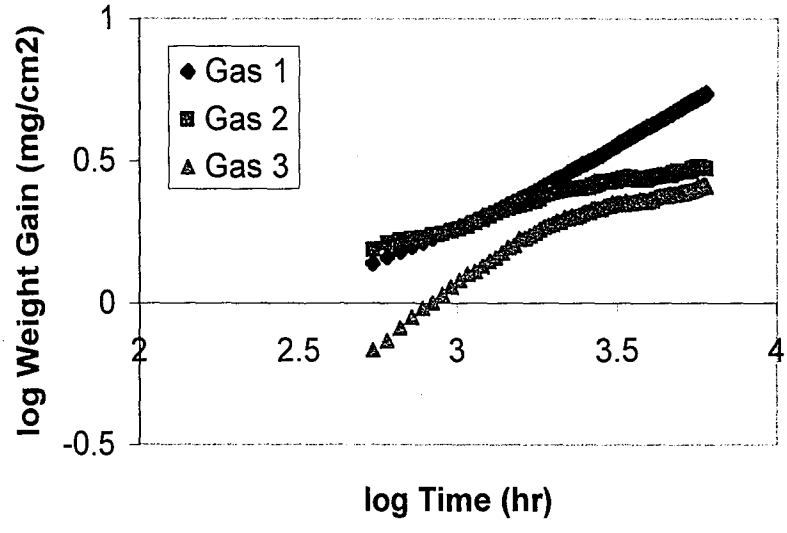

Figure 4. 14: Plot of weight gain vs. time for FM72: a) linear and b) logarithmic for exposure to Gases 1, 2, and 3 for 100 hours at 500°C.

a)

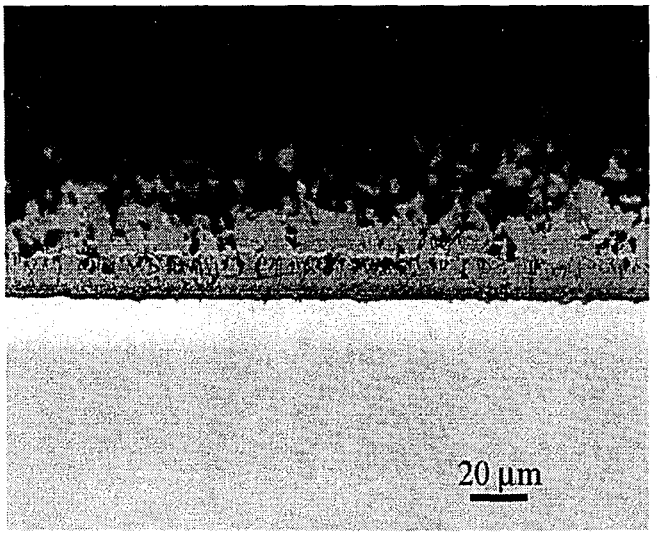

b)

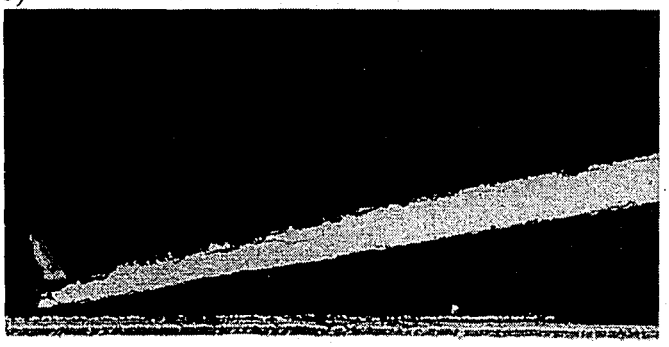

Figure 4. 15: Photomicrograph of the cross section of 309SS exposed to a)Gas 1 and b)Gas 3 at 500°C for 100 hours.

a)

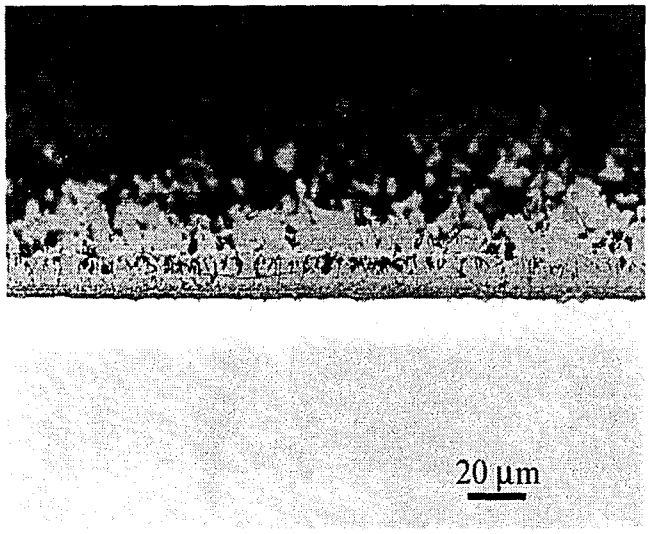

b)

Figure 4. 15: Photomicrograph of the cross section of 309SS exposed to a)Gas 1 and b)Gas 3 at 500°C for 100 hours.

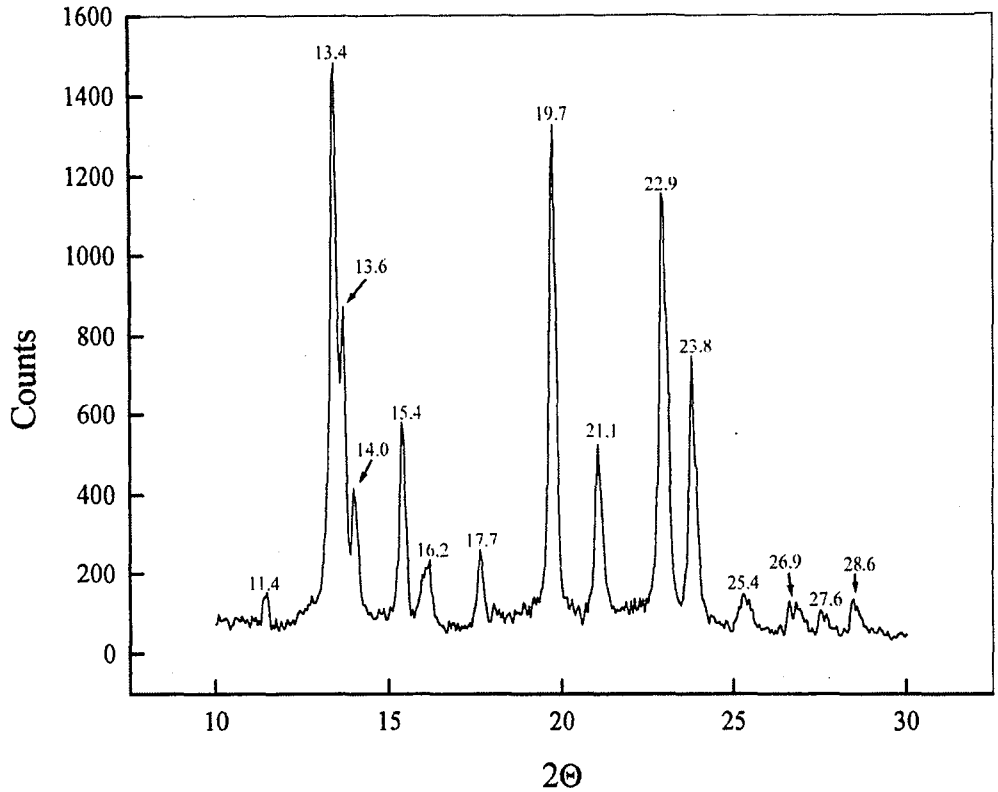

Figure 4. 16: X-ray diffraction spectrum obtained for 309SS exposed to Gas 1 performed with Mo Kα radiation. Peaks indicate presence of FeS and $FeCr_2S_4$ in corrosion scal

Table 4. 3: Powder diffraction table for FeS and $FeCr_2S_4$ from JCPDS – International Centre for Diffraction Data

FeS	FeCr2S4	Relative Intensity
13.77	13.67	
13.99		
	14.3	
15.48		
16.36		
	16.57	
	18.12	
19.87		
21.7	21.85	
	23.86	
24.46		
25.83		
	26.9	
	28.38	

a)

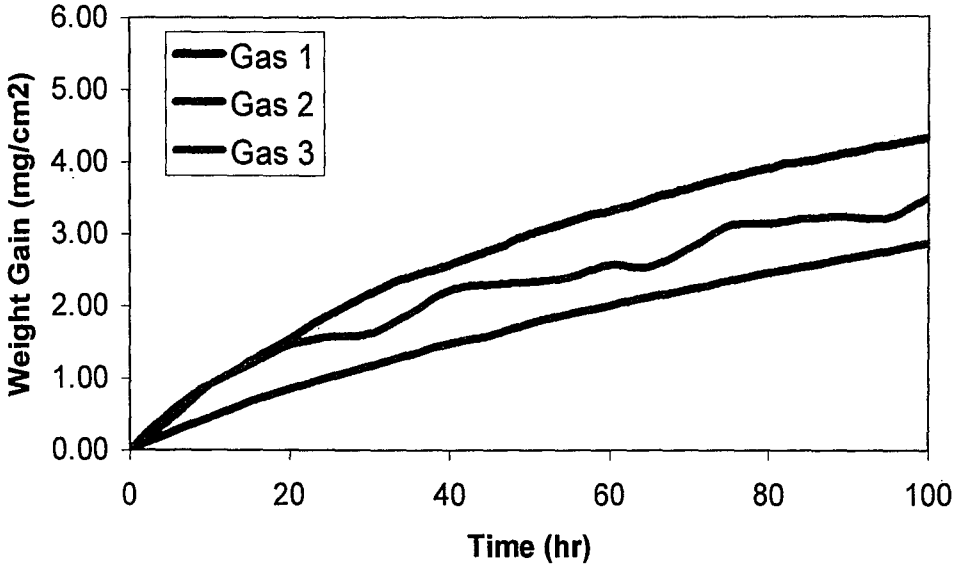

b)

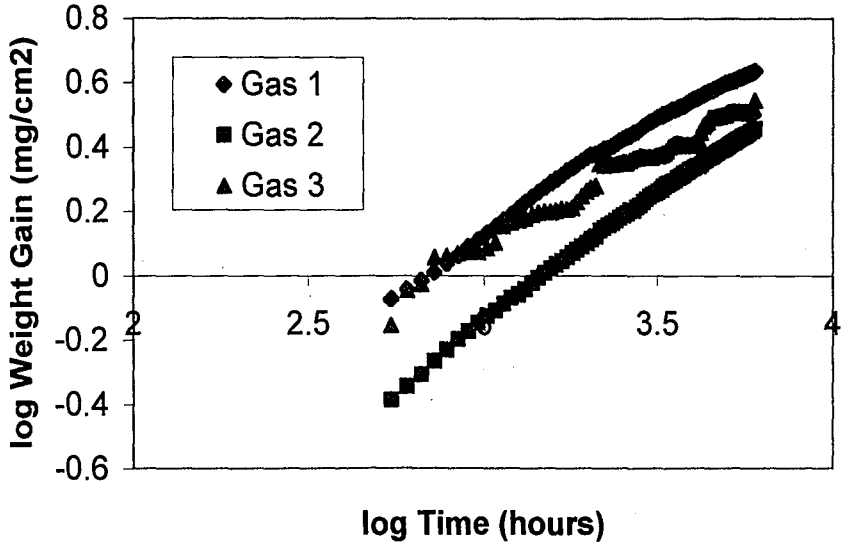

Figure 4. 17: Plot of weight gain vs. time for 309SS exposed to sulfidizing gases at 500°C for 100 hours: a) linear and b) logarithmic.

a)

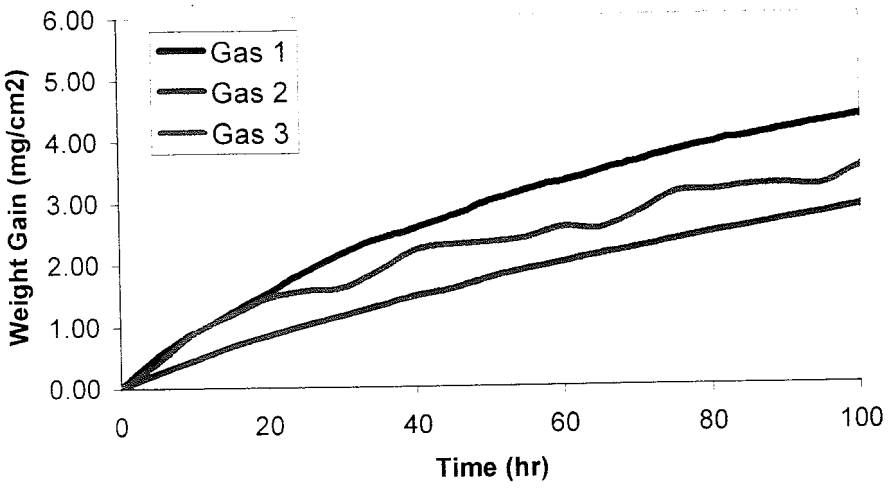

b)

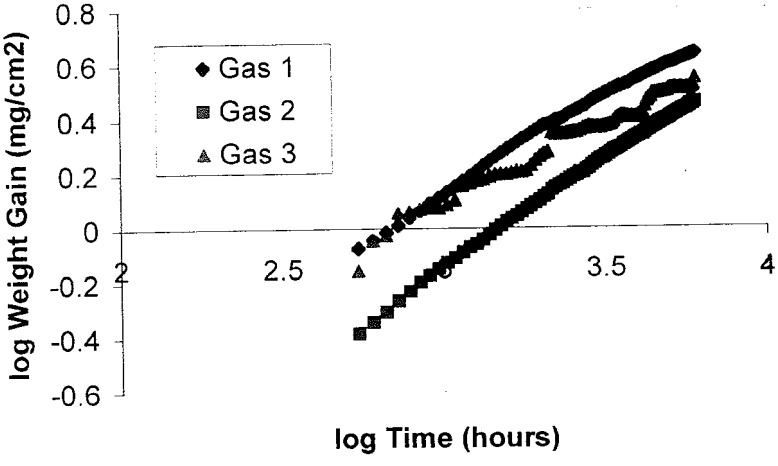

Figure 4. 17: Plot of weight gain vs. time for 309SS exposed to sulfidizing gases at 500°C for 100 hours: a) linear and b) logarithmic.

a)

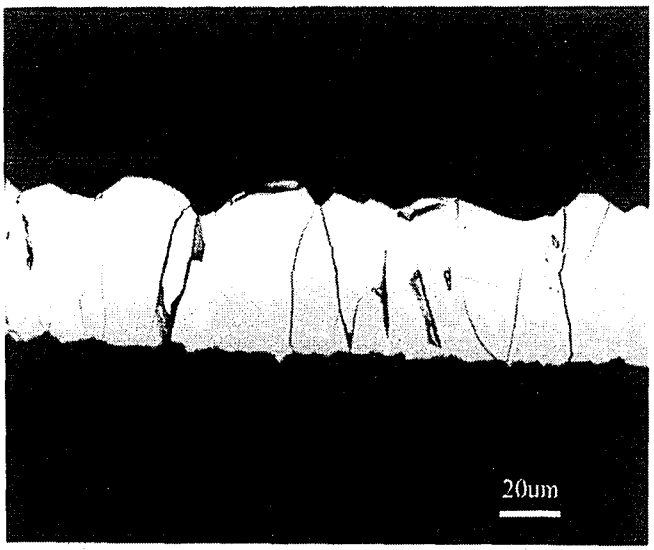

b)

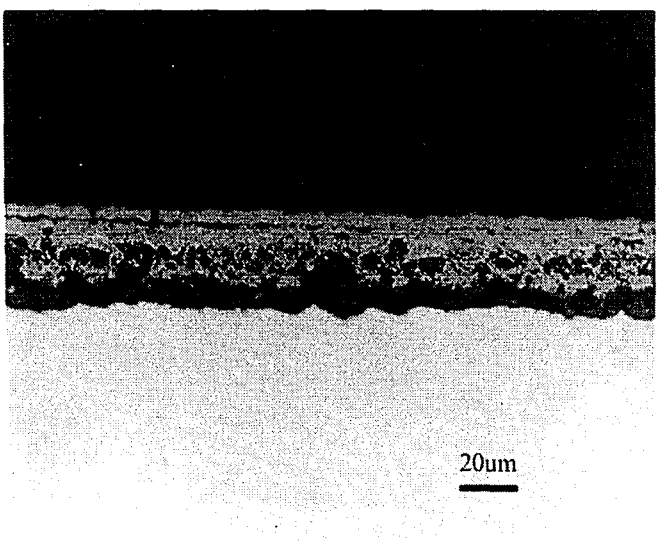

Figure 4. 18: Photomicrograph of the cross section of T11 exposed to Gas 1 at 500°C for 100 hours: a) $Fe_{1-x}S$ layer which spalled off of the substrate and b) Fe_{1-xS} layer enriched in Cr and Mo adjacent to substrate.

a)

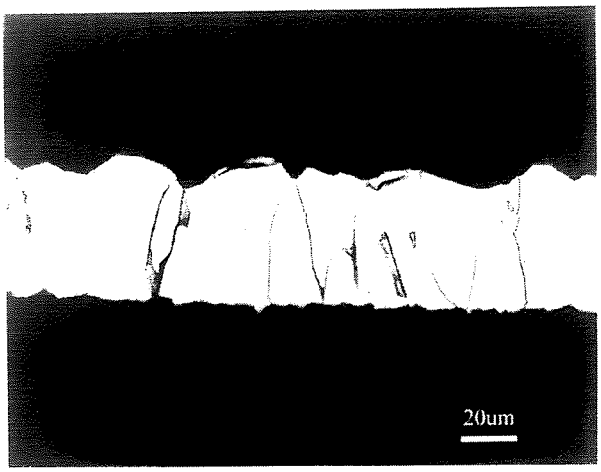

b)

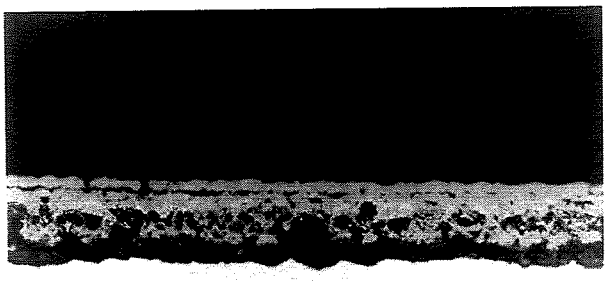

Figure 4. 18: Photomicrograph of the cross section of T11 exposed to Gas 1 at 500°C for 100 hours: a) $Fe_{1-x}S$ layer which spalled off of the substrate and b) Fe_{1-xS} layer enriched in Cr and Mo adjacent to substrate.

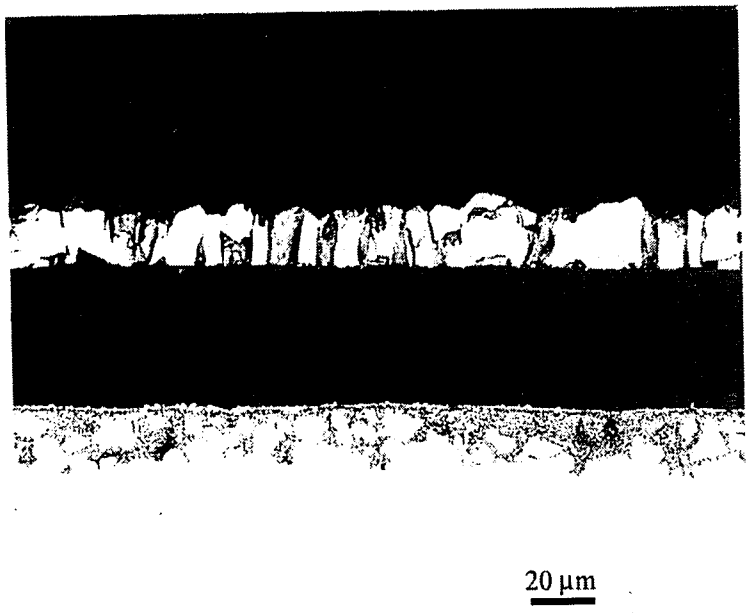

Figure 4. 19: Photomicrograph of the cross section of T11 exposed to Gas 3 at 500°C for 100 hours.

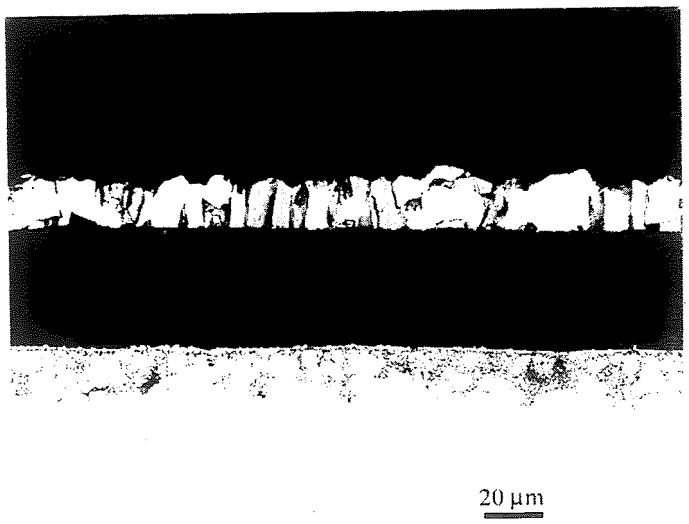

Figure 4. 19: Photomicrograph of the cross section of T11 exposed to Gas 3 at 500°C for 100 hours.

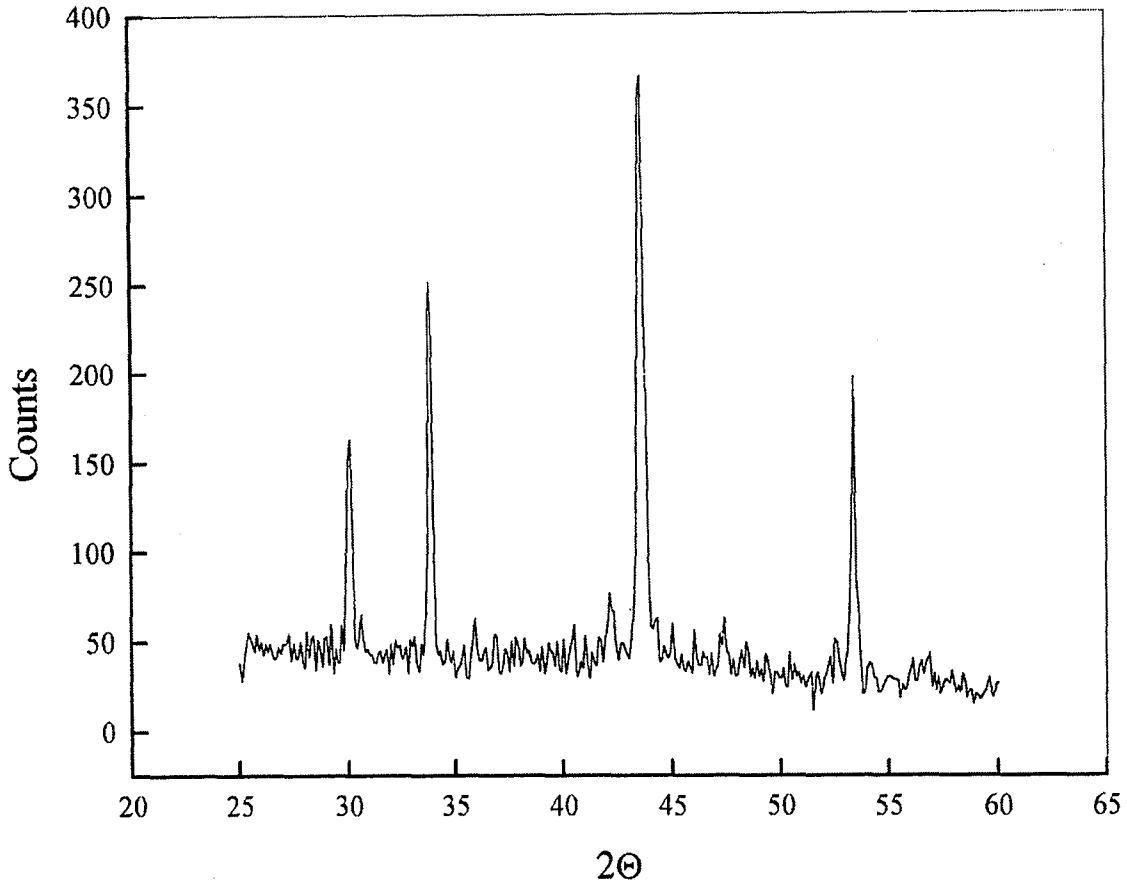

Figure 4. 20: X-ray diffraction spectrum obtained for outer scale formed on T11 steel exposed to Gas 1 performed with Cu Kα radiation. Peaks indicate formation of FeS scale.

Table 4. 4: Powder diffraction table for FeS from JCPDS – International Centre for Diffraction Data

2θ	Relative Intensity
29.62	466
33.45	439
42.58	33
43.18	999
52.55	335

a)

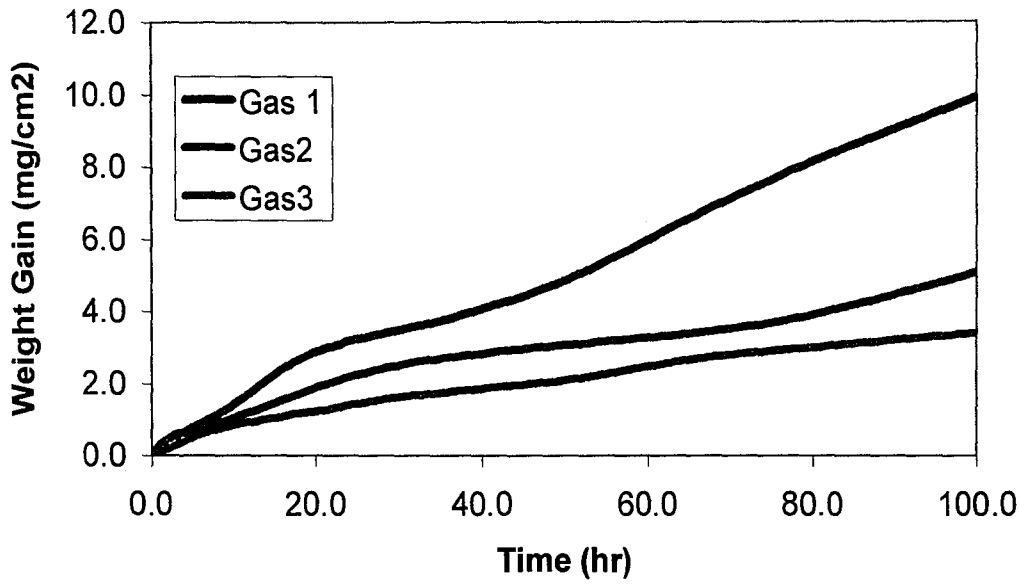

b)

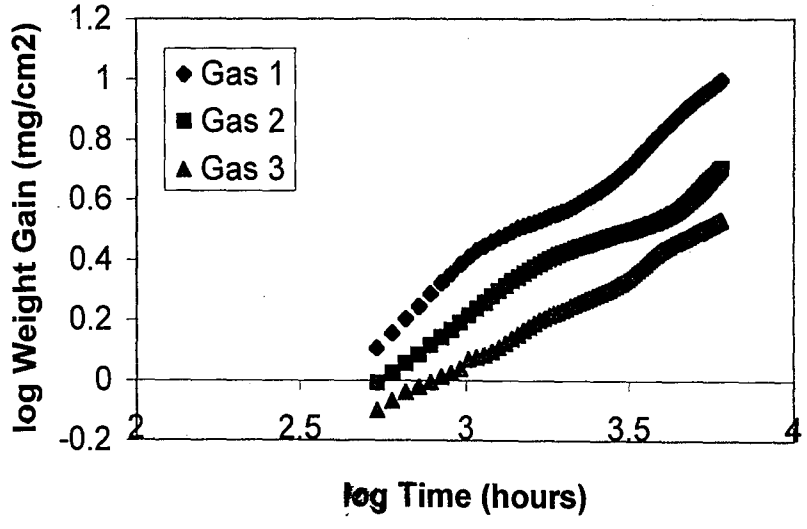

Figure 4. 21: Plot of weight gain vs. time for T11 exposed to the sulfidizing gases at 500°C for 100 hours: a) linear and b)logarithmic

a)

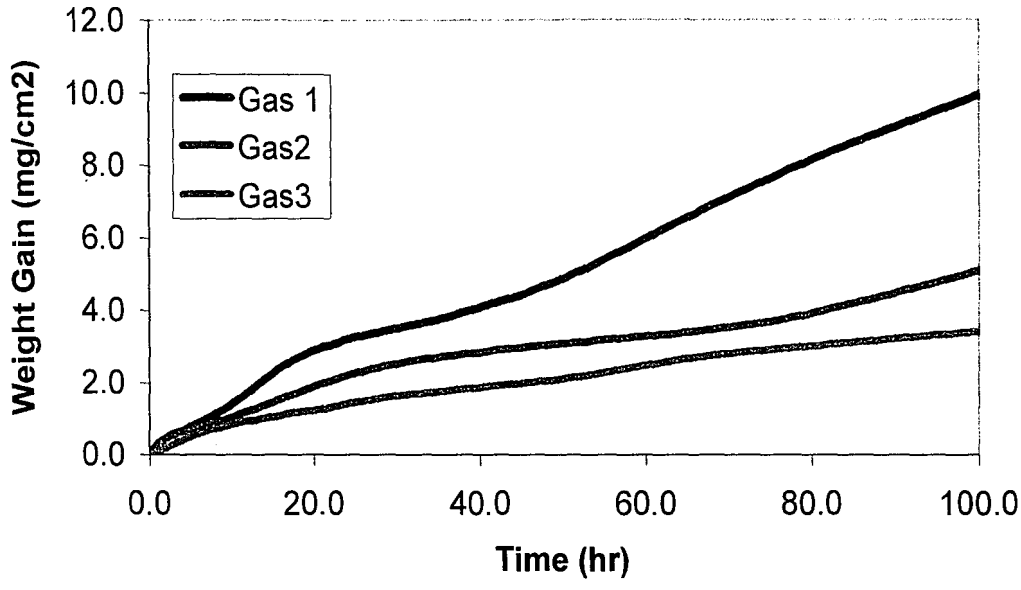

b)

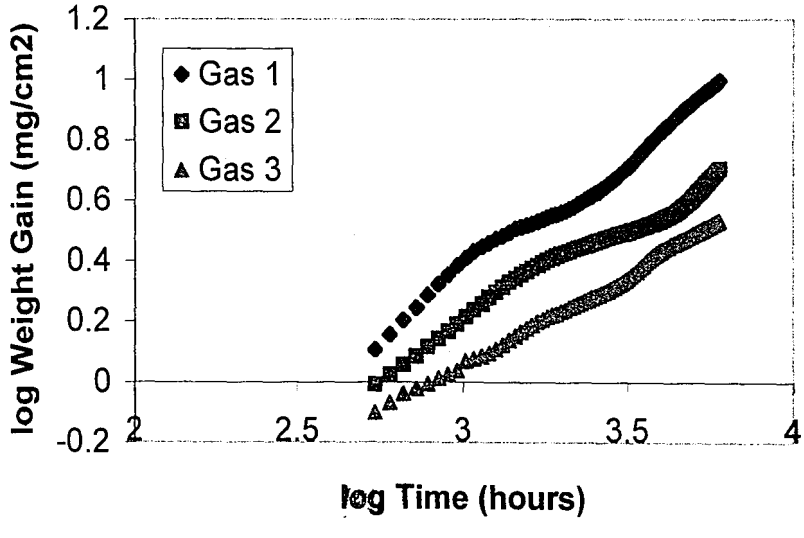

Figure 4. 21: Plot of weight gain vs. time for T11 exposed to the sulfidizing gases at 500°C for 100 hours: a) linear and b)logarithmic

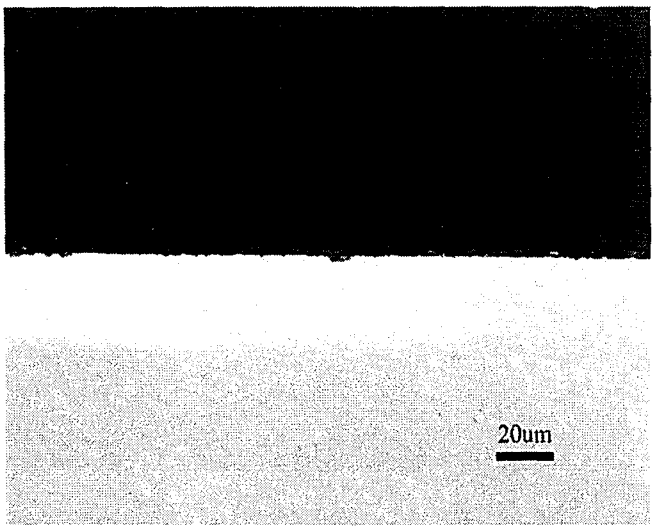

Figure 4. 22: Photomicrograph of the cross section of Fe-10wt%Al exposed to Gas 1 at 500°C for 100 hours.

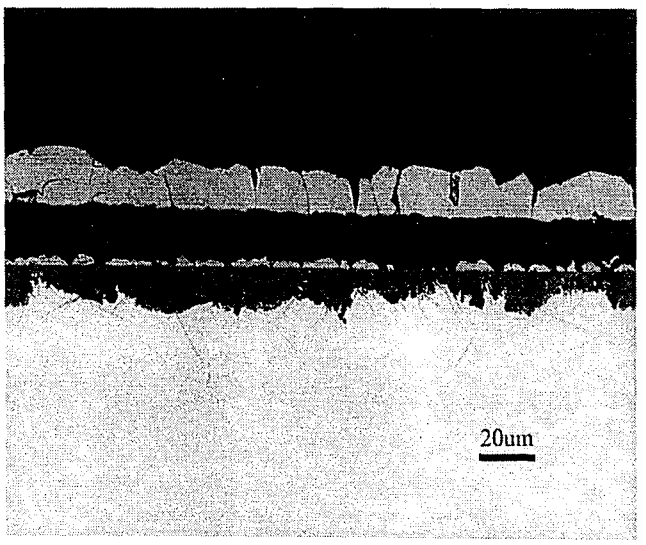

Figure 4. 23: Photomicrograph of the cross section of Fe-10wt%Al exposed to Gas 3 at 500°C for 100 hours.

Figure 4. 22: Photomicrograph of the cross section of Fe-10wt%Al exposed to Gas 1 at 500°C for 100 hours.

Figure 4. 23: Photomicrograph of the cross section of Fe-10wt%Al exposed to Gas 3 at 500°C for 100 hours.

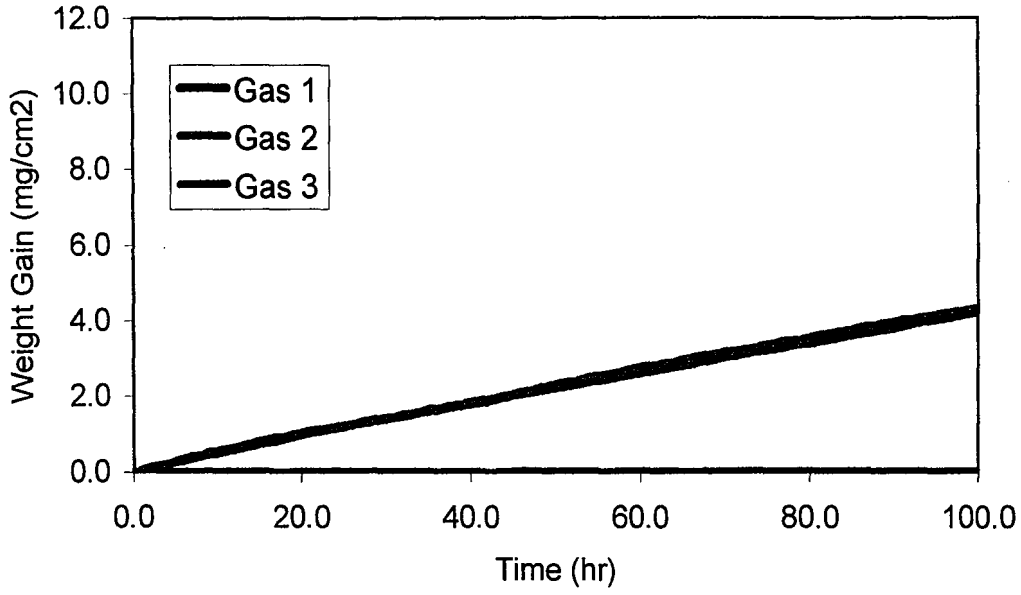

Figure 4. 24: Plot of weight gain vs. time for Fe-10wt%Al exposed to the sulfidizing gases at 500°C for 100 hours.

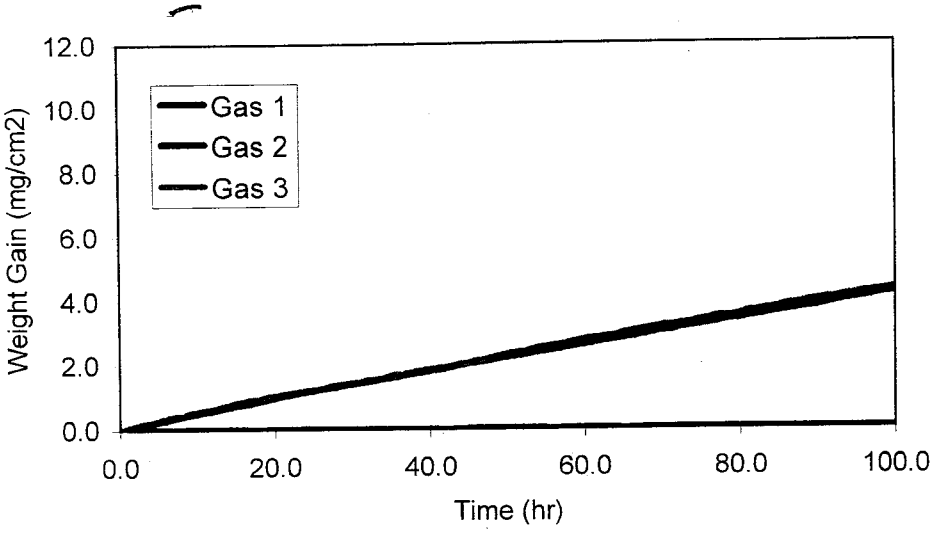

Figure 4. 24: Plot of weight gain vs. time for Fe-10wt%Al exposed to the sulfidizing gases at 500°C for 100 hours.

a)

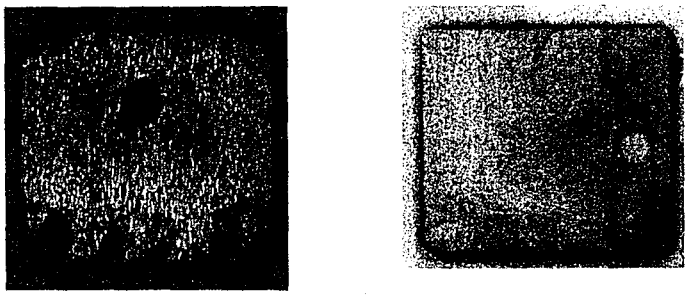

b)

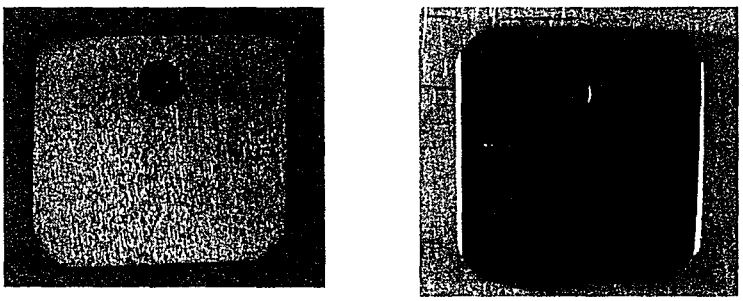

c)

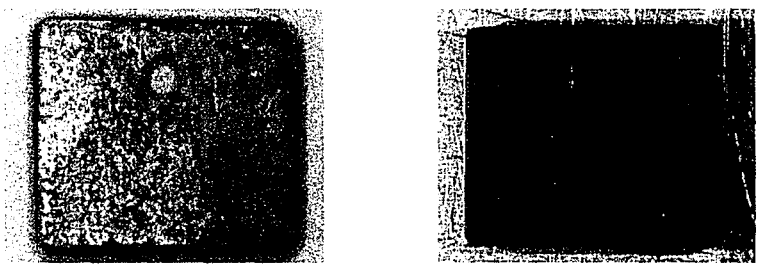

Figure 4. 25: Light optical macrographs of a)IN622, b)IN625, and c)FM72 after 100 hours exposure toGases 4 and 5 at 500C.

a)

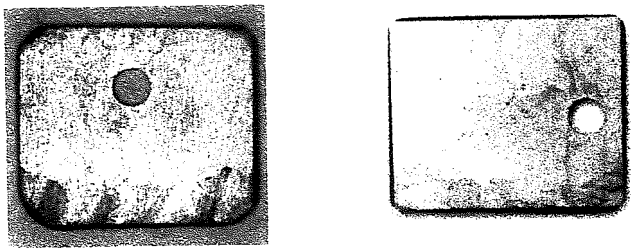

b)

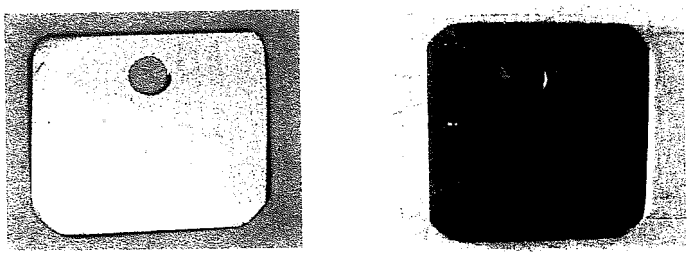

c)

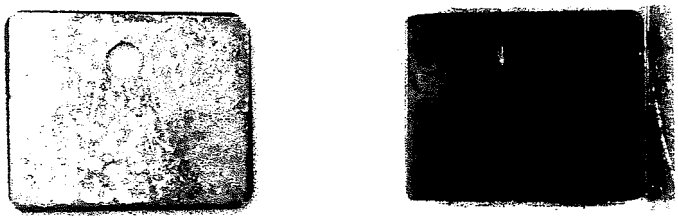

Figure 4. 25: Light optical macrographs of a)IN622, b)IN625, and c)FM72 after 100 hours exposure toGases 4 and 5 at 500C.

a)

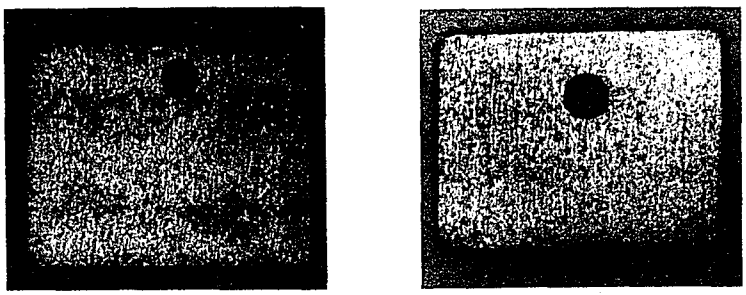

b)

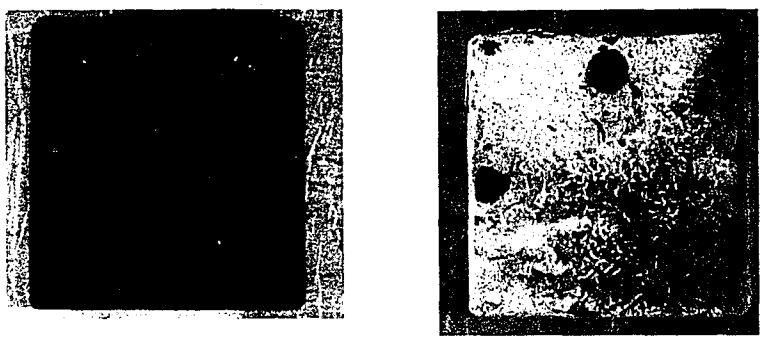

c)

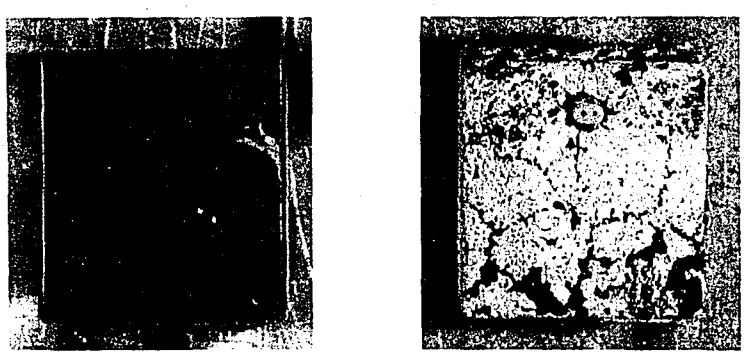

Figure 4. 26: Light optical macrographs of a)309SS b)Fe-1.0Cr-0.5M0 and c)Fe-10wt%Al after 100 hours exposure toGases 4 and 5 at 500C.

a)

b)

c)

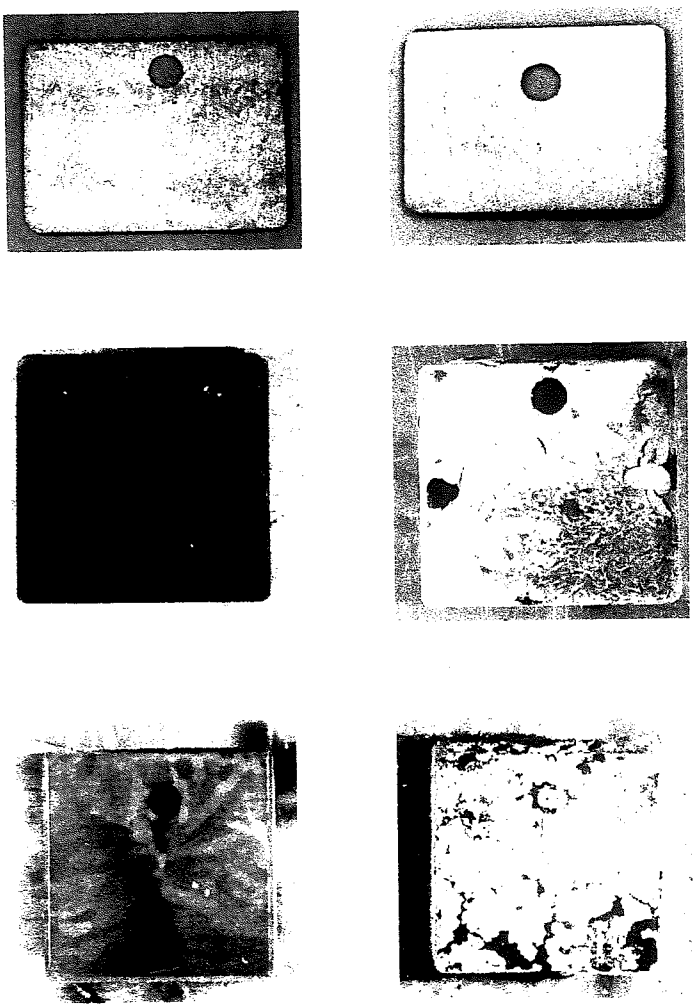

Figure 4. 26: Light optical macrographs of a)309SS b)Fe-1.0Cr-0.5M0 and c)Fe-10wt%Al after 100 hours exposure toGases 4 and 5 at 500C.

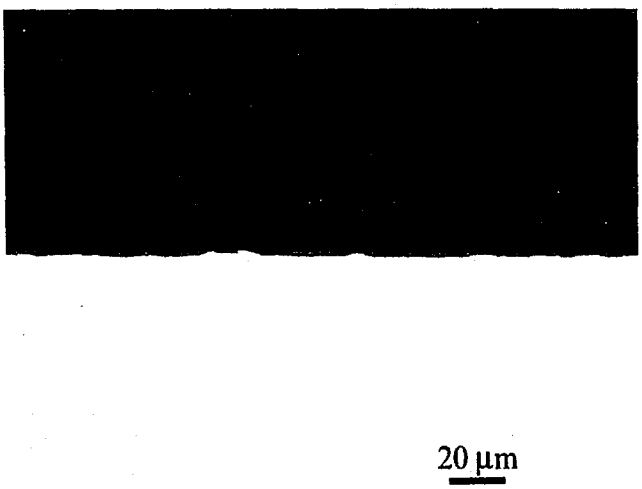

Figure 4. 27: Photomicrograph of the cross section of FM72 exposed to Gas 5 (catalyzed) (catalyzed) at 500°C for 100 hours.

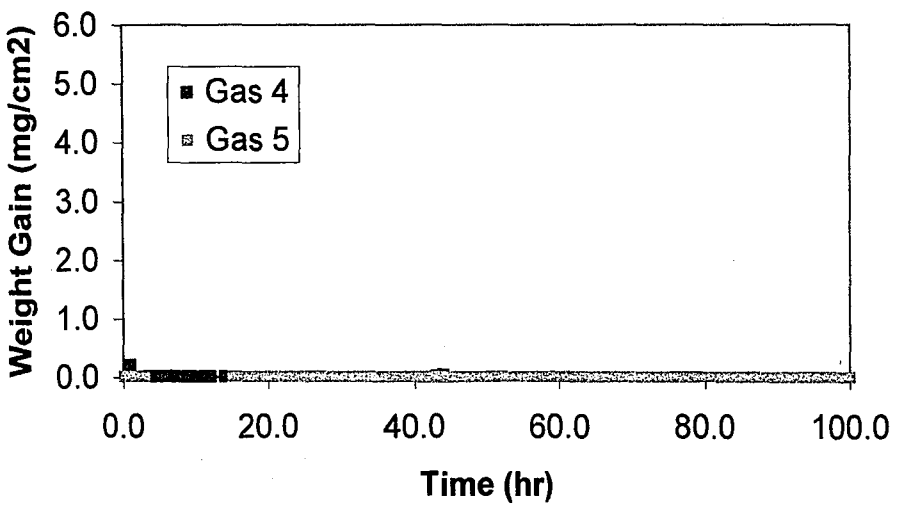

Figure 4. 28: Plot of weight gain vs. time for FM72 in Gases 4 and 5 at 500°C for 100 hours.

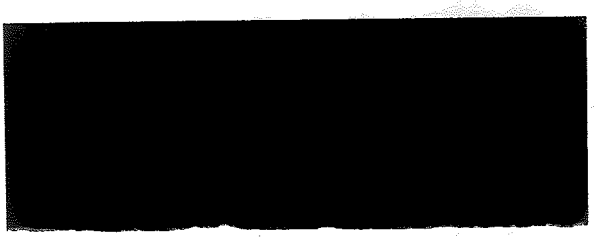

Figure 4. 27: Photomicrograph of the cross section of FM72 exposed to Gas 5 (catalyzed) (catalyzed) at 500°C for 100 hours.

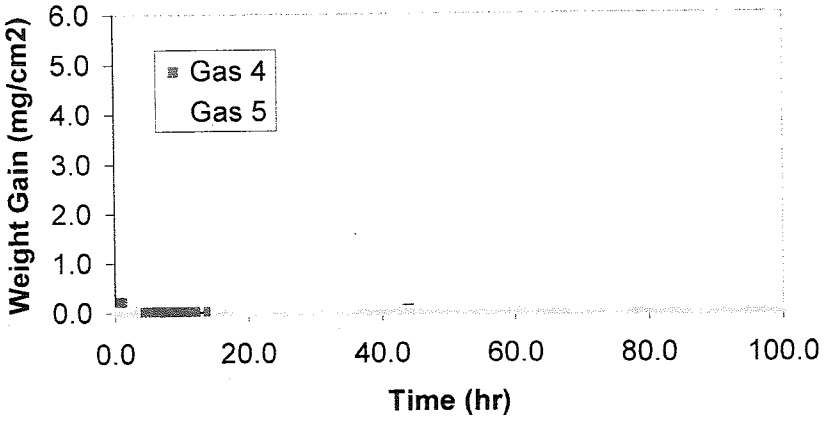

Figure 4. 28: Plot of weight gain vs. time for FM72 in Gases 4 and 5 at 500°C for 100 hours.

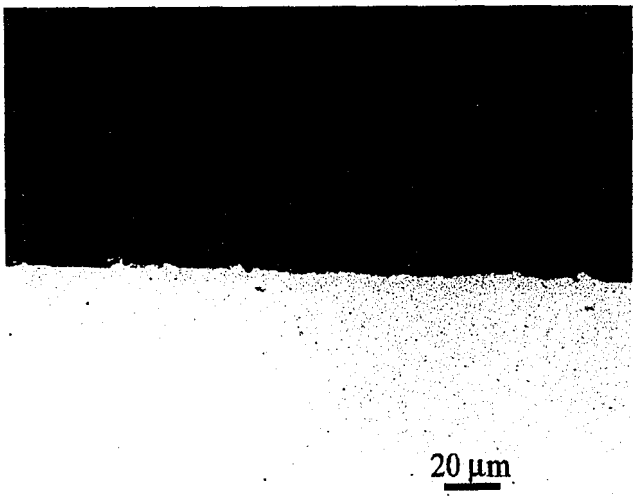

Figure 4. 29: Photomicrograph of the cross section of 309SS exposed to Gas 4 at 500°C for 100 hours.

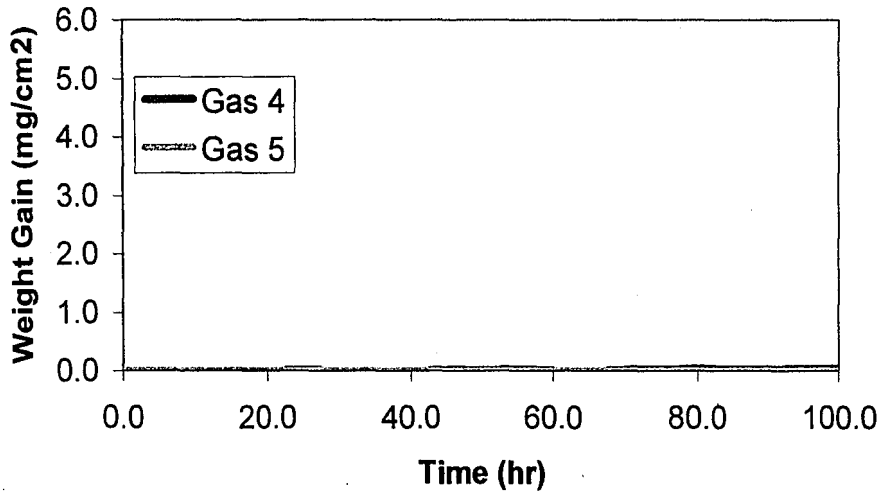

Figure 4. 30: Plot of weight gain vs. time for 309SS exposed to Gases 4 and 5 for 100 hours at 500°C.

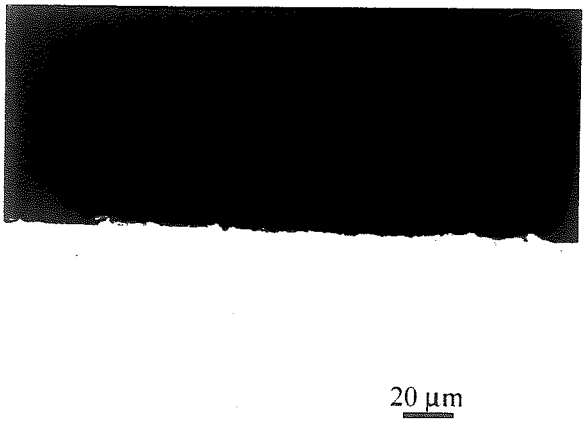

Figure 4. 29: Photomicrograph of the cross section of 309SS exposed to Gas 4 at 500°C for 100 hours.

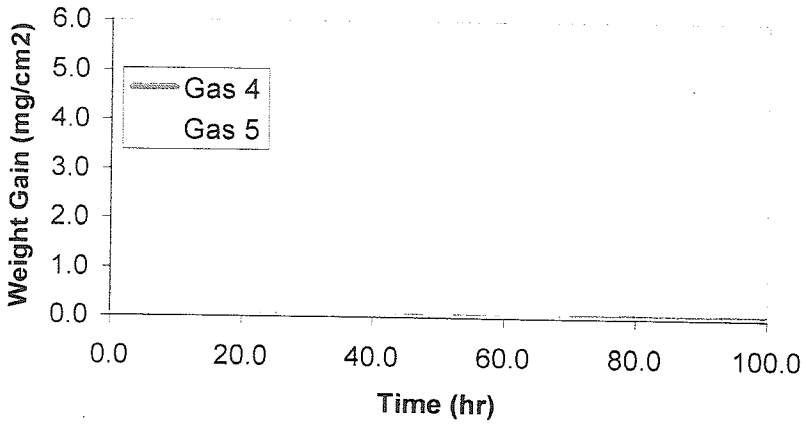

Figure 4. 30: Plot of weight gain vs. time for 309SS exposed to Gases 4 and 5 for 100 hours at 500°C.

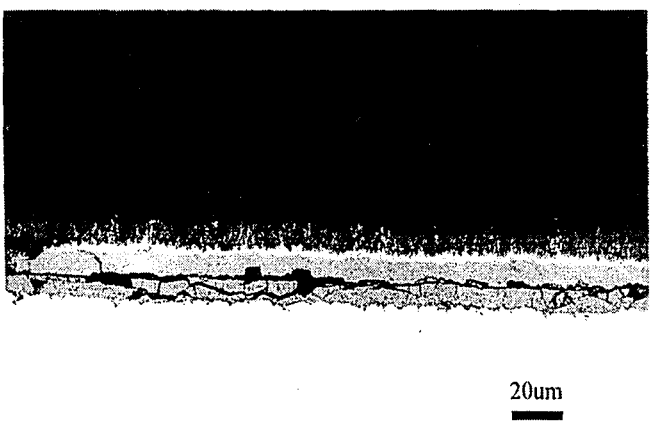

Figure 4. 31: Photomicrograph of the cross section of T11 steel exposed to Gas 4 at 500°C for 100 hours.

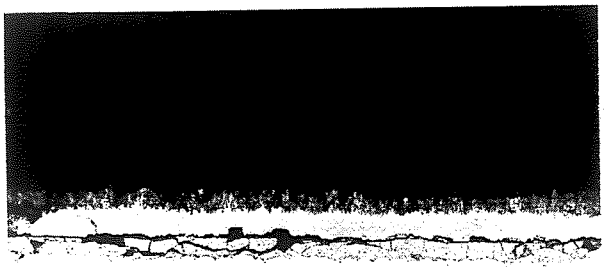

Figure 4. 31: Photomicrograph of the cross section of T11 steel exposed to Gas 4 at 500°C for 100 hours.

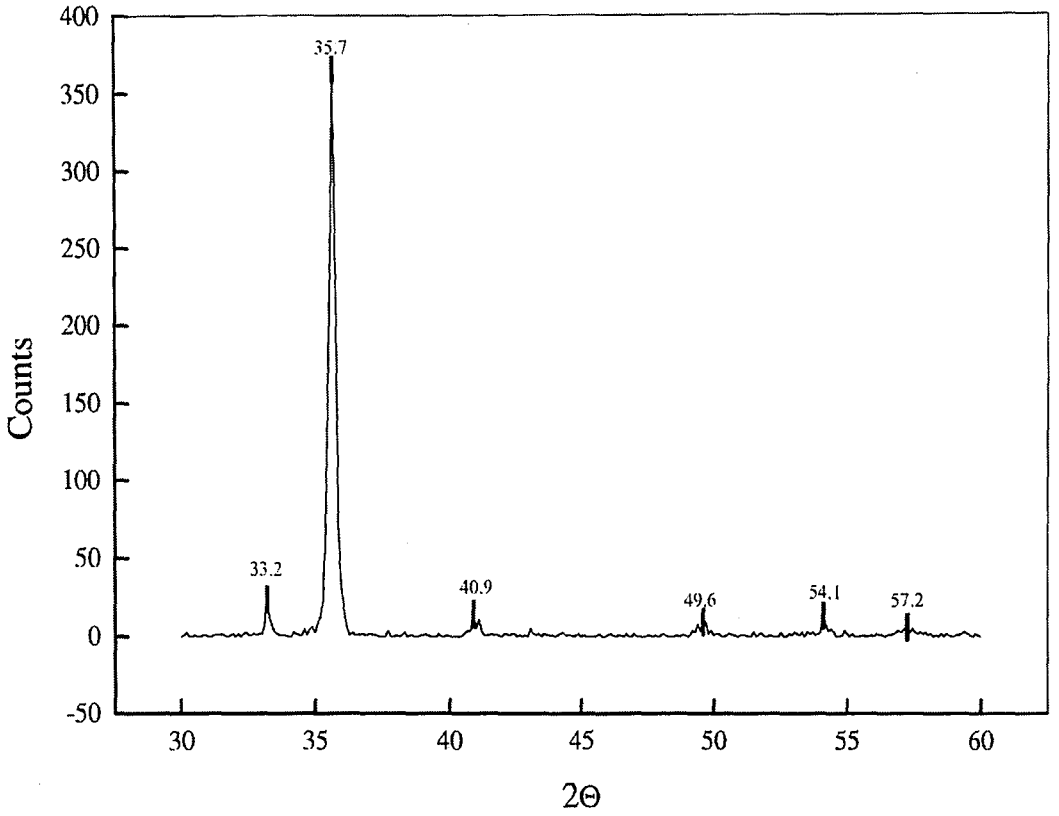

Figure 4. 32: X-ray diffraction spectrum obtained for T11 exposed to Gas 4 performed with Cu Kα radiation. Peaks indicate presence of Fe_2O_3 in corrosion scale.

Table 4. 5: Powder diffraction table for Fe_2O_3 from JCPDS – International Centre for Diffraction Data.

2θ	Relative Intensity
33.45	999
35.88	699
41.18	197
49.86	327
54.55	403
57.88	22

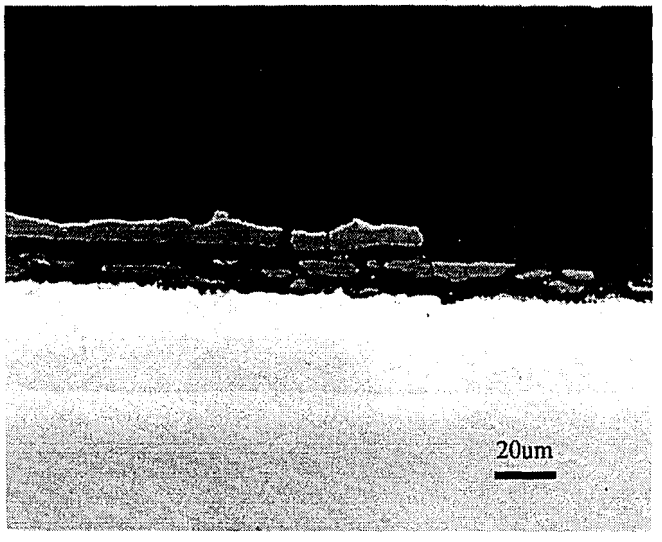

Figure 4. 33: Photomicrograph of the cross section of T11 steel exposed to Gas 5 (catalyzed) (catalyzed) at 500°C for 100 hours.

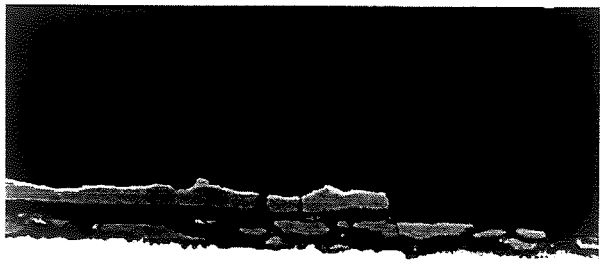

Figure 4. 33: Photomicrograph of the cross section of T11 steel exposed to Gas 5 (catalyzed) (catalyzed) at 500°C for 100 hours.

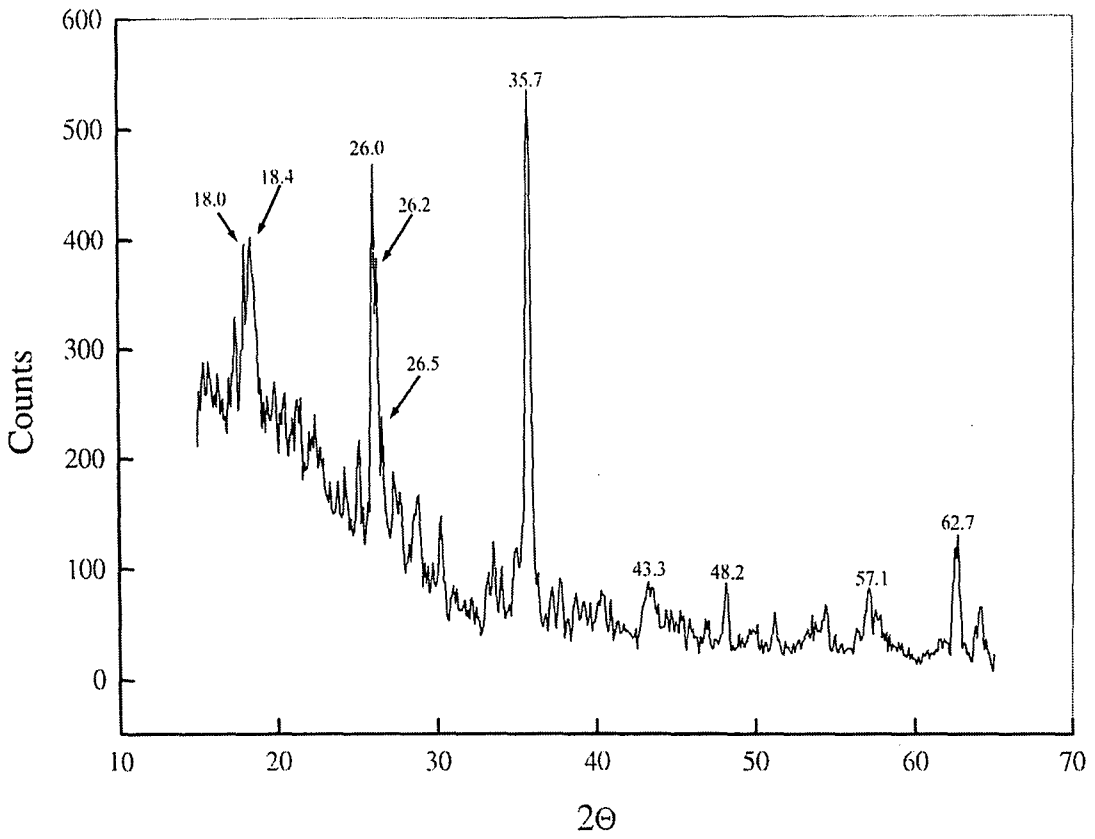

Figure 4. 34: X-ray spectrum obtained for T11 exposed to Gas 5 (catalyzed) (catalyzed) at 500°C for 100 hours

Table 4. 6: List of possible phases formed on T11 exposed to Gas 5 (catalyzed) (catalyzed). Data obtained from JCPDS-International Centre for Diffraction Data.

T-11 Gas5	FeS	FeS2	Fe2O3	Fe3O4	Fe2(SO4)3	FeSO4	Cr2O3	CrS	Cr2S3	Possible Compounds
17.4										?
17.9										?
18.2	18.73			18.988					18.038	FeS, Fe3O4, Cr2S3
18.5										
24.9			24.33		24.052	24.355	24.494			Fe2O3, FeSO4, Fe2(SO4)3
					24.742					
25.9										FeSO4
27.1									27.5	Cr2S3
27.3										
27.5										
28.7		28.51						28.161		FeS2, CrS
30.2	30.4							30.198	30.08	FeS, CrS
33.5	33.69	33.04	33.45		33.458		33.597	33.756		FeS, FeS2, Fe2O3, Fe2(SO4)3, CrS
						34.001				
34.9						34.116		34.194	34.206	FeSO4, CrS
35.7	35.55		35.88							FeS, Fe2O3
43.3	43.18							43.035		FeS
48.2					48.869			48.51		Fe2(SO4)3, CrS
57.1										?
62.7			62.94							Fe2O3

a)

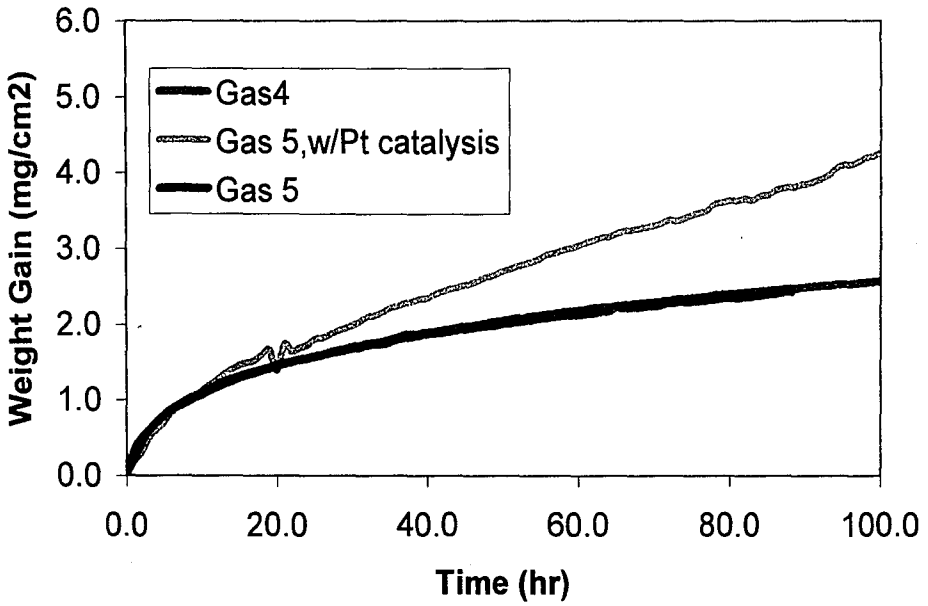

b)

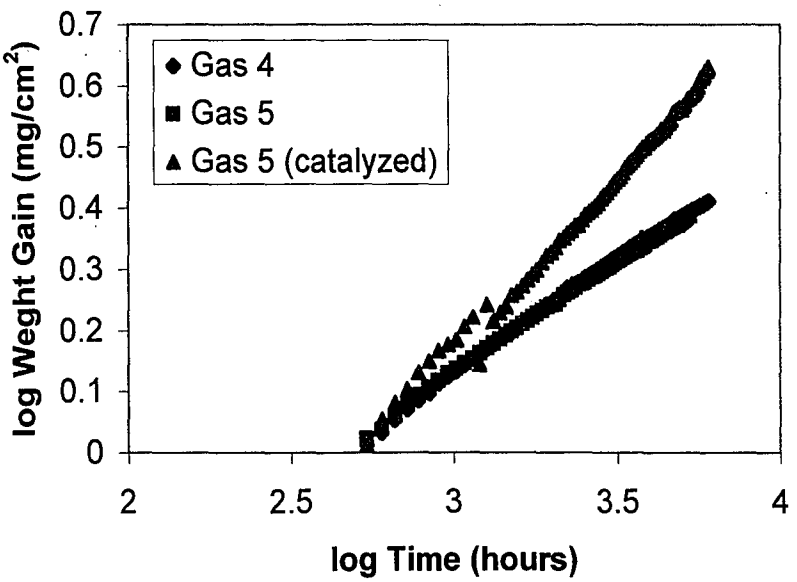

Figure 4. 35: Plot of weight gain vs. time for T11 exposed to Gases 4, 5, and 5 (Pt catalyzed) for 100 hours at 500°C: a) linear and b)logarithmic.

a)

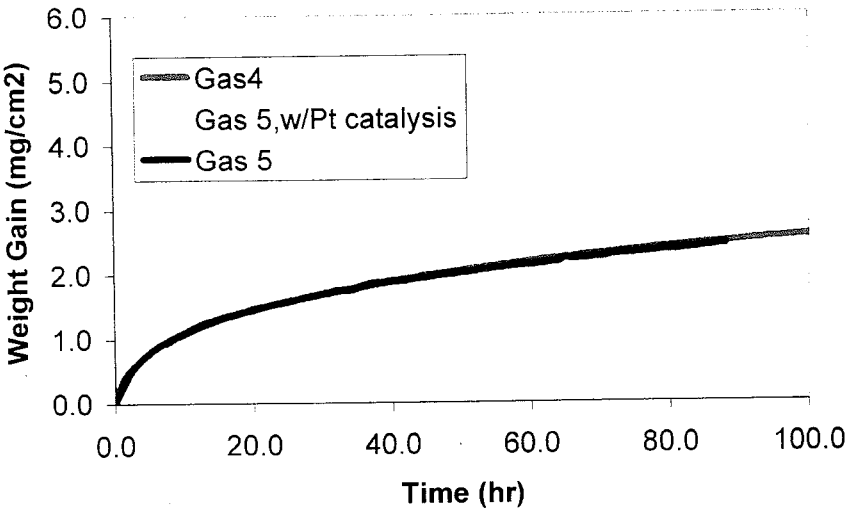

b)

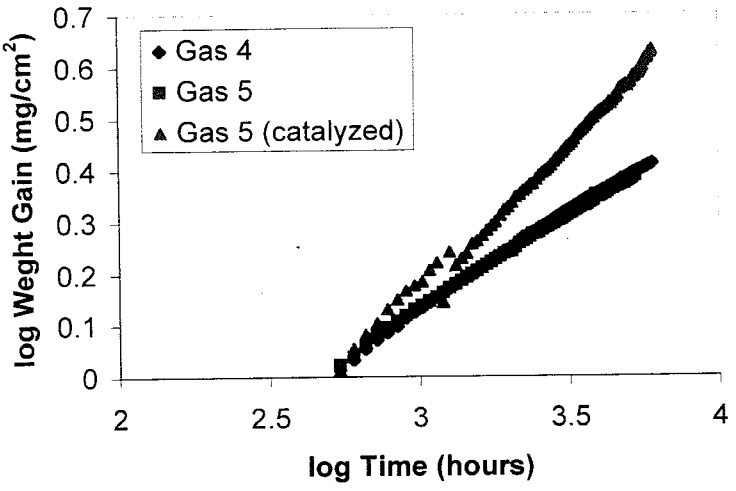

Figure 4. 35: Plot of weight gain vs. time for T11 exposed to Gases 4, 5, and 5 (Pt catalyzed) for 100 hours at 500°C: a) linear and b)logarithmic.

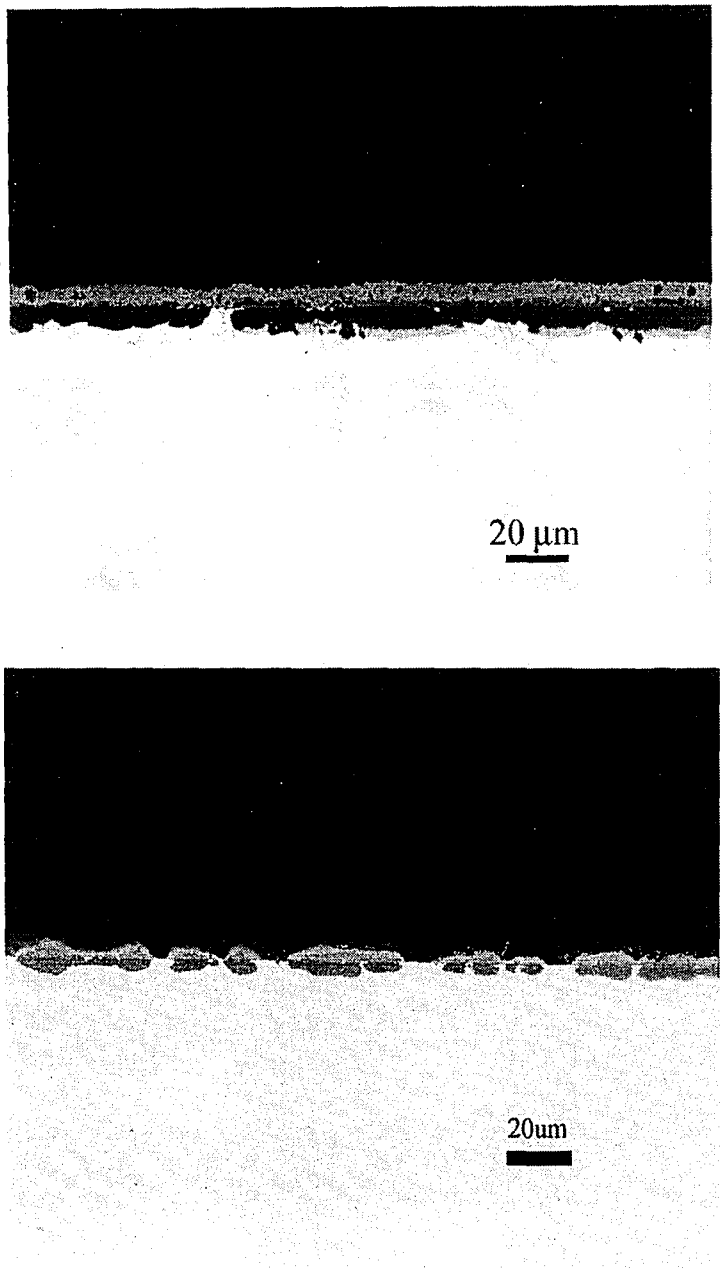

Figure 4. 36: Photomicrograph of the cross section of Fe-10wt%Al exposed to a) Gas 4 and b) Gas 5 (non-catalyzed) at 500°C for 100 hours.

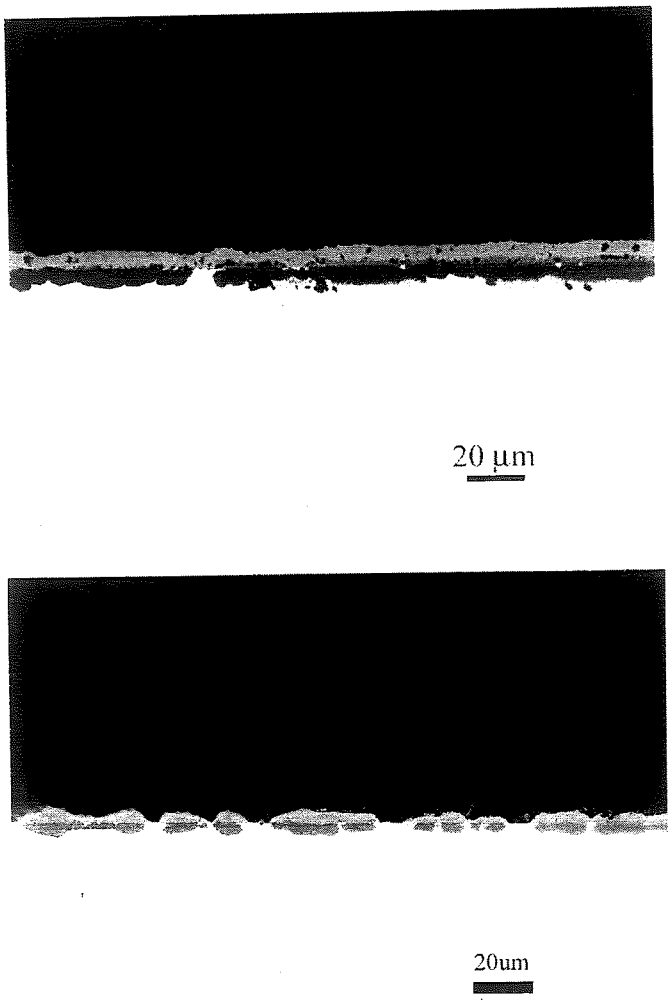

Figure 4. 36: Photomicrograph of the cross section of Fe-10wt%Al exposed to a) Gas 4 and b) Gas 5 (non-catalyzed) at 500°C for 100 hours.

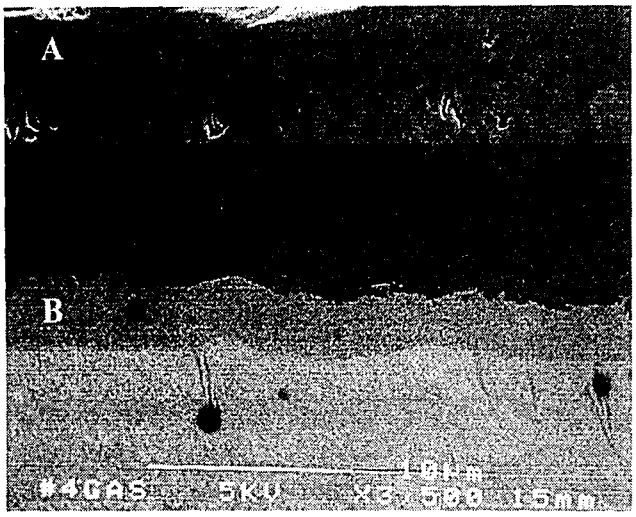

Figure 4. 37: Scanning electron microscope image of Fe-10wt%Al exposed to Gas 4 at 500°C for 100 hours. A and B designate areas for EDS.

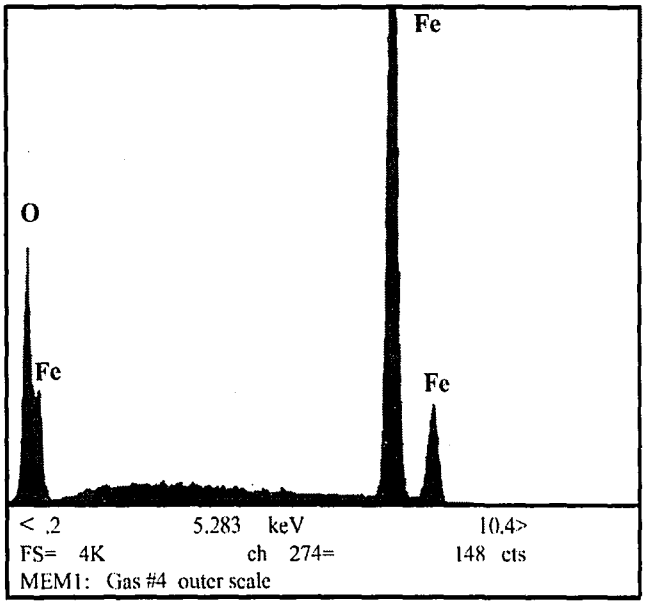

Figure 4. 38: EDS spectrum obtained from area A in Figure 4. 37.

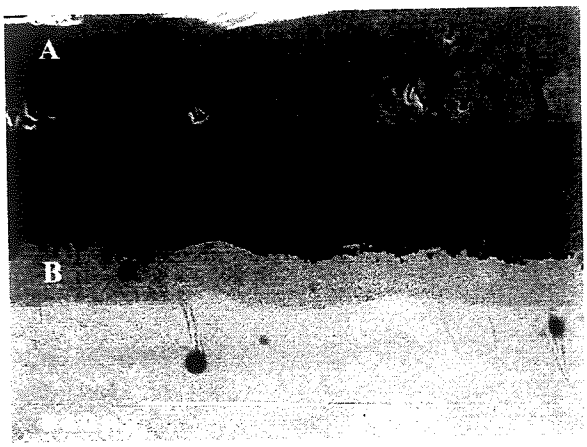

Figure 4. 37: Scanning electron microscope image of Fe-10wt%Al exposed to Gas 4 at 500°C for 100 hours. A and B designate areas for EDS.

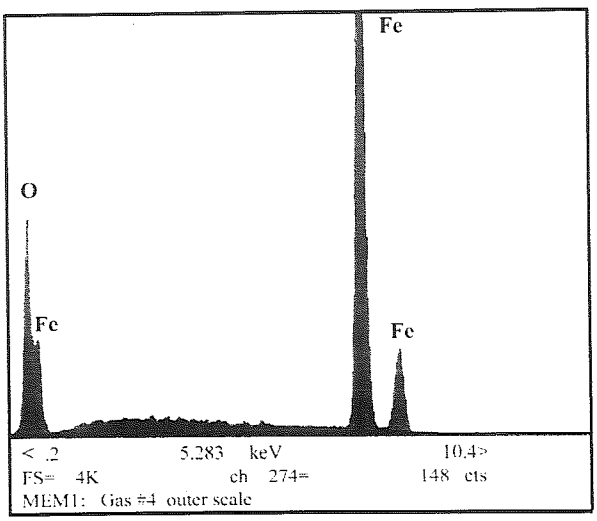

Figure 4. 38: EDS spectrum obtained from area A in Figure 4. 37.

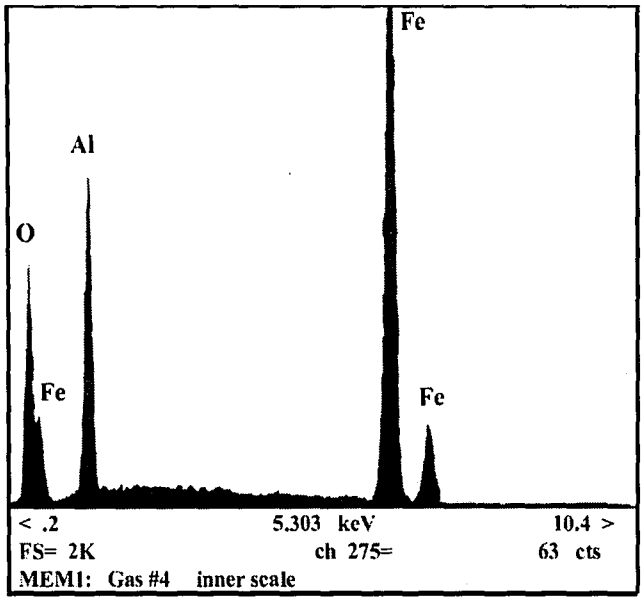

Figure 4. 39: EDS spectrum obtained from area B in Figure 4. 37.

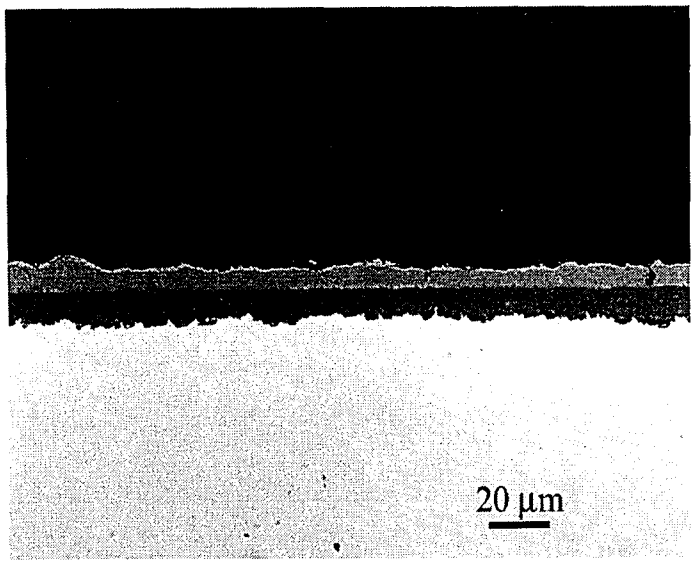

Figure 4. 40: Photomicrograph of cross section of Fe-10wt%Al exposed to Gas 5 (catalyzed) at 500°C for 100 hours.

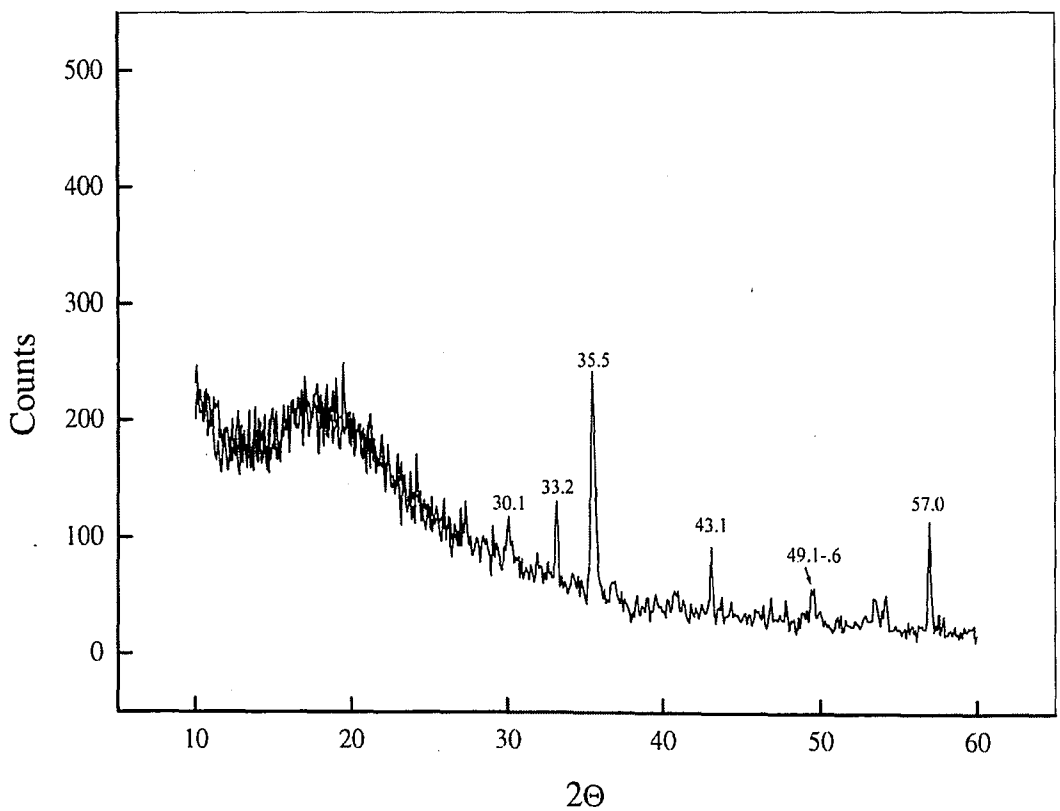

Figure 4. 41: X-ray spectrum obtained for Fe-10wt%Al exposed to Gas 5 (catalyzed) (catalyzed).

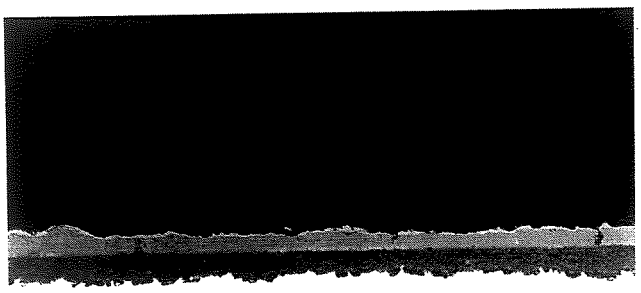

Figure 4. 40: Photomicrograph of cross section of Fe-10wt%Al exposed to Gas 5 (catalyzed) at 500°C for 100 hours.

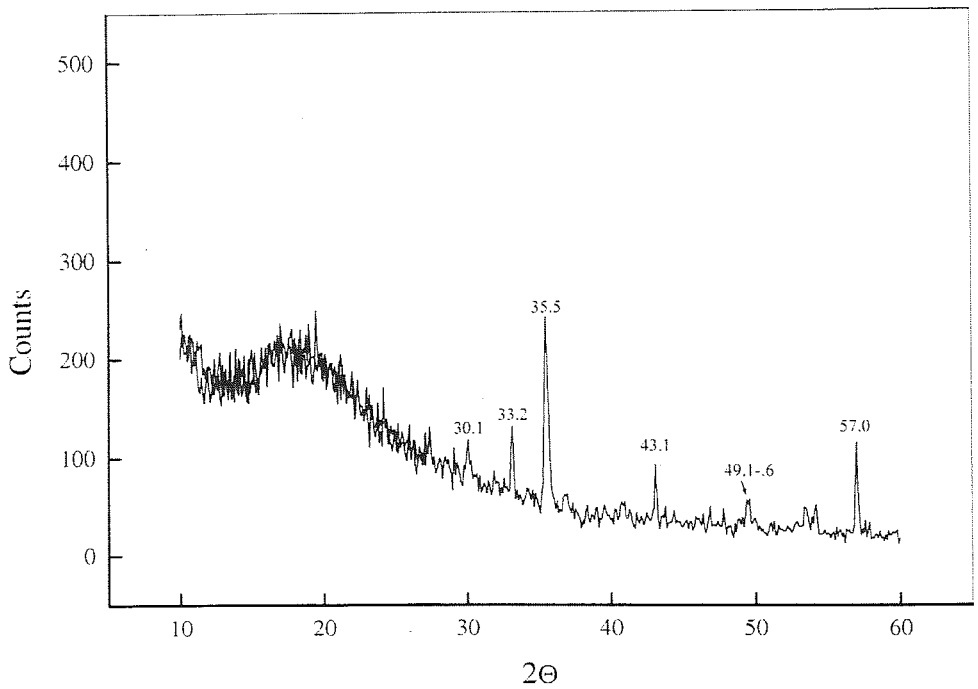

Figure 4. 41: X-ray spectrum obtained for Fe-10wt%Al exposed to Gas 5 (catalyzed) (catalyzed).

Table 4. 7: List of possible phases formed on Fe-10wt%Al exposed to Gas 5 (catalyzed). Data obtained from JCPDS – International Centre for Diffraction Data.

Fe10Al, Gas5	FeS	FeS2	Fe2O3	Fe3O4	Fe2(SO4)3	FeSO4	Cr2O3	CrS	Cr2S3	Possible Compounds
12.9										?
16.3										?
18.7	18.73			18.99					18.04	FeS, Fe3O4
19.8										
22.4						22.268				FeSO4
24.7			24.33		24.052	24.355	24.49			Fe2O3, FeSO4, Fe2(SO4)3
					24.742					
26.2						26.091				FeSO4
27.2									27.5	NiS2, Cr2S3
27.7								28.16		
30.1	30.4							30.2	30.08	FeS,
33.2	33.69	33.04	33.45		33.458		33.6	33.76		FeS, FeS2, Fe2O3, Fe2(SO4)3
35.5	35.55		35.88							FeS, Fe2O3
43.1	43.18							43.04		FeS
49.5			49.86			49.907				Fe2O3, Fe2SO4
57.1										?

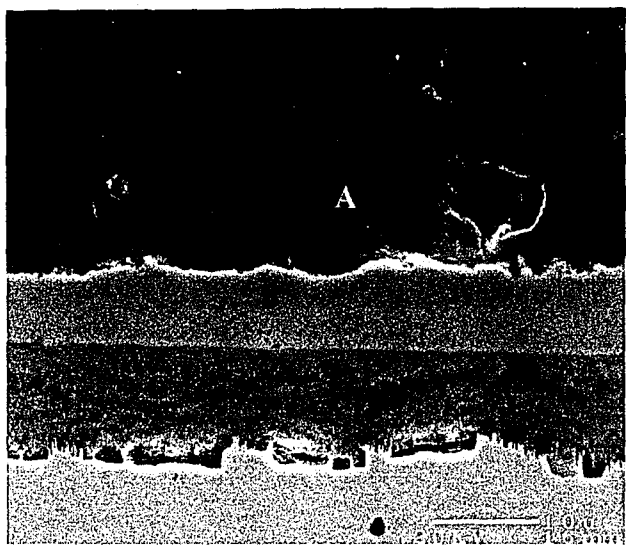

Figure 4. 42: SEM image of cross section of Fe-10wt%Al exposed to Gas 5 (catalyzed). A , B, and C indicate areas where EDS was performed.

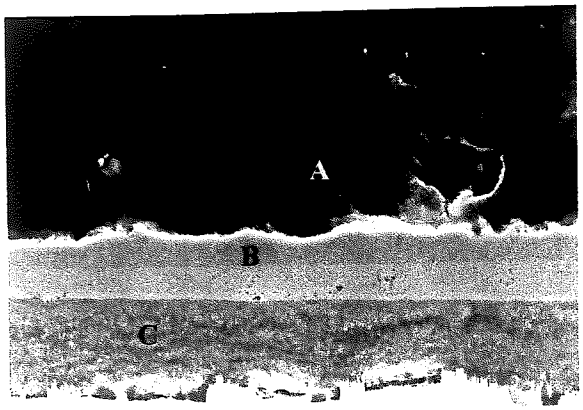

Figure 4. 42: SEM image of cross section of Fe-10wt%Al exposed to Gas 5 (catalyzed). A , B, and C indicate areas where EDS was performed.

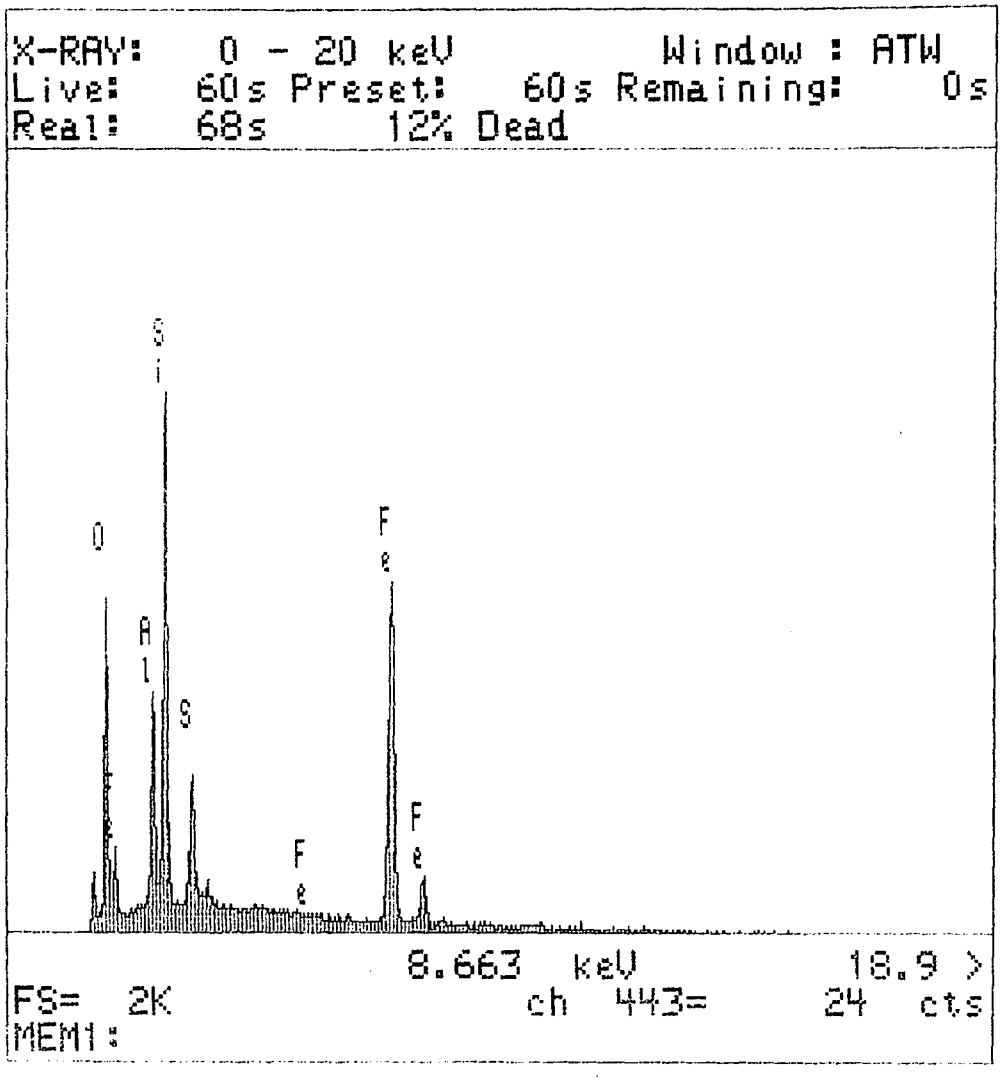

Figure 4. 43: EDS spectrum obtained from area A in Figure 4. 42.

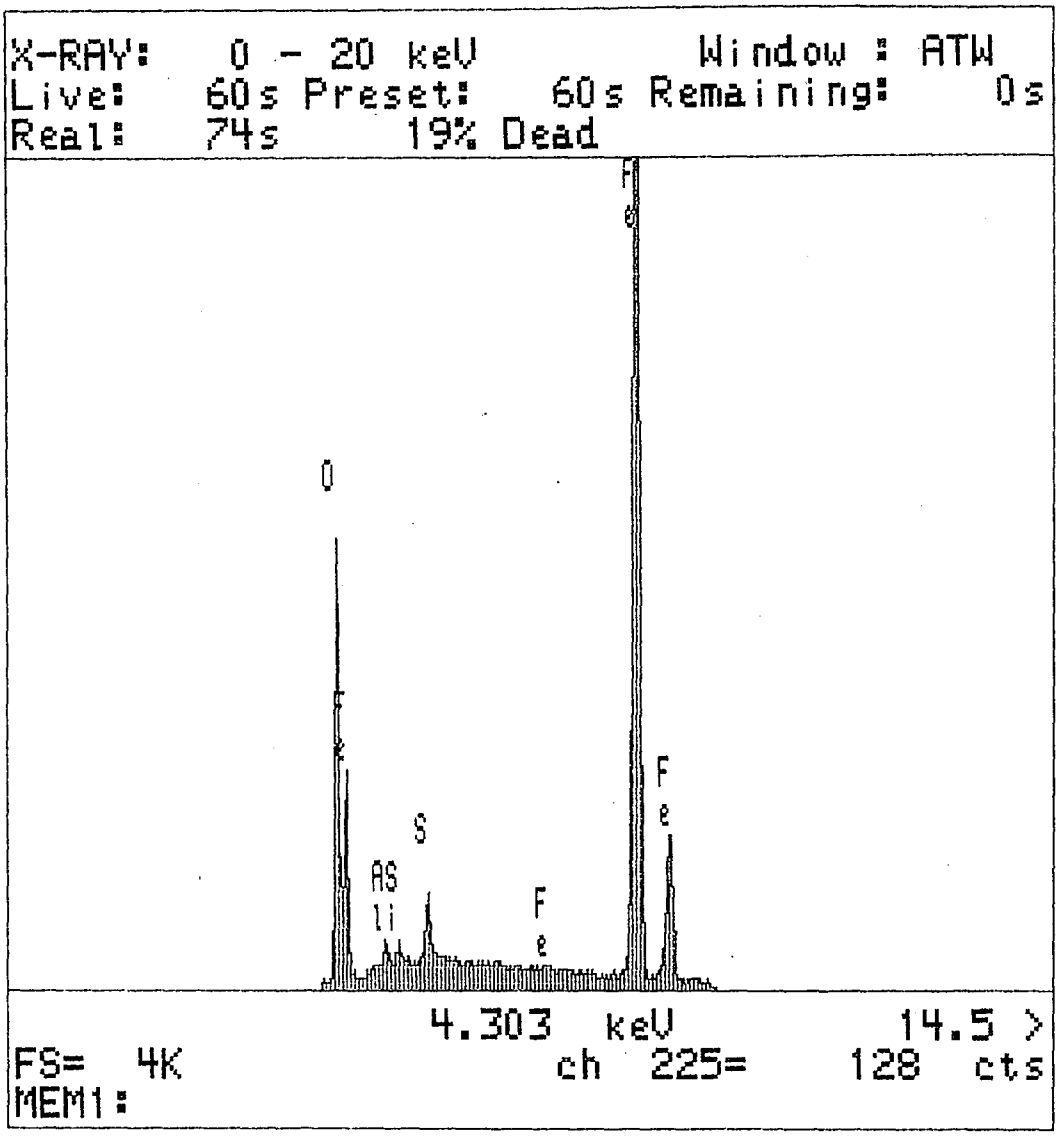

Figure 4. 44: EDS spectrum obtained from area B in Figure 4. 42.

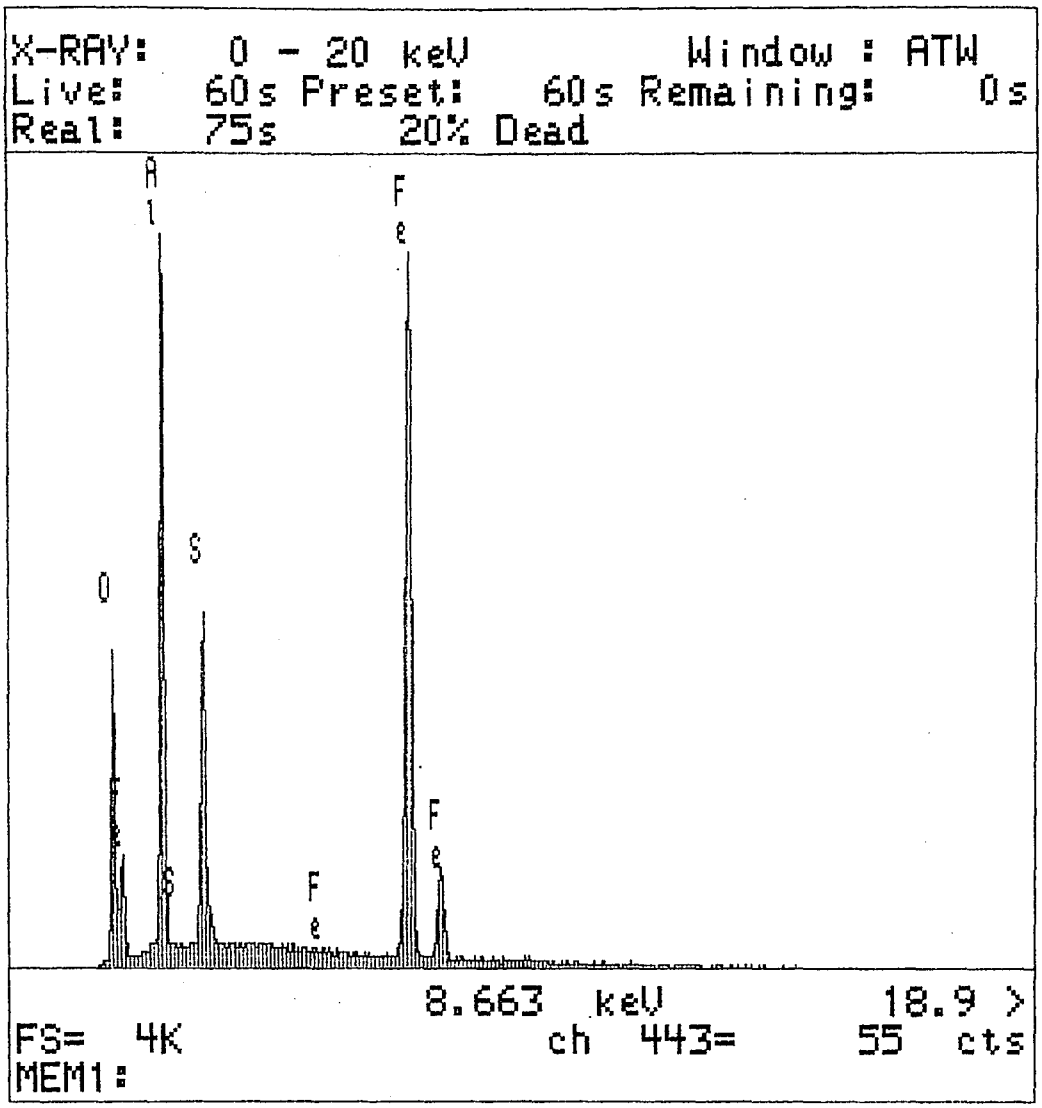

Figure 4. 45: EDS spectrum obtained from area C in Figure 4. 42.

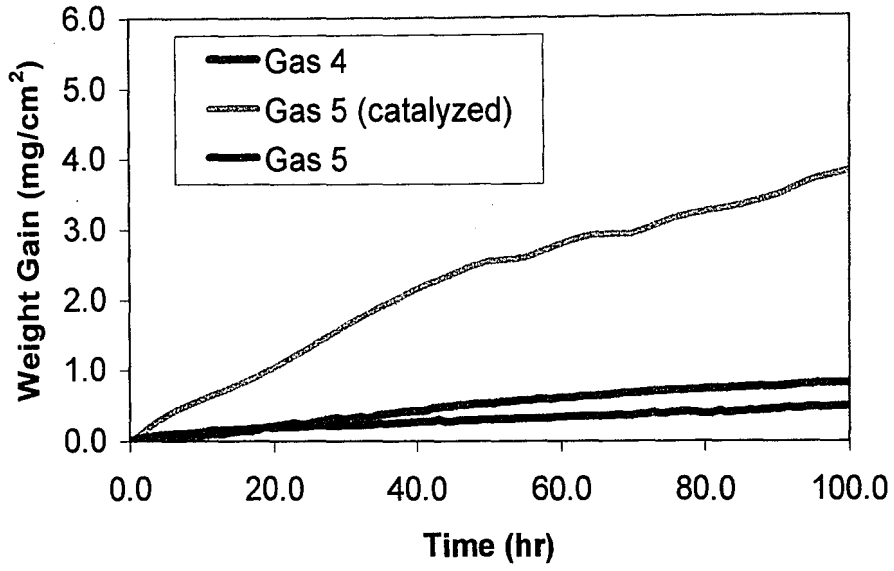

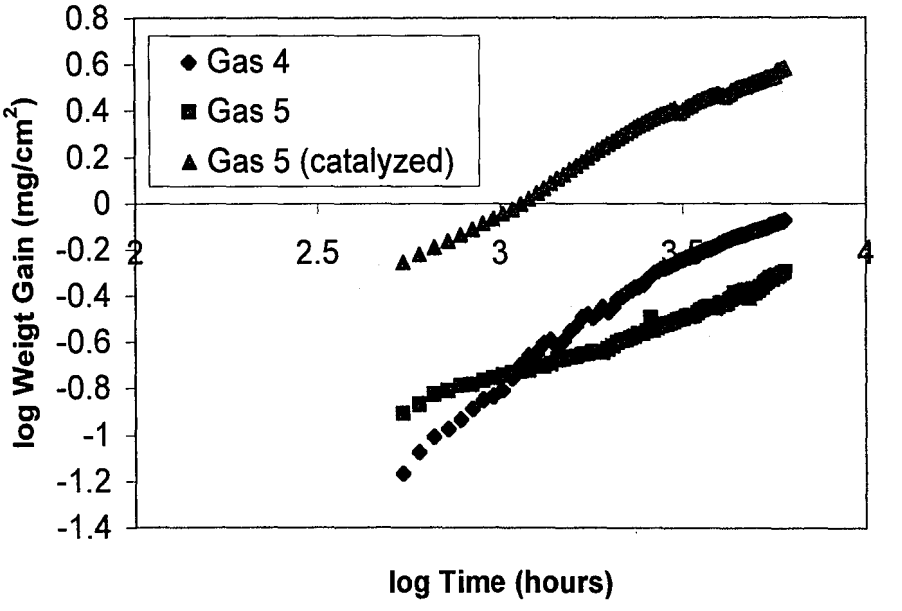

Figure 4. 46: Plot of weight gain vs. time a) linear and b)logarithmic for Fe-10wt%Al exposed to Gases 4 and 5 (catalyzed and non-catalyzed) at 500°C 100 hours.

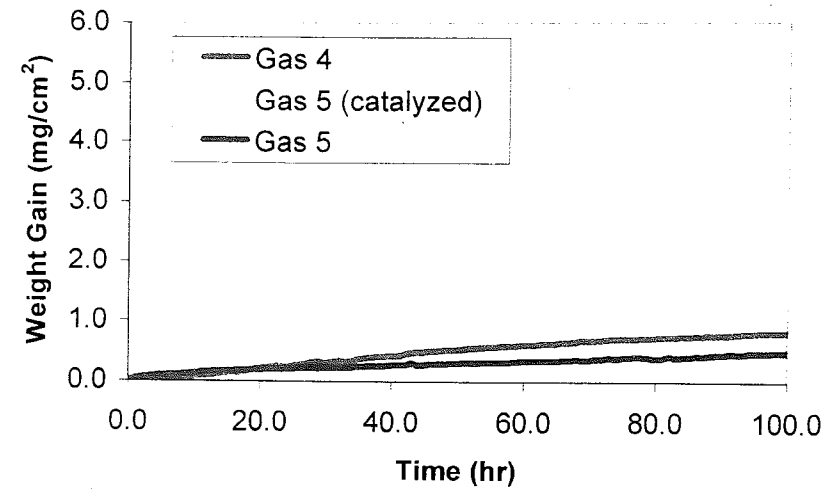

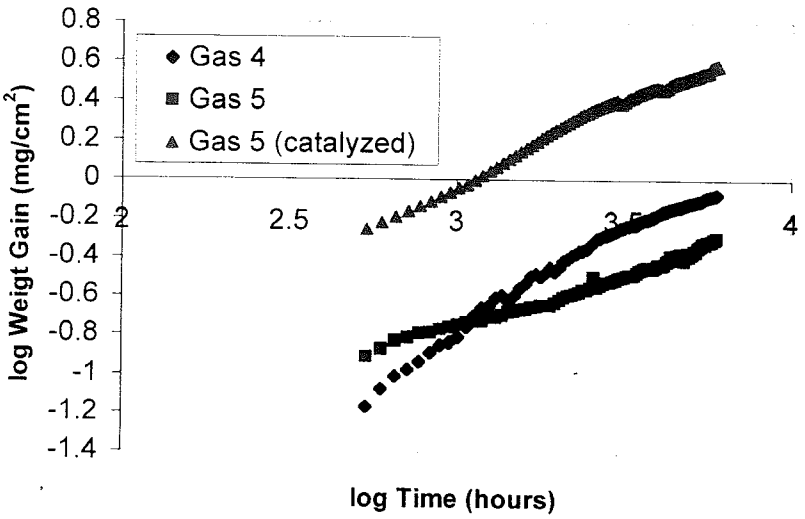

Figure 4. 46: Plot of weight gain vs. time a) linear and b)logarithmic for Fe-10wt%Al exposed to Gases 4 and 5 (catalyzed and non-catalyzed) at 500°C 100 hours.

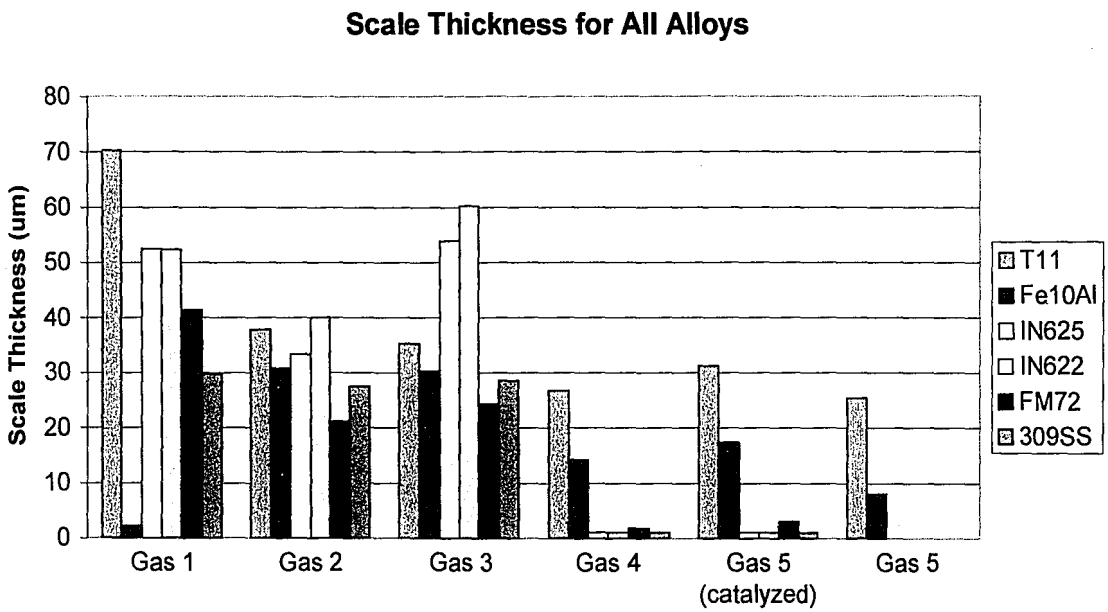

Figure 4. 47: Comparison of scale thickness for each alloy exposed to each gas composition. (Gas 5 non-catalyzed Fe-10wt%Al represents largest value of non-uniform corrosion product)

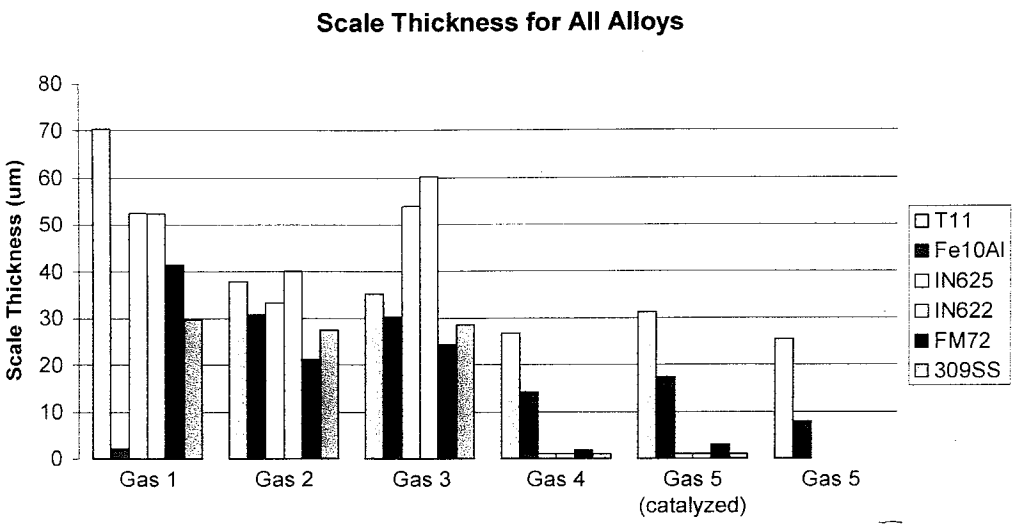

Figure 4. 47: Comparison of scale thickness for each alloy exposed to each gas composition. (Gas 5 non-catalyzed Fe-10wt%Al represents largest value of non-uniform corrosion product)

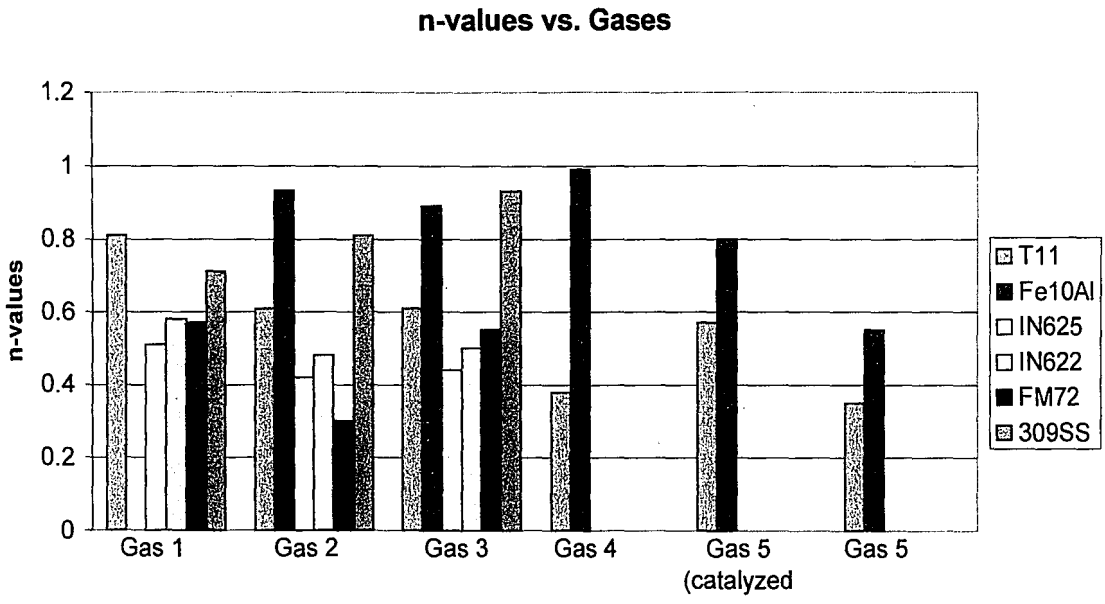

Figure 4. 48: Comparison of n-values for each alloy exposed to each gas composition.

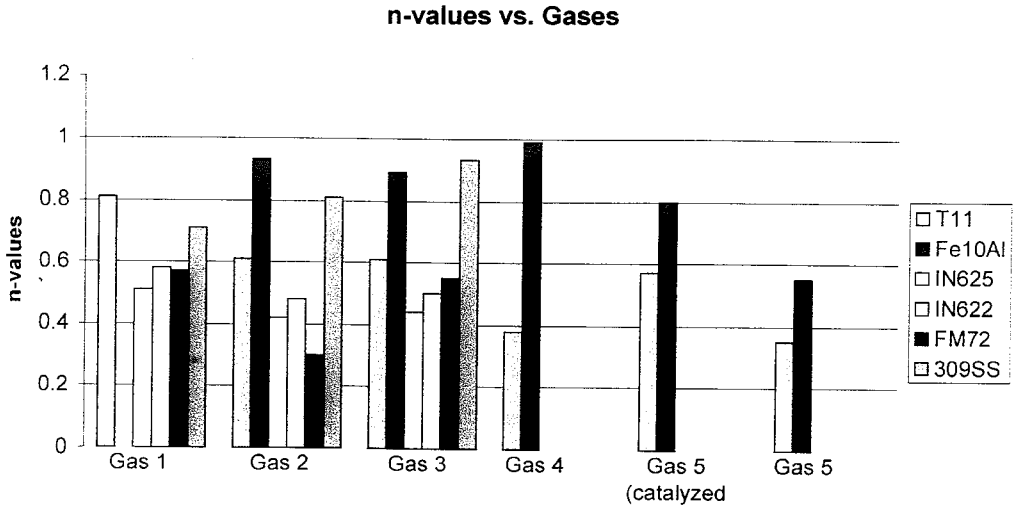

Figure 4. 48: Comparison of n-values for each alloy exposed to each gas composition.

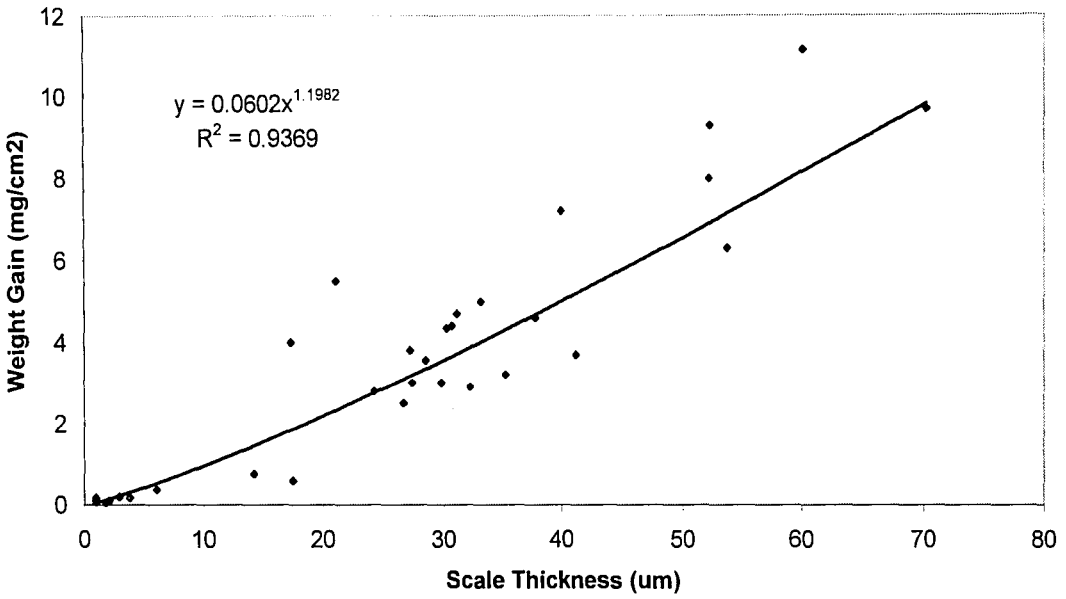

Figure 4. 49: Plot of weight gain vs. scale thickness for all alloys exposed to all gas compositions.

Table 4. 8: Summary of corrosion kinetics and scale thickness of each alloy exposed to each gas composition.

Gas	Alloy	Equation	R2	thickness (um)
1	IN622	y = 0.5841x - 1.316	R2 = 0.991	52.25
2	IN622	y =0.4856x - 0.5006	R2 = 0.9646	40.00
3	IN622	y = 0.4969x - 0.8133	R2 = 0.9924	60.13
1	IN625	y = 0.50780x - 0.9398	R2 = 0.9732	52.35
2	IN625	y = 0.4236x - 0.8935	R2 = 0.9933	33.22
3	IN625	y = 0.4475x - 0.888	R2 = 0.9602	53.78
1	FM72	y = 0.5759x - 1.4541	R2 = 0.9958	41.25
2	FM72	y = 0.2963x - 0.62	R2 = 0.9534	21.13
3	FM72	y = 0.556x - 1.62269	R2 = 0.9027	24.35
1	309SS	y = 0.7088x - 2.0046	R2 = 0.9916	29.8
2	309SS	y = 0.8094 - 2.5803	R2 = 0.996	27.41
3	309SS	y = .9305 - 2.8897	R2 = 0.9996	28.54
1	T11	y = 0.8114x - 2.0921	R2 = 0.9882	70.24
2	T11	y = 0.6084x - 1.625	R2 = 0.9789	37.8
3	T11	y = 0.6174x - 1.8005	R2 = 0.997	35.29
4	T11	y = 0.3827x - 1.0238	R2 = 0.9952	26.74
5	T11	y = 0.3538x - 0.9274	R2 = 0.9984	25.33
5 (catalyzed)	T11	y = 0.57x - 1.5434	R2 = 0.9952	31.17
1	Fe-10Al	undefined		2.1
2	Fe-10Al	y = 0.9346x - 2.9041	R2 = 0.9997	30.7
3	Fe-10Al	y = 0.895x - 2.744	R2 = 0.9995	30.27
4	Fe-10Al	y = 0.9117x - 3.4787	R2 = 0.9493	14.24
5	Fe-10Al	y = 0.5588x - 2.4419	R2 = 0.9849	7.97
5 (catalyzed)	Fe-10Al	y = 0.7842x - 2.361	R2 = 0.9921	17.35

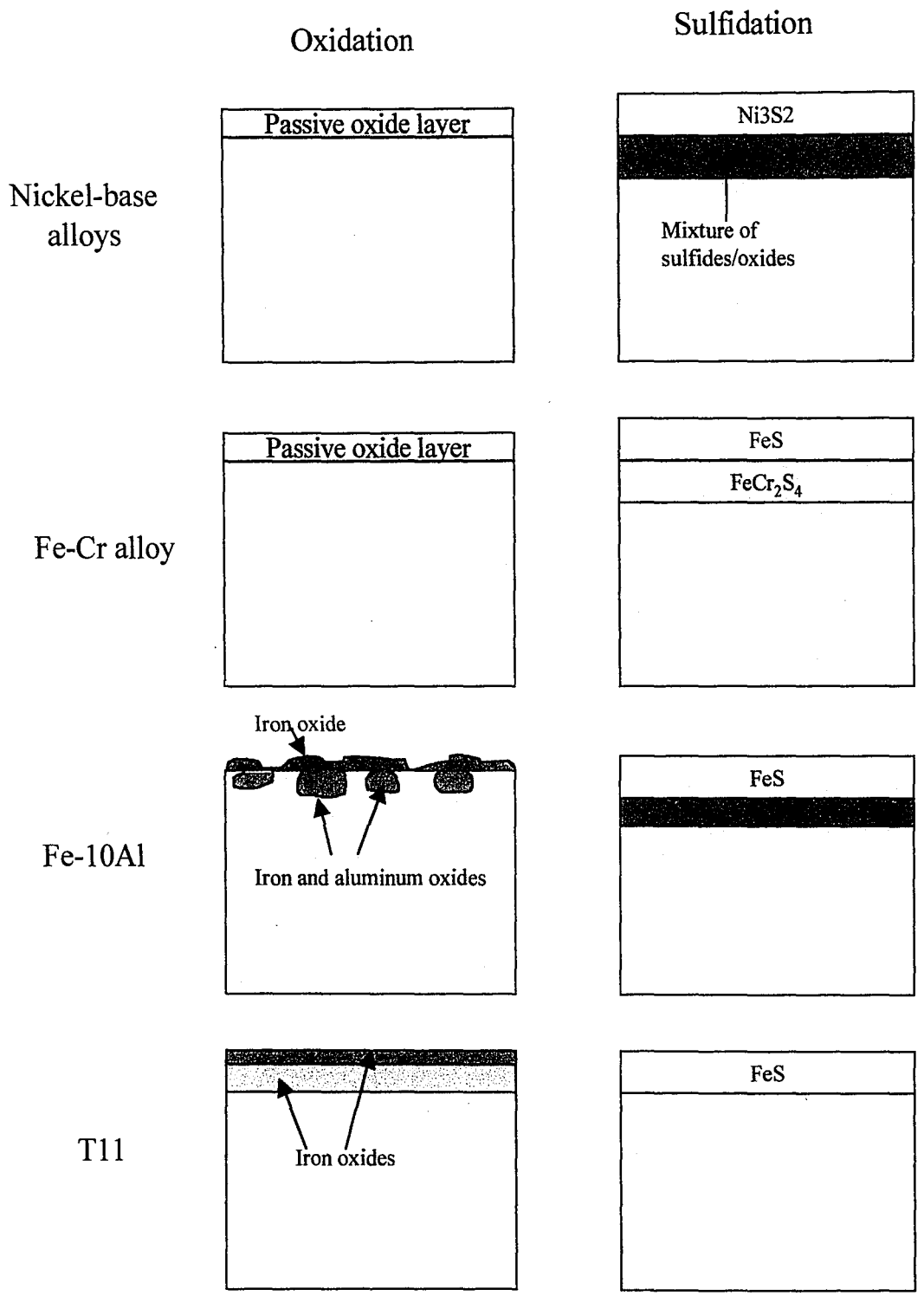

Figure 4. 50: Schematic illustration of the oxidaton and sulfidation of each alloy.

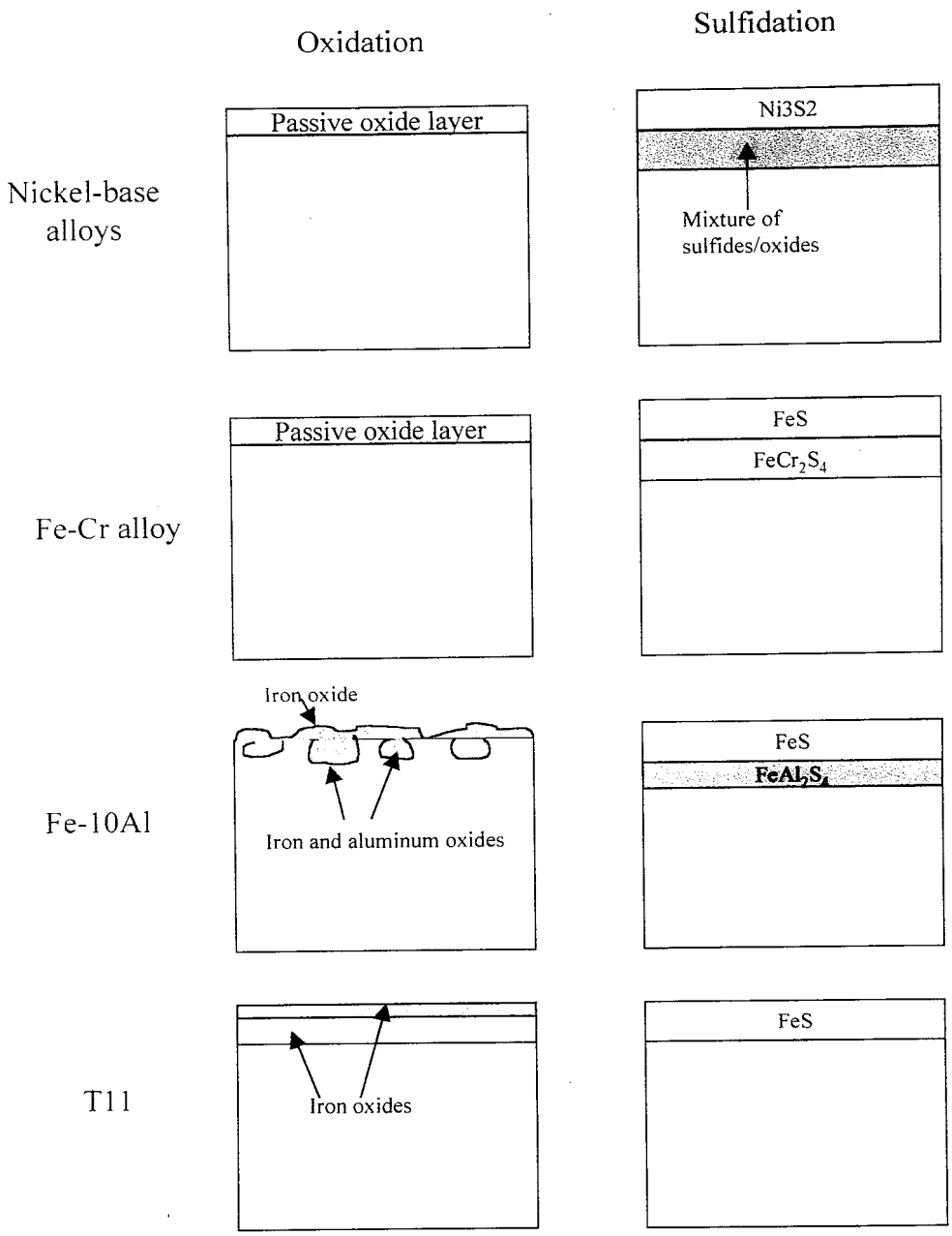

Figure 4. 50: Schematic illustration of the oxidaton and sulfidation of each alloy.

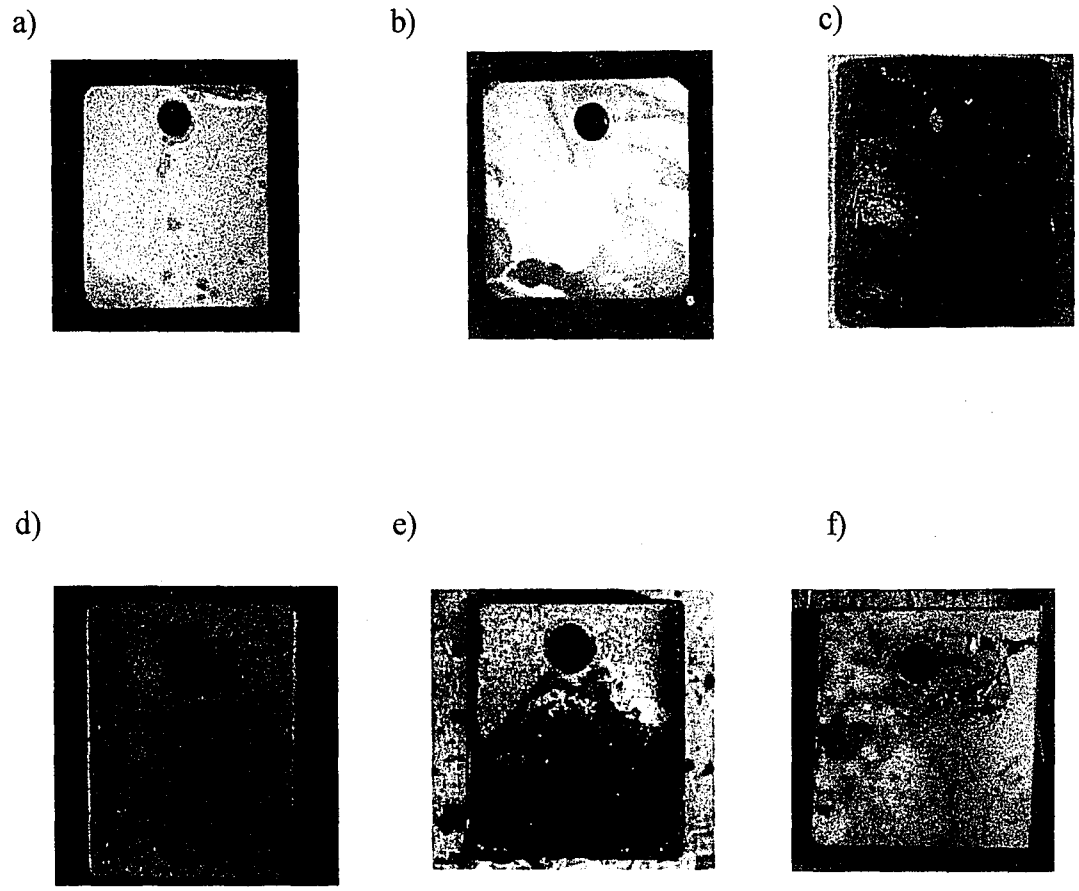

Figure 4. 51: Light optical macrographs of a)IN622, b)IN625, c) FM72, d) 309SS, e)T11 and f) Fe-10wt%Al after 96 hours exposure to cyclic gas atmosphere at 500°C.

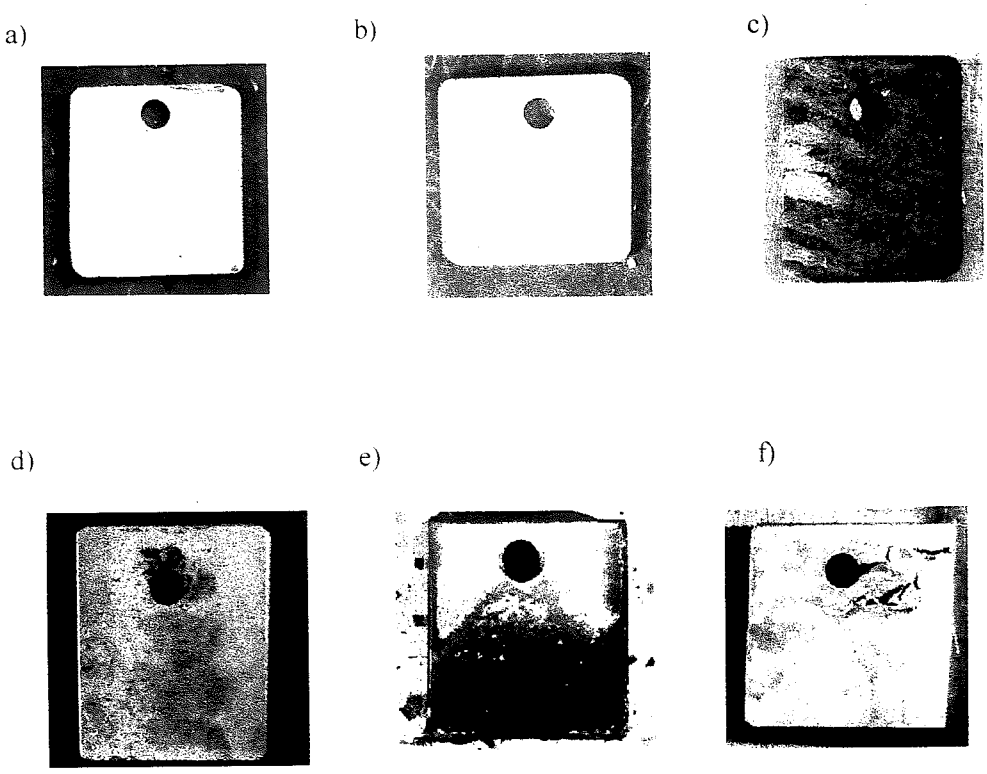

Figure 4. 51: Light optical macrographs of a)IN622, b)IN625, c) FM72, d) 309SS, e)T11 and f) Fe-10wt%Al after 96 hours exposure to cyclic gas atmosphere at 500°C.

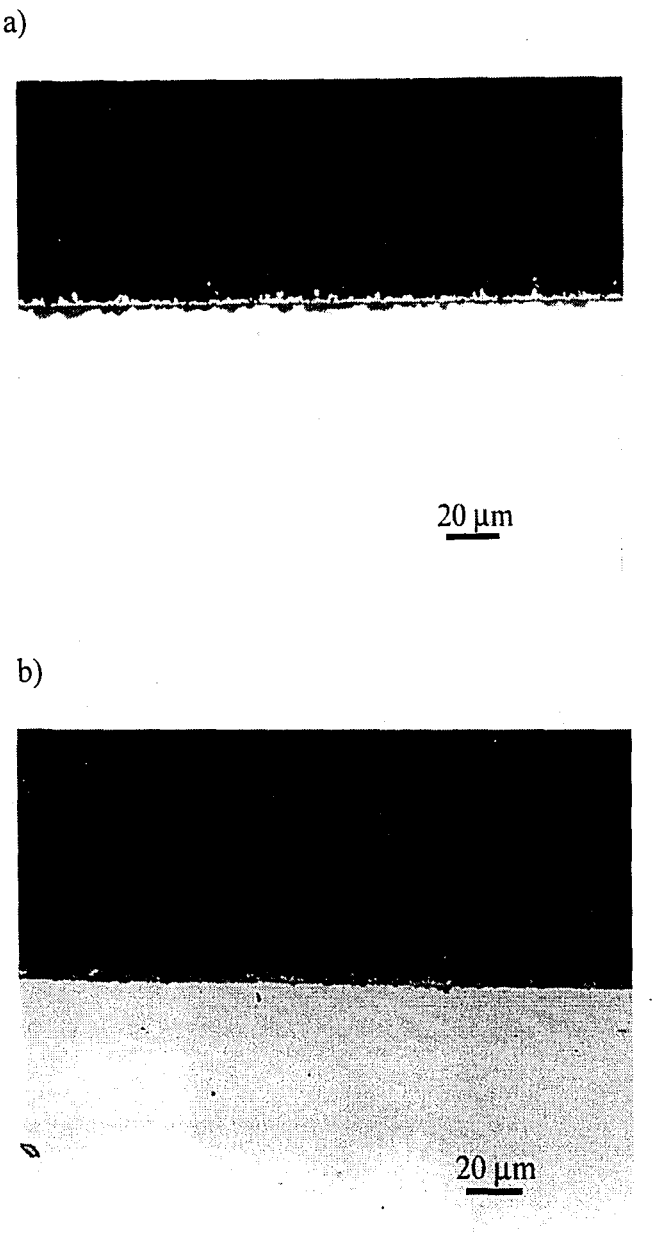

Figure 4. 52: Photomicrographs of the cross sections of a)IN625 and b)IN622 after 96 hours exposure to cyclic atmosphere at 500°C.

a)

20 µm

b)

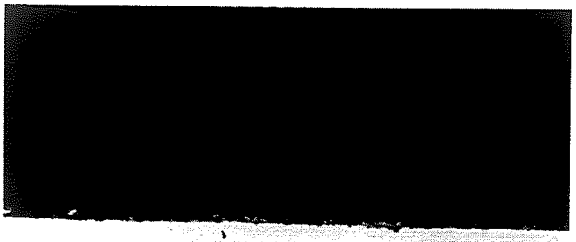

20 µm

Figure 4. 52: Photomicrographs of the cross sections of a)IN625 and b)IN622 after 96 hours exposure to cyclic atmosphere at 500°C.

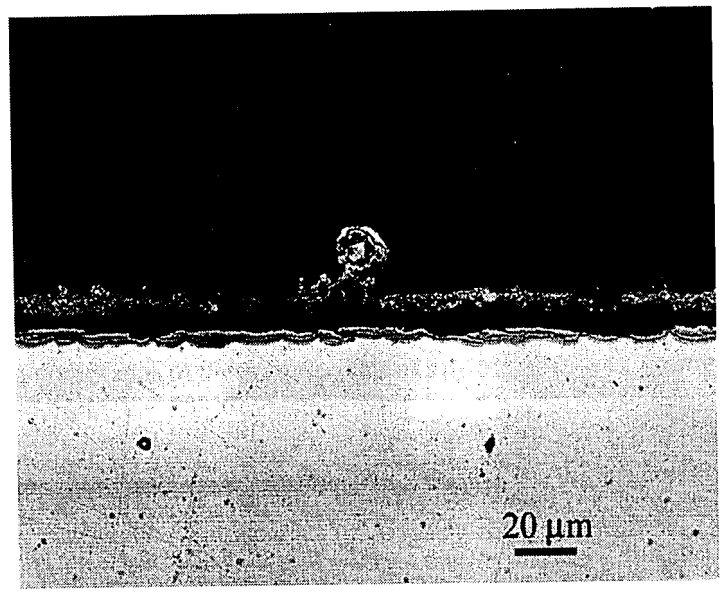

Figure 4. 53: Photomicrograph of the cross section of FM72 after 96 hours exposure to cyclic gas atmosphere at 500°C.

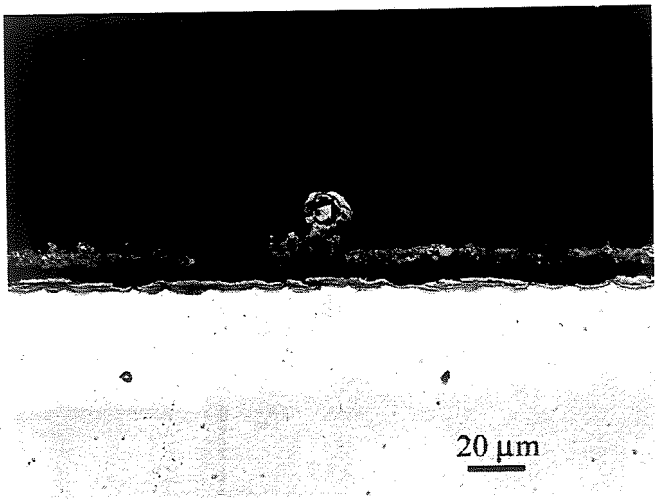

Figure 4. 53: Photomicrograph of the cross section of FM72 after 96 hours exposure to cyclic gas atmosphere at 500°C.

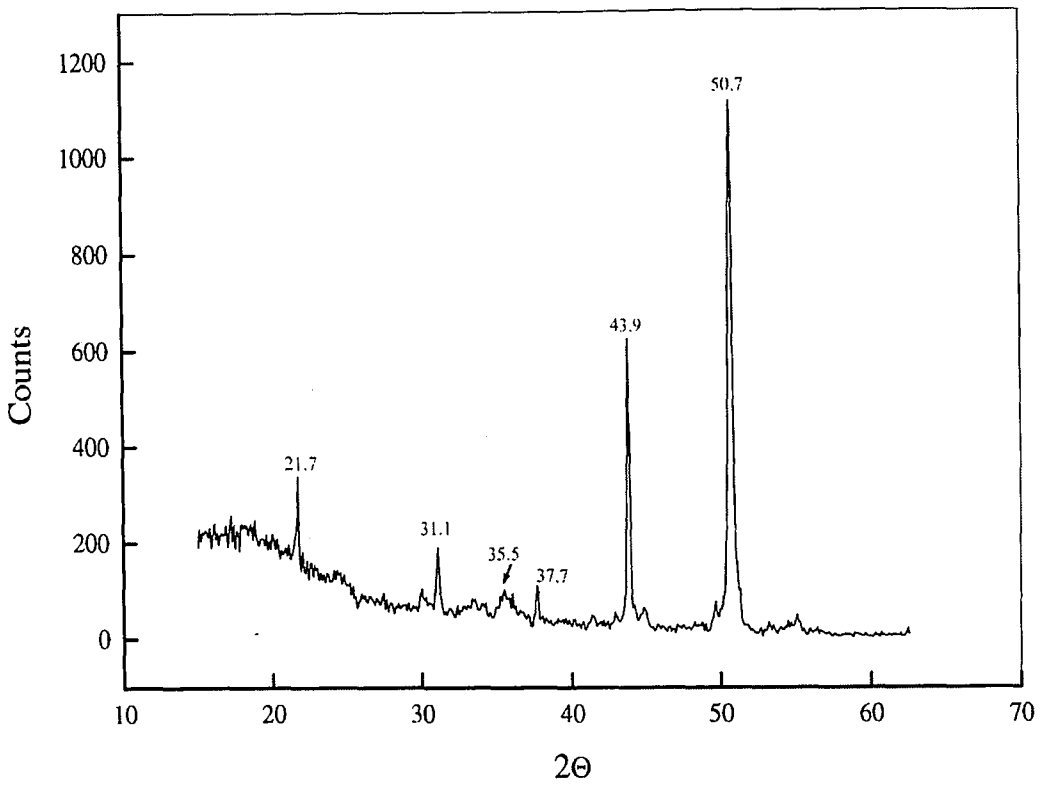

Figure 4. 54: X-ray spectrum obtained for FM72 exposed to cyclic atmosphere for 96 hours at 500°C performed with Cu Kα radiation.

Table 4. 9: List of possible phases formed in FM72 exposed to cyclic atmosphere. Data obtained from JCPDS – International Centre for Diffraction Data.

FM72 GasCycle	FeS	FeS2	Fe3O4	NiS	Ni3S2	NiS2	NiO	Cr2O3	CrS	Possible Compounds
21.7					21.76					Ni3S2
31.1			31.249		31.11	31.615				Ni3S2, NiS2
35.5	35.55			35.73		35.336				FeS, NiS, NiS2
37.7		37.074		37.38	37.78		37.25		37.733	FeS2, NiS, Ni3S2, NiO, CrS
43.9	43.18						43.28		43.035	
50.7				50.19	50.12			50.22		NiS, Ni3S2, Cr2O3

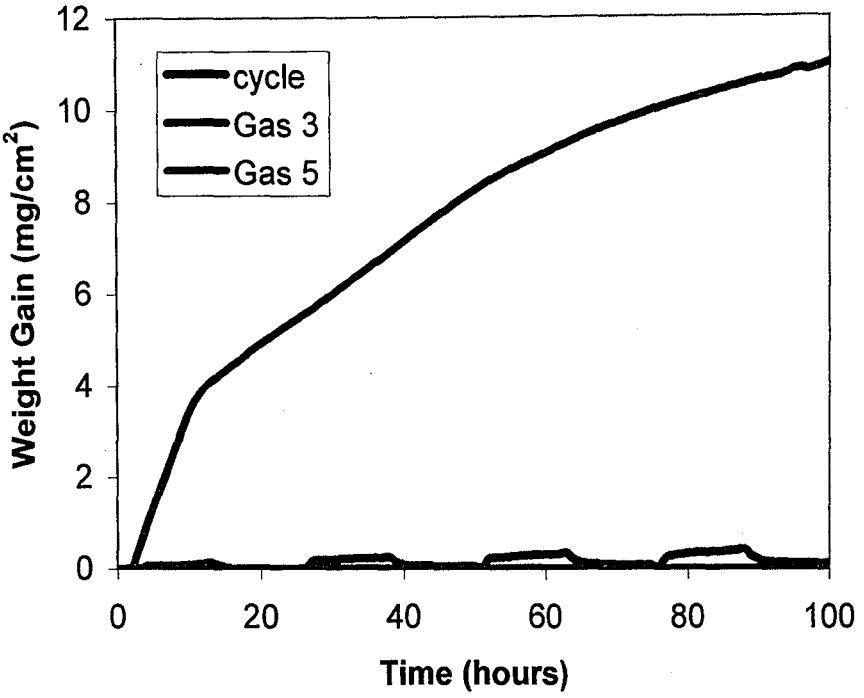

Figure 4. 55: Comparison of corrosion kinetics for IN622 in Gas 3, Gas 5 (catalyzed), and cyclic atmosphere.

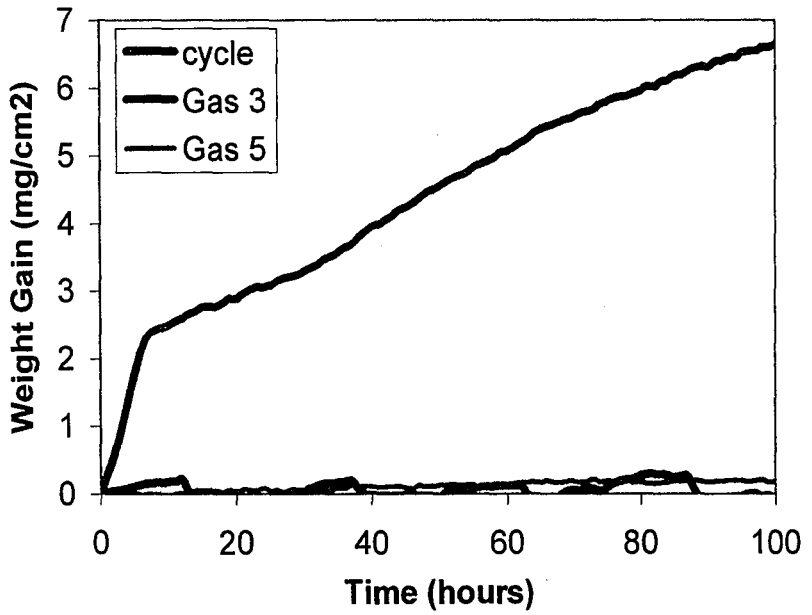

igure 4. 56: Comparison of corrosion kinetics for IN625 in Gas 3, Gas 5 (catalyzed), and cyclic atmosphere.

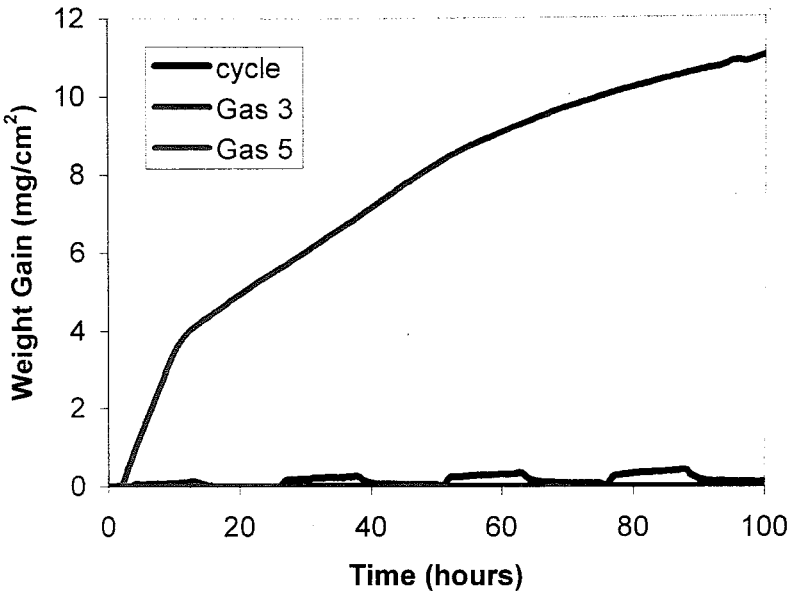

Figure 4. 55: Comparison of corrosion kinetics for IN622 in Gas 3, Gas 5 (catalyzed), and cyclic atmosphere.

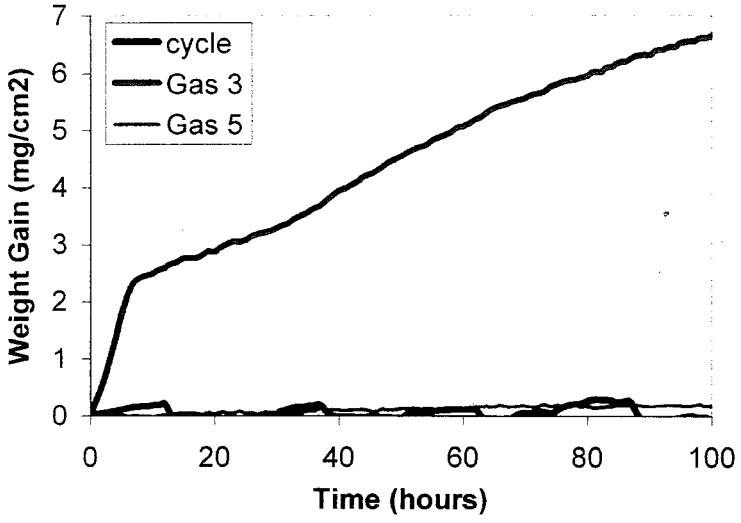

igure 4. 56: Comparison of corrosion kinetics for IN625 in Gas 3, Gas 5 (catalyzed), and cyclic atmosphere.

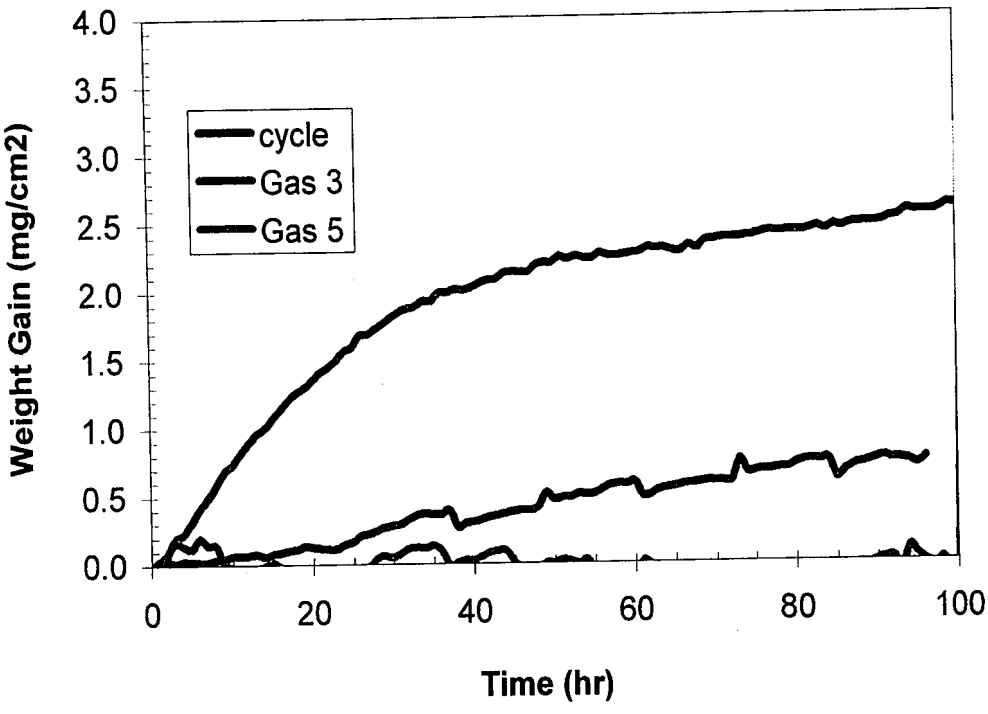

Figure 4. 57: Comparison of corrosion kinetics for FM72 in Gas 3, Gas 5 (catalyzed), and cyclic atmosphere.

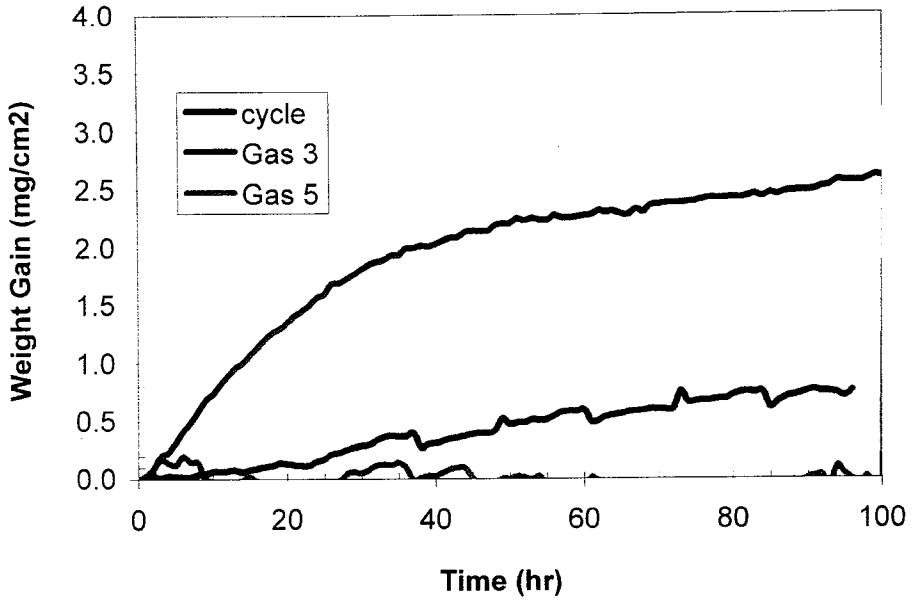

Figure 4. 57: Comparison of corrosion kinetics for FM72 in Gas 3, Gas 5 (catalyzed), and cyclic atmosphere.

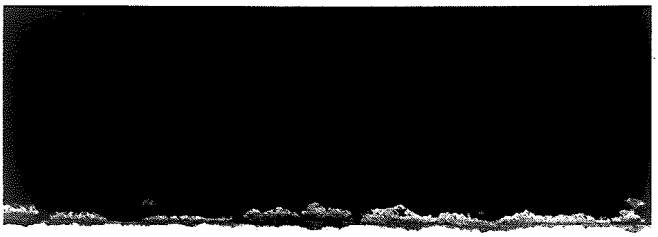

Figure 4. 58: Photomicrograph of the cross section of 309SS exposed to cyclic atmosphere for 96 cycles at 500°C.

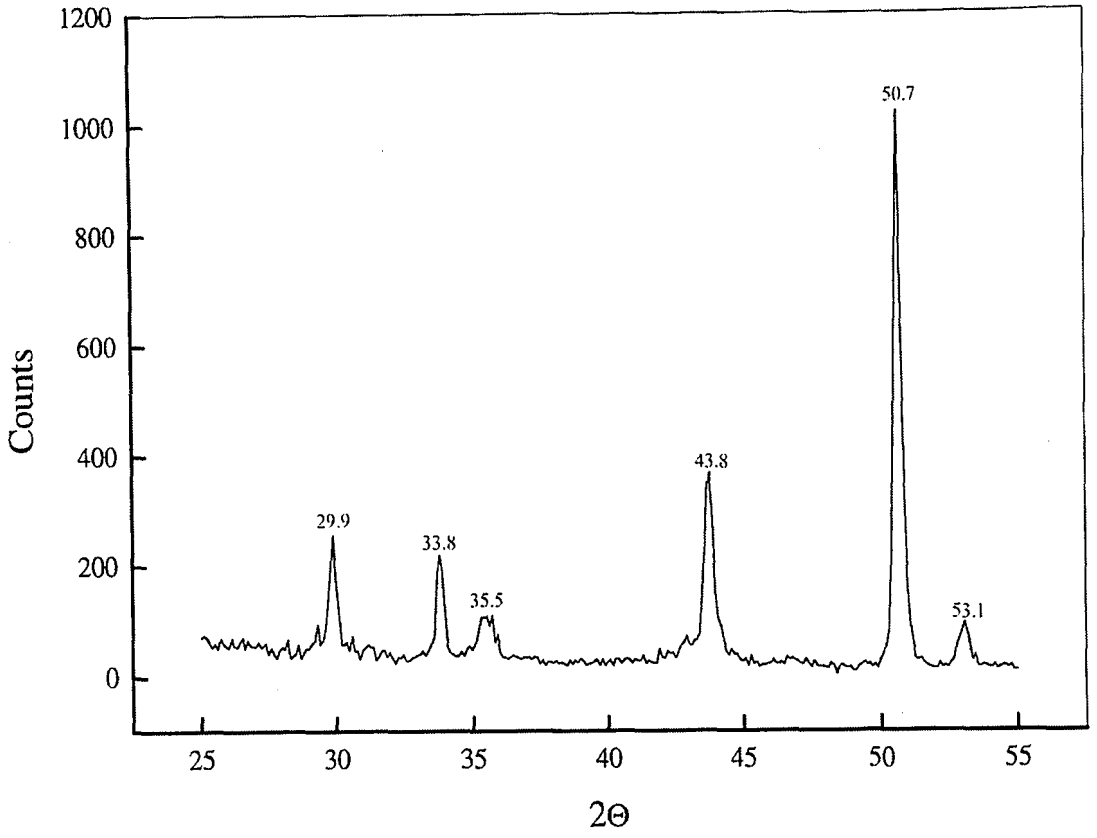

Figure 4. 59: XRD spectrum obtained for 309SS exposed to cyclic atmosphere for 96 hours at 500°C performed with Cu Kα radiation.

Table 4. 10: List of possible phases formed in 309SS exposed to cyclic atmosphere. Data obtained from JCPDS – International Centre for Diffraction Data.

309SS Gas cycle	FeS	Fe2O3	FeCr2S4	NiS	Ni3S2	NiS2	NiO	Cr2O3	CrS	Possible Compounds
29.9	29.943		29.7						29.563	FeS, CrS, FeCr2S4
33.8	33.693	33.45						33.6	33.756	FeS, FeS, Fe2O3, Cr2O3
35.5	35.553	35.88		35.73		35.34				FeS, Fe2O3, NiS, NiO, CrS
43.8	43.181						43.28		43.035	FeS, NiO
50.7				50.19	50.123			50.22		NiS, Ni3S2, Cr2O3

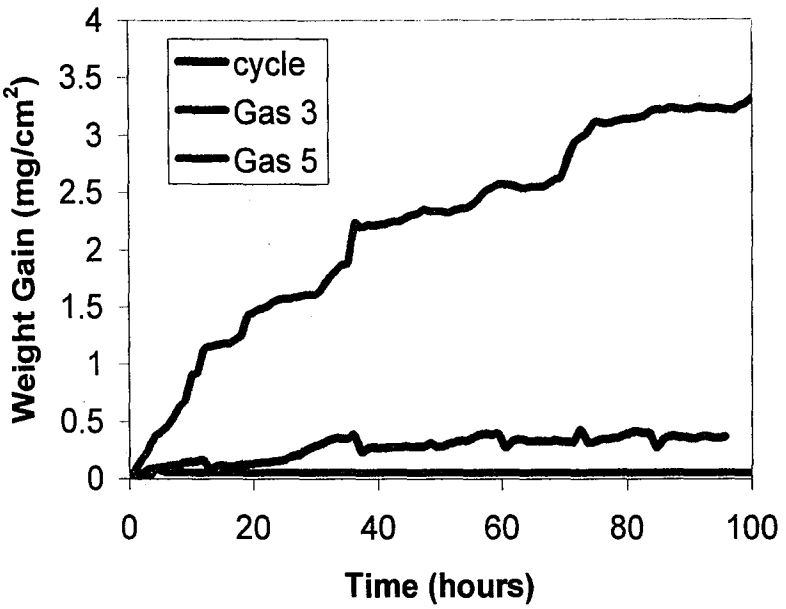

Figure 4. 60: Comparison of weight gain vs. time for the exposure of 309SS in Gas 3, Gas 5 (catalyzed), and cyclic atmosphere.

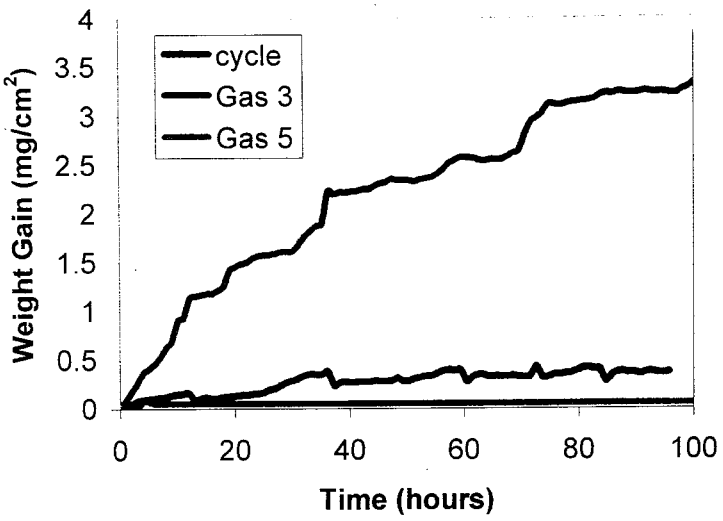

Figure 4. 60: Comparison of weight gain vs. time for the exposure of 309SS in Gas 3, Gas 5 (catalyzed), and cyclic atmosphere.

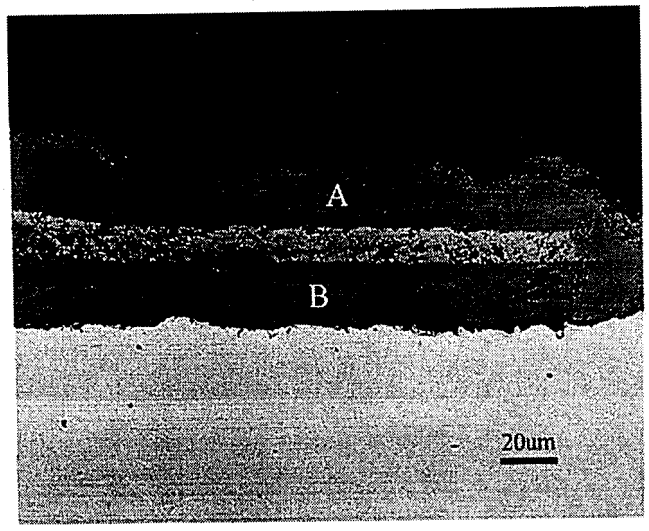

Figure 4. 61: Photomicrograph of the cross section of T11 exposed to cyclic atmosphere for 96 hours at 500°C.

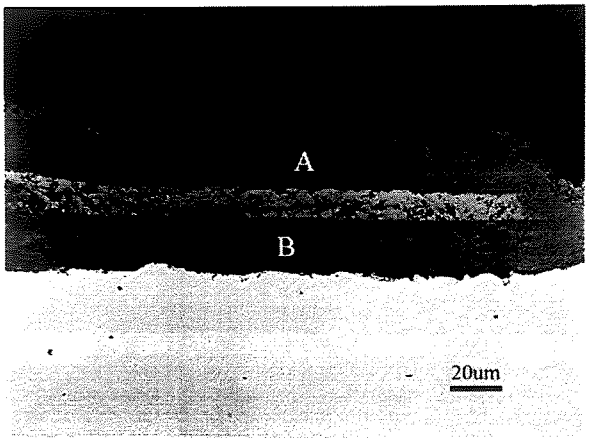

Figure 4. 61: Photomicrograph of the cross section of T11 exposed to cyclic atmosphere for 96 hours at 500°C.

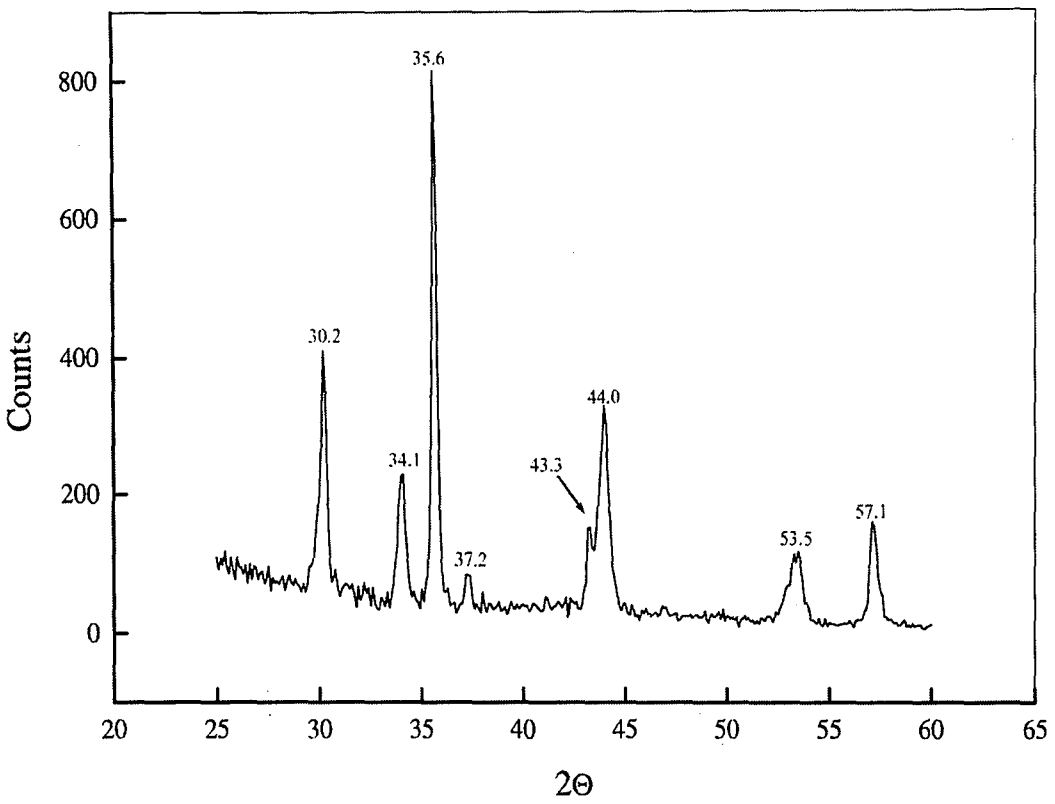

Figure 4. 62: X-ray spectrum obtained for T11 exposed to cyclic atmosphere performed using Cu Kα radiation.

Table 4. 11: List of possible phases formed on T11 exposed to cyclic atmosphere. Data obtained from JCPDS – International Centre for Diffraction Data.

T-11, Gas Cycle	FeS	FeS2	Fe2O3	Fe3O4	Fe2(SO4)3	FeSO4	Cr2O3	Possible Compounds
30.3	30.402							FeS
34.1						34.116		FeSO4
35.7	35.553		35.88					FeS, Fe2O3
37.2		37.074			37.807	37.892		Fe(SO4)3, FeS2, FeSO4
43.3	43.181							FeS
44				44.762		44.061	44.194	Fe3O4, FeSO4
53.5	53.169				53.478	53.548		FeS, FeSO4, Fe2(SO4)3
57.1								?

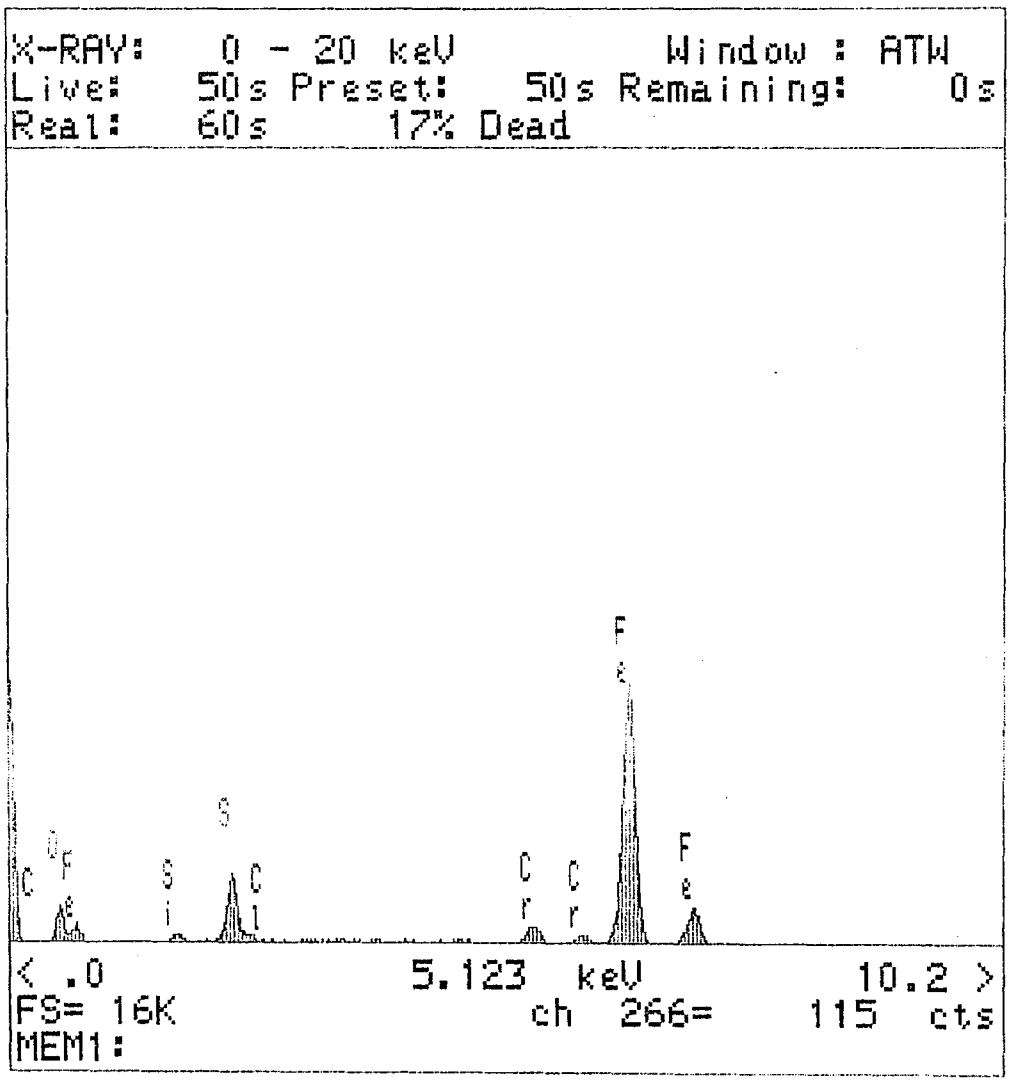

Figure 4. 63: EDS spectrum obtained for area A in Figure 4. 61. Shows presence of iron, chromium, oxygen, and sulfur.

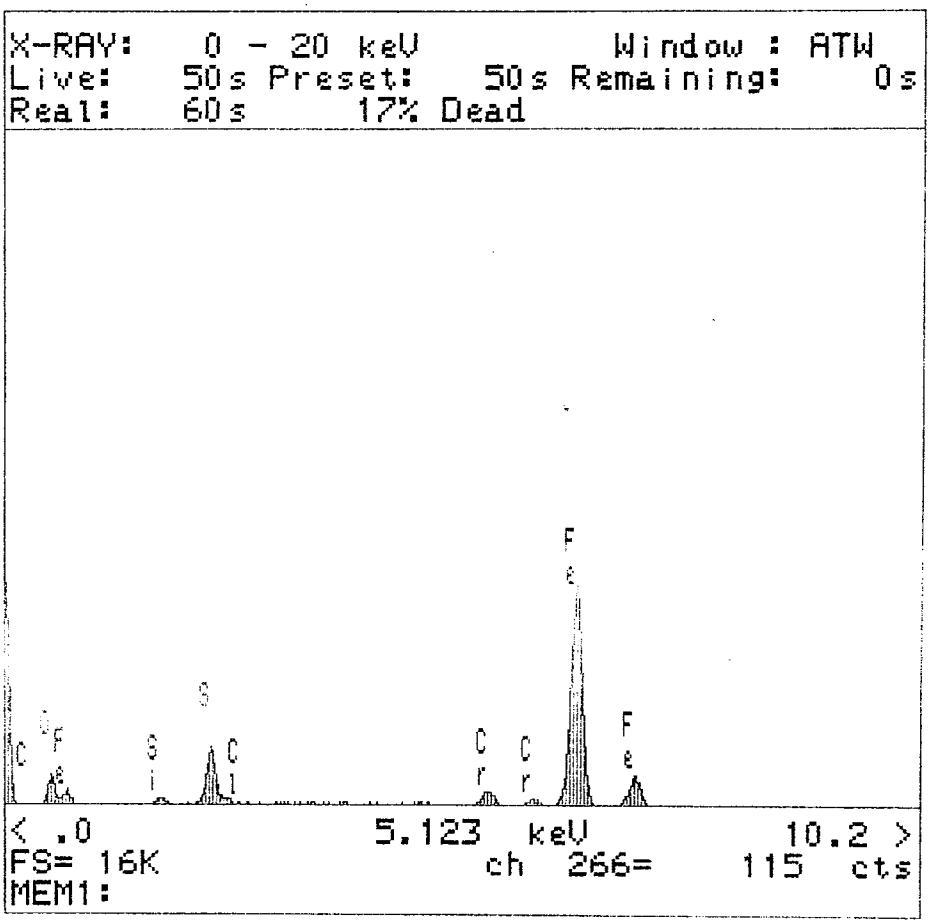

Figure 4. 63: EDS spectrum obtained for area A in Figure 4. 61. Shows presence of iron, chromium, oxygen, and sulfur.

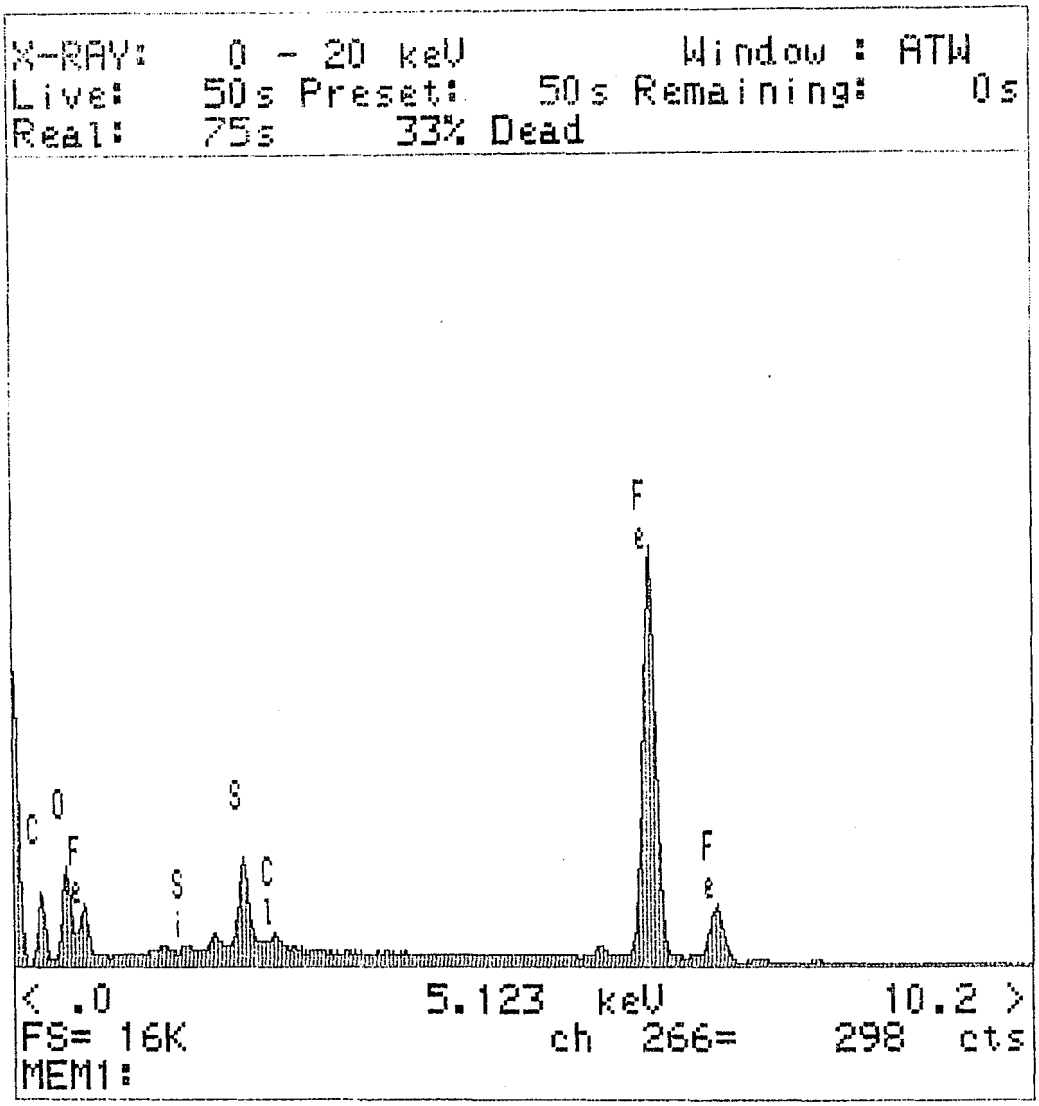

Figure 4. 64: EDS spectrum obtained for area B in Figure 4.70. Shows presence of iron, oxygen, and sulfur.

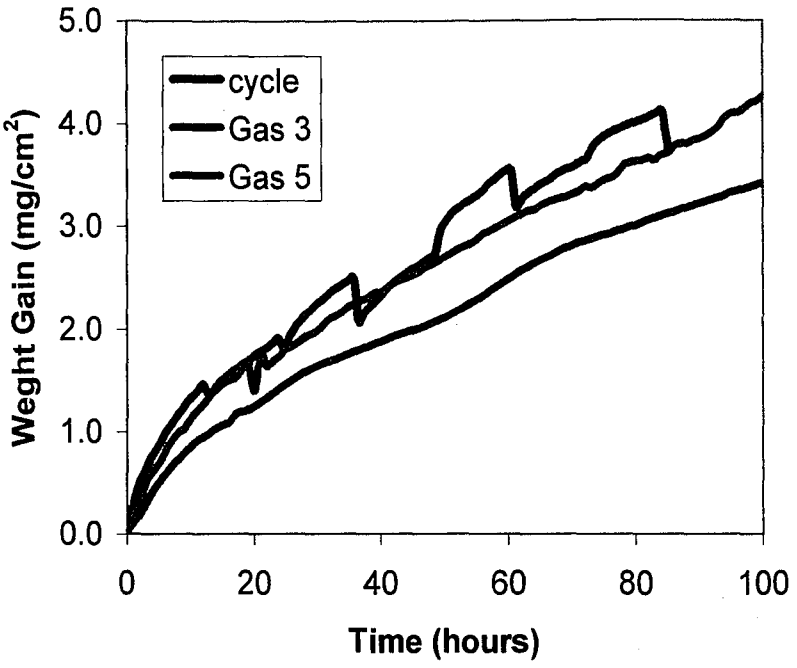

Figure 4. 65: Comparison of weight gain vs. time for T11 exposed to Gas 3, Gas 5 (catalyzed), and cyclic atmosphere.

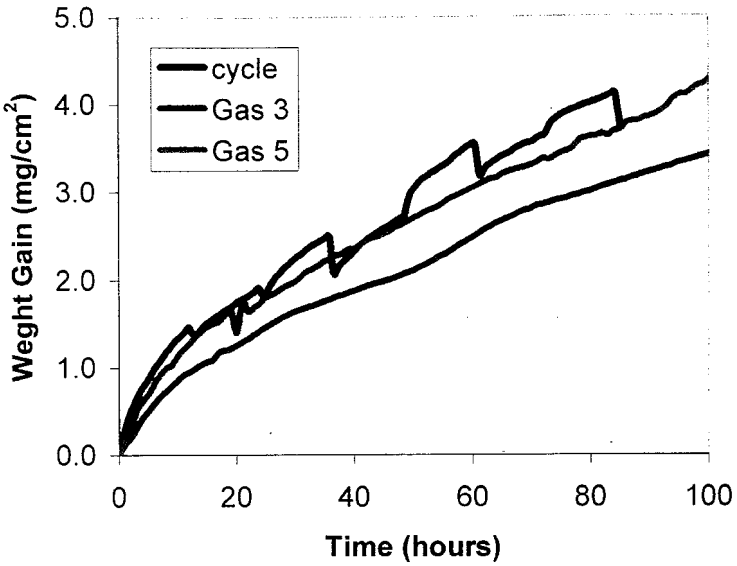

Figure 4. 65: Comparison of weight gain vs. time for T11 exposed to Gas 3, Gas 5 (catalyzed), and cyclic atmosphere.

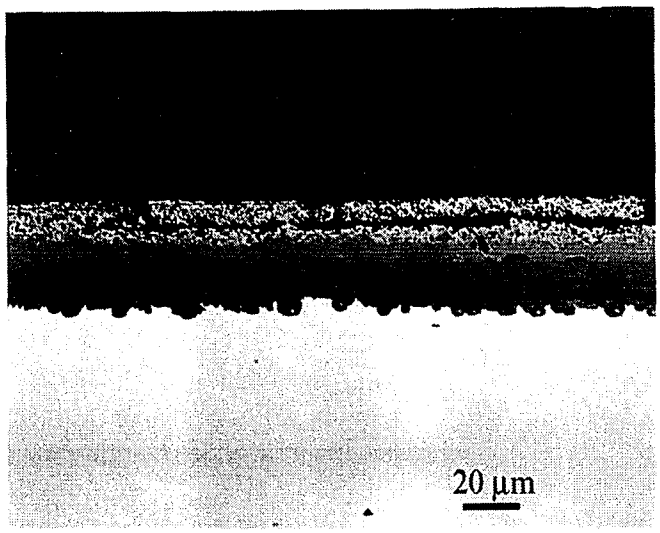

Figure 4. 66: Photomicrograph of the cross section of Fe-10wt%Al exposed to cyclic gas atmosphere for 96 hours at 500°C.

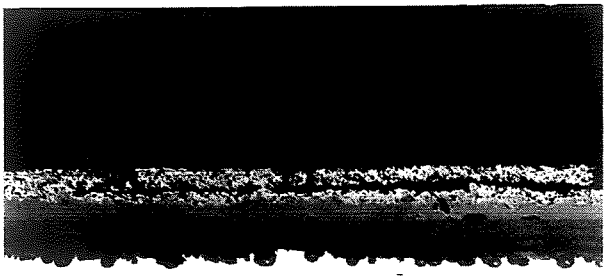

Figure 4. 66: Photomicrograph of the cross section of Fe-10wt%Al exposed to cyclic gas atmosphere for 96 hours at 500°C.

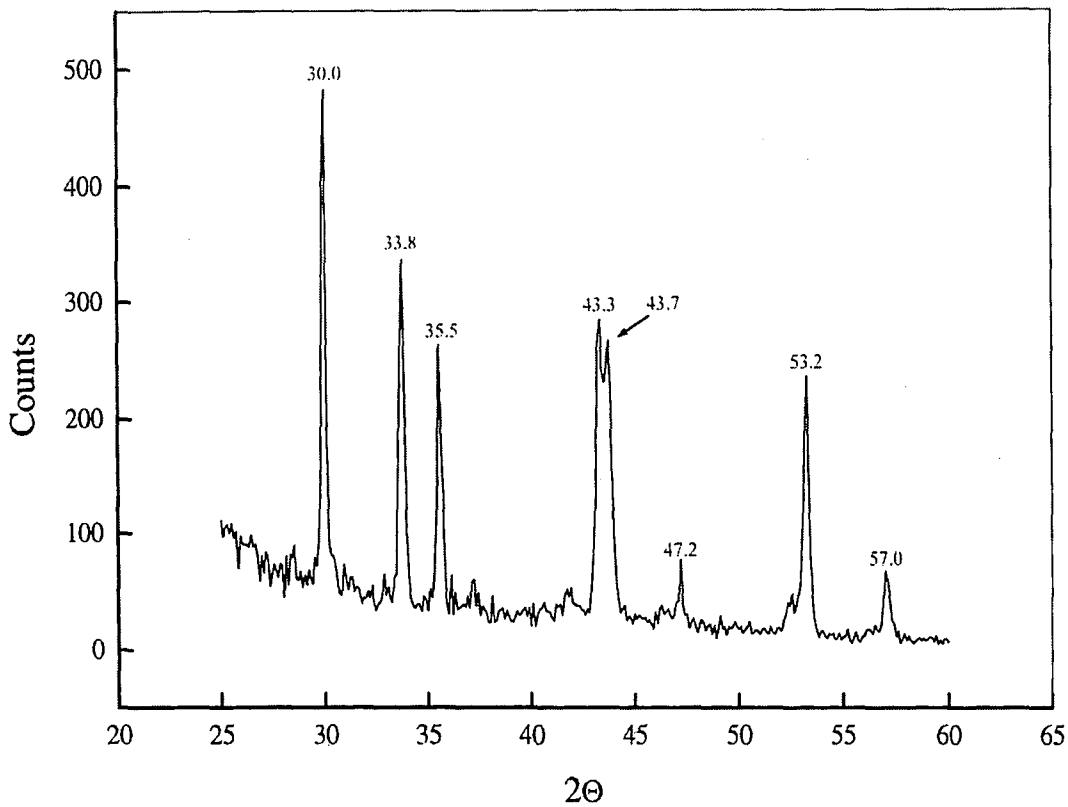

Figure 4. 67: X-ray spectrum obtained for Fe-10wt%Al exposed to cyclic gas atmosphere.

Table 4. 12: List of possible phases formed on Fe-10wt%Al. Data obtained from JCPDS – International Centre for Diffraction Data.

Fe10Al-gas cycle	FeS	FeS2	Fe2O3	Fe3O4	Fe2(SO4)3	FeSO4	Possible Compounds
30	30.402						FeS
33.8	33.693	33.04	33.447		33.458		FeS, FeS2, Fe2O3, Fe2(SO4)3
35.5	35.553		35.88				FeS, Fe2O3
43.3	43.181						FeS
43.7				44.762		44.061	Fe3O4, FeSO4
47.2	47.162	47.424				47.197	FeS, FeS2 Fe2(SO4)3
53.2	53.169				53.478	53.548	FeS, Fe2(SO4)3
57							?

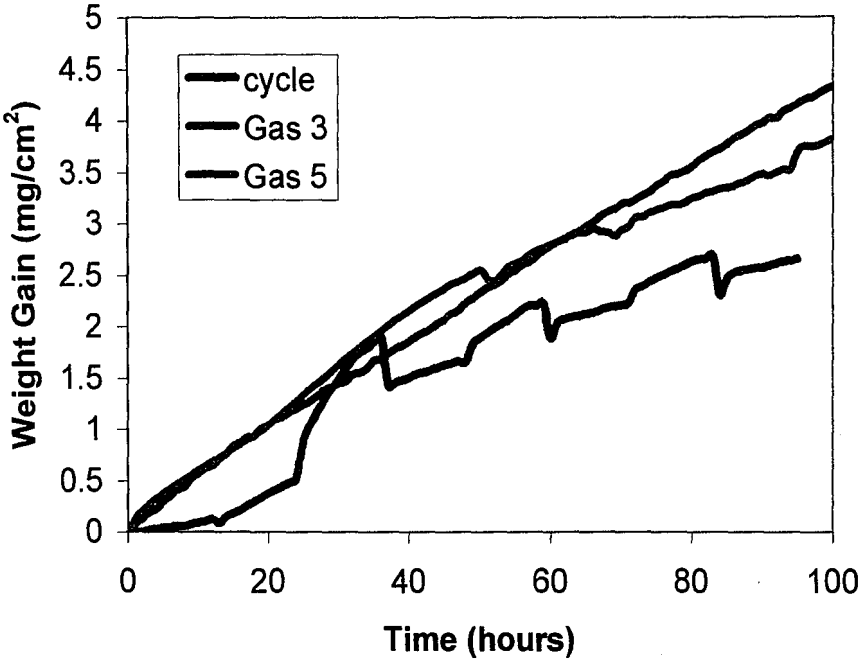

Figure 4. 68: Comparison of weight gain vs. time for exposure of Fe-10wt%Al exposed to Gas 3, Gas 5 (catalyzed), and cyclic atmosphere.

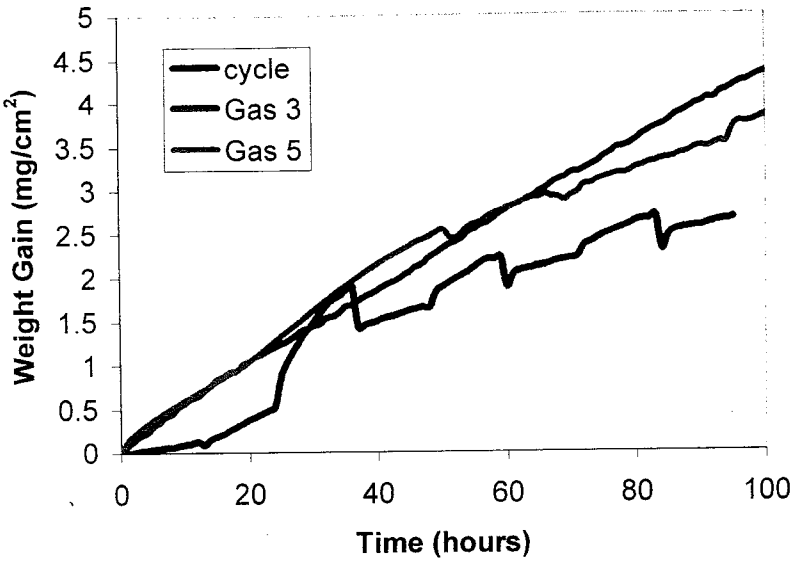

Figure 4. 68: Comparison of weight gain vs. time for exposure of Fe-10wt%Al exposed to Gas 3, Gas 5 (catalyzed), and cyclic atmosphere.

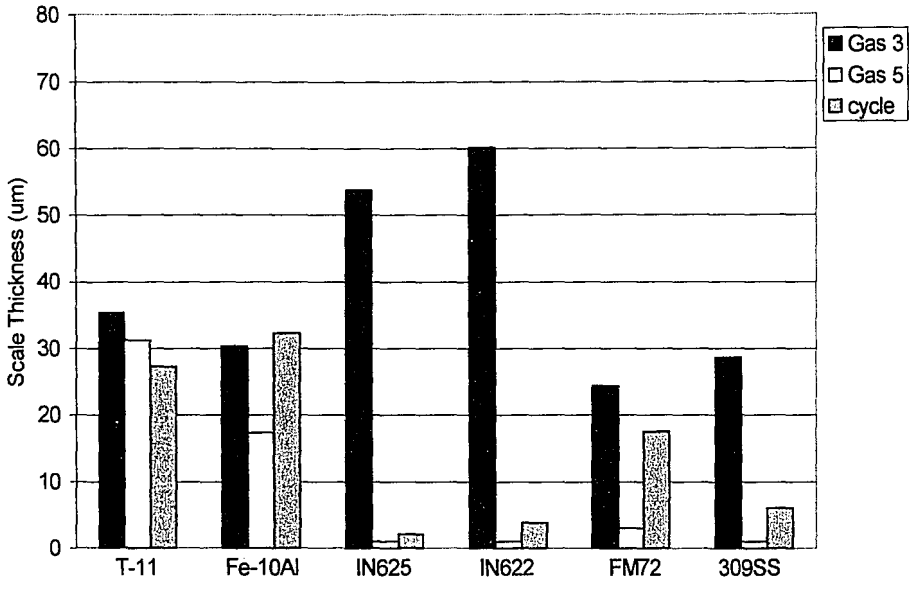

Figure 4. 69: Comparison of the scale thickness of each alloy in Gas 3, Gas 5 (catalyzed), and gas cycle atmospheres.

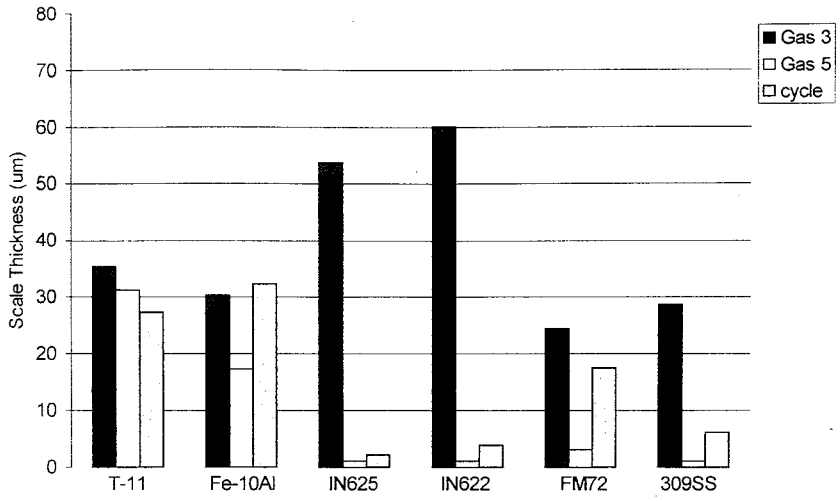

Figure 4. 69: Comparison of the scale thickness of each alloy in Gas 3, Gas 5 (catalyzed), and gas cycle atmospheres.

VITA

Melissa Ann Lim was born on March 9, 1976 in Princeton, New Jersey. Her parents, Chong and Helen Lim, currently reside in Doylestown, Pennsylvania. She has an older sister, Valerie, and a younger brother, Derek. She attended Central Bucks East High School and graduated in June, 1994. Afterwards, she enrolled in Lehigh University and received her Bachelor of Science degree in Materials Science and Engineering in May, 1998. She then decided to continue her education at Lehigh and pursue a Master of Science degree. After completing her graduate program, she is looking forward to some rest and relaxation.

END OF TITLE